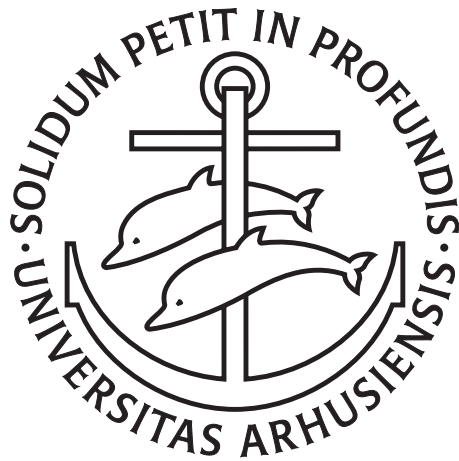

Nonlinear Wave Propagation in Photonic Crystal Fibers and Bose-Einstein Condensates



Karen Marie Hilligsøe

QUANTOP, Department of Physics and Astronomy &
NKT Academy, Department of Chemistry
University of Aarhus, Denmark

PhD thesis
February 2005

This thesis is submitted to the Faculty of Science at the University of Aarhus, Denmark, in order to fulfill the requirements for obtaining the PhD degree in Physics. The studies have been carried out at the Department of Physics and Astronomy under the supervision of Prof. Søren Keiding and Prof. Klaus Mølmer.



Contents

List of Publications	vii
Abstract	ix
1 Introduction to the thesis	1
1.1 Introduction	2
1.2 Thesis outline	2
2 Photonic crystal fibers	5
2.1 Introduction	6
2.2 Photonic crystal fibers	6
2.2.1 Dispersion properties of PCFs	7
2.2.2 Types of fibers	9
2.2.3 Applications	9
2.3 Solving Maxwells equations	10
2.3.1 Dispersion properties	11
2.3.2 Effective area	12
2.4 Conclusion	12
3 Model for wave propagation in photonic crystal fibers	15
3.1 Introduction	16
3.2 The nonlinear Schrödinger equation	16
3.3 Derivation of a nonlinear Schrödinger equation	17
3.4 Dispersion	21
3.4.1 Calculation of the propagation constant	21
3.4.2 Experimentally measured dispersion	21
3.5 Nonlinear effects	22
3.5.1 Raman response	22
3.5.2 Nonlinearity factor γ	22
3.5.3 Kerr nonlinearity	23
3.5.4 Overview of approached to the nonlinearity	23
3.6 Computational methods	24
3.6.1 Scaling	25
3.7 Conclusion	25

4 Supercontinuum generation	27
4.1 Introduction	28
4.2 Applications	29
4.3 Physical processes in supercontinuum generation	30
4.3.1 Self phase and cross phase modulation	31
4.3.2 Solitons	31
4.3.3 Higher order dispersion	31
4.3.4 Non-solitonic radiation	32
4.3.5 Raman scattering and self-steepening	34
4.3.6 Four wave mixing	35
4.3.7 Higher harmonics	36
4.4 Supercontinuum evolution as a function of time and wavelength	37
4.4.1 Computational methods	37
4.5 Comparison with experiments	40
4.5.1 Comparison of spectra	41
4.5.2 Phase-matched NSR	42
4.5.3 Threshold	42
4.5.4 Intensity of the nonsolitonic radiation	43
4.5.5 Wavelength of the nonsolitonic radiation	44
4.6 Conclusion	46
5 Four wave mixing in a photonic crystal fiber	47
5.1 Introduction	48
5.2 PCF with two zero dispersion wavelengths	48
5.3 Experiments	50
5.4 Pulse evolution in the fiber	51
5.4.1 Computational methods	56
5.5 Applications	57
5.6 Phase-matched FWM - continuous wave regime	57
5.7 Conclusion	57
6 BEC in optical lattices	59
6.1 Introduction	60
6.2 Fundamentals of BEC physics	61
6.2.1 The two-body interaction potential	62
6.2.2 Second quantized Hamiltonian	63
6.2.3 The Bogoliubov approximation and mean field theory	63
6.2.4 The Gross-Pitaevskii equation	64
6.2.5 Elementary excitations	65
6.2.6 One-dimensional nonlinear Schrödinger equation	66
6.3 Bose-Einstein condensates in optical lattices	67
6.3.1 The optical lattice	67
6.3.2 Linear description	68
6.3.3 Nonlinear description	69
6.3.4 General stability properties	70

6.3.5	Shallow lattices	71
6.3.6	Deep lattices	72
6.3.7	Superlattices	73
6.4	Conclusion	73
7	Quantum beam splitting	75
7.1	Introduction	76
7.2	Phase-matched four wave mixing	77
7.3	Mean-field analysis	77
7.4	Mean field results	79
7.4.1	Double four wave mixing	80
7.5	Varying k_0	80
7.6	Rabi-oscillations	82
7.7	Wave function in direct space	84
7.8	Number state analysis	85
7.8.1	Detuning	87
7.8.2	Conclusion on number state analysis	88
7.9	Conclusion	88
8	Conclusion and perspectives	93
8.1	Conclusion and perspectives	94
8.2	Acknowledgments	97
	Bibliography	99

List of Publications

- [I] *Stability of gap solitons in a Bose-Einstein condensate*,
K.M. Hilligsøe, M.K. Oberthaler and K.-P. Marzlin, Phys. Rev. A **66**, 063605 (2002).
- [II] *Coherent anti-Stokes Raman scattering microscopy with a photonic crystal fiber based light source*,
H.N. Paulsen, K.M. Hilligsøe, J. Thøgersen, S.R. Keiding and J.J. Larsen, Opt. Lett., **28**, 1123 (2003).
- [III] *Initial steps of supercontinuum generation in photonic crystal fibers*,
K.M. Hilligsøe, H.N. Paulsen, J. Thøgersen, S.R. Keiding and J.J. Larsen, J. Opt. Soc. Am. B., **20**, 1887 (2003).
- [IV] *Supercontinuum generation in a photonic crystal fiber with two zero dispersion wavelengths*,
K.M. Hilligsøe, T.V. Andersen, H.N. Paulsen, C.K. Nielsen, K. Mølmer, S.R. Keiding, R. Kristiansen, K.P. Hansen and J.J. Larsen, Opt. Express, **12**, 1045 (2004),
<http://www.opticsexpress.org/abstract.cfm?URI=OPEX-12-6-1045>.
- [V] *Continuous-wave wavelength conversion in a photonic crystal fiber with two zero-dispersion wavelengths*,
T.V. Andersen, K.M. Hilligsøe, C.K. Nielsen, J. Thøgersen, K.P. Hansen, S.R. Keiding and J.J. Larsen, Opt. Express, **12**, 4113 (2004),
<http://www.opticsexpress.org/abstract.cfm?URI=OPEX-12-17-4113>.
- [VI] *Phase-matched four wave mixing and quantum beam splitting of matter waves in a periodic potential*,
K.M. Hilligsøe and K. Mølmer,
arXiv:cond-mat/0411228, accepted for publication in Phys. Rev. A, Rapid Communications.

Abstract

Dansk resumé.

Denne afhandling beskæftiger sig med udbredelse af lys i fotoniske krystal-fibre. Lufthuller i længderetningen af denne nye type lyslederkabel er årsag til fibrenes specielle egenskaber. Afhandlingen beskæftiger sig med, hvordan ekstremt brede frekvensspektre dannes i fibrene. Andre har anvendt spek-trene til at udvikle en ny optisk frekvensstandard. Fire-bølge-blanding, hvor to lyskvanter forenes i fiberen og danner to nye, behandles. Processen kan po-tentielt anvendes til frekvenskonvertering i optiske netværk. Det andet emne i afhandlingen er Bose-Einstein kondensater i optiske gitre. Det undersøges, hvorledes to atomers impulser omdannes til to nye impulser gennem en fire-bølge-blandingsproces ækvivalent med fire-bølge-blandingen i fibrene.

Nonlinear wave propagation in photonic crystal fibers is a main theme in this thesis. The fibers possess unique dispersive properties due to the transverse micro-structuring. The generation of supercontinua in the fibers caused by the interplay between the dispersion and a cascade of nonlinear effects is investigated in the thesis. Already, the spectra have been used by others to develop optical frequency standards. For photonic crystal fibers with two closely lying zero dispersion wavelengths phase-matched four wave mixing plays a dominating role as shown in the thesis. The process can potentially be used for frequency conversion in optical networks. The spectra generated in these fibers with femtosecond pulses can in principle be compressed to sub 15 femtoseconds. The other system treated in the thesis is Bose-Einstein condensates in optical lattices. In this system the dispersive properties can be controlled by the optical lattice making it possible to achieve phase-matched four wave mixing, resembling the process taking place in the photonic crystal fibers.

CHAPTER 1

Introduction to the thesis

Wave propagation is a fundamental phenomenon occurring in several physical systems. This thesis will focus on two such systems: The propagation of light in photonic crystal fibers and the propagation of matter waves in optical lattices. In this very brief chapter an outline of the thesis will be given.

1.1 Introduction

Photonic crystals are periodic structures of dielectric materials and can today be produced with almost any imaginable structure. In this thesis focus will be on propagation of light in photonic crystal fibers (PCFs). These fibers are based on a new and very promising technology and could provide solutions to many optical problems in telecommunications, light source manufacturing and has already revolutionized the field of frequency metrology.

The light itself can also provide periodic structuring through an optical lattice and in this system matter wave propagation will be investigated. It is only a decade ago that Bose-Einstein condensation was first achieved in alkali gases [1, 2] and it has certainly turned into a very rich field since the condensates are very flexible model systems for solid state physics and statistical physics in general.

The dynamics of the wave propagation in both systems is mainly determined by the interplay between dispersive and nonlinear effects. Consequently, even though the systems are fundamentally different, the physical phenomena are still much the same. In Fig. 1.1 the two systems have been listed side by side. In the Bose-Einstein condensates (BECs) the nonlinear response originates in the s-wave scattering between atom pairs, whereas the nonlinearity in the PCFs stems from saturation and optical pumping accounted for through a nonlinear susceptibility. The micro-structuring of the PCFs leads to unique and tailorable dispersive properties. In the Bose-Einstein condensed system the optical lattice does the job of tuning the dispersion.

In many situations the systems can be described by a type of nonlinear Schrödinger equation. In addition the behavior of the two systems is highly influenced by phase-matched processes such as four wave mixing, to which a great deal of attention will be paid in this thesis.

1.2 Thesis outline

The outset for the work concerning the PCFs was the understanding of super-continuum generation in the fibers. Chapter 2 gives a short introduction to the basic concepts of PCFs. In Chap. 3 a derivation of a general version of the nonlinear Schrödinger equation is outlined. The chapters 4 and 5 are devoted to answering the following question: **How does light propagate in a specific type of PCF?** In particular, Chap. 4 focuses on describing the evolution of light in a typical PCF with only one zero dispersion wavelength, where emission of phase-matched non-solitonic radiation is a central process. This chapter is mainly based on the paper [III]. Chapter 5 concerns the light propagation in a fiber with two closely lying zero dispersion wavelength and is based on the paper [IV] with relations to paper [V]. In this fiber the determining process is instead phase-matched four wave mixing. Simulations are compared to experimental data obtained by the Femtosecond Group at the Department of Chemistry and

the PCFs used in the experiments have been provided by the company Crystal Fibre A/S.

The second part of the thesis concerns BECs in optical lattices and an introduction together with a brief review over the field is given in Chap. 6. The following central question in this part of the thesis was inspired by the role of phase-matched four wave mixing in PCFs. **Can phase-matched four wave mixing play a central role in a BEC in an optical lattice?** The answer is yes and Chap. 7 is devoted to the topic. This chapter is based on paper [VI], whereas the paper [I] is not explicitly treated in this thesis, since it relates to my Master's thesis work. Finally Chap. 8 closes the thesis with a conclusion and perspectives for further research.

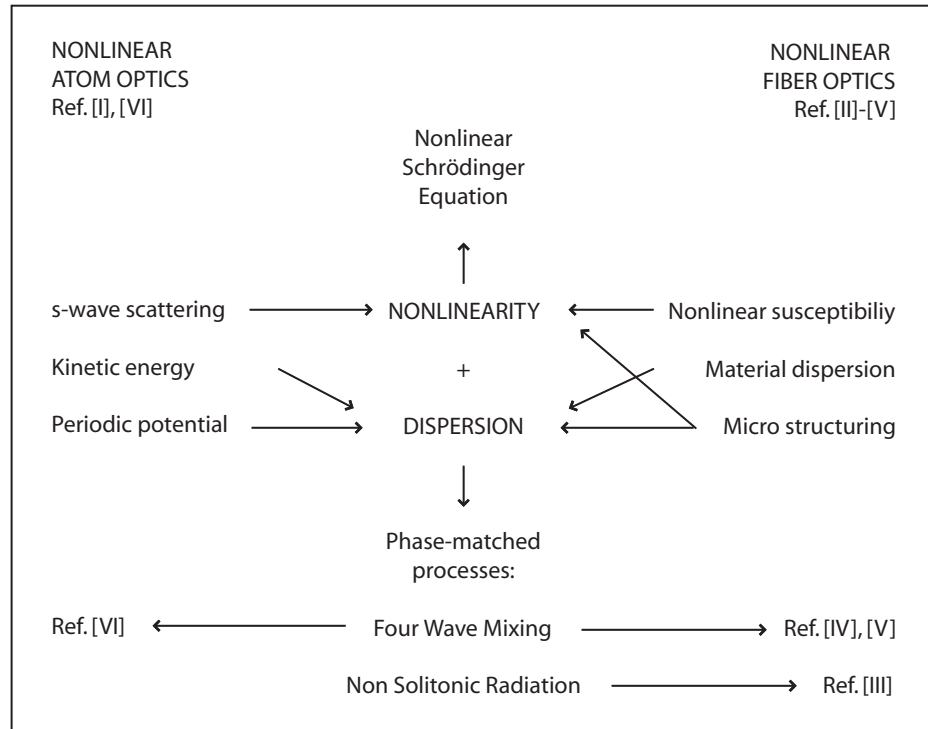


Figure 1.1: The dynamics of light propagation in PCFs and evolution of matter waves in optical lattices are basically determined by the interplay between dispersive and nonlinear effects. A nonlinear Schrödinger equation is often sufficient to describe the wave propagation in both systems. Phase-matched processes play important roles in the systems and the papers [IV-V] are treating four wave mixing in PCFs, whereas the paper [VI] concerns four wave mixing in a BEC in an optical lattice. The paper [III] is examining the production of phase-matched non-solitonic radiation in PCFs.

CHAPTER 2

Photonic crystal fibers

An introduction to PCFs is given. More thorough introductions to the field are given in the review articles [3, 4] and the book [5]. In this chapter it is furthermore sketched how the frequency dependent propagation constant and the effective area of the fibers can be found.

2.1 Introduction

Conventional optical fibers have within the last decades revolutionized the telecommunications industry and it is today a mature technology being pushed to its limit with respect to properties such as losses, single mode operation and dispersion. A new era started, not only in fiber optics, but in optics in general with the appearance of photonic crystals. The essential benefit offered by photonic crystals is the high degree of control of the light propagation. Investigations of the physical phenomena occurring in photonic crystals are interesting both from a basic scientific point of view and because of the possibilities for commercial applications for instance in an all optical network or for new light sources.

Like a crystal lattice results from the periodic arrangement of atoms or molecules, a photonic crystal arises from a periodic modulation of the refractive index of the material [6–8]. Due to the periodic structure of the atoms, crystals can exhibit band gaps and the propagation of electrons with energies within the band gap is consequently prohibited. Equivalently the periodic modulation of the refractive index in a photonic crystal leads to the possibility of photonic band gaps i.e. certain frequency intervals where light propagation in the crystal is prohibited. Hence a photonic band gap material or photonic crystal is the optical analog of electronic band gap materials.

Bragg stacks are 1D periodic structures that reflect maximally when the optical thickness of a layer is a quarter of a wavelength. These structures have been known for many years and are used for dielectric mirrors.

For a material to exhibit a full 3D photonic band gap, electromagnetic wave propagation for frequencies within the band gap must be forbidden irrespective of propagation direction. The photonic band gap effect was described by Yablonovitch [9] and John [10] in 1987. Materials exhibiting a full photonic band gap in 3D due to the periodic modulation of the refractive index were already demonstrated in 1991 [11, 12], but the manufacturing is still very challenging.

Important 2D photonic crystals are planar waveguides (where the light propagation is confined in the periodic plane by defects) and PCFs, which are the topic of the remainder of this chapter.

2.2 Photonic crystal fibers

PCFs are made of a periodic arrangement of fused silica and airholes running parallel to the axis of the fiber, with the scale of the microstructuring being comparable to the wavelength of the electromagnetic radiation guided by the fibers. An essential effect of the transverse periodic structure is to alter the effective refractive index for propagation along the direction of the fiber leading to intriguing new dispersive properties.

The fibers can be airguiding if the light is confined to an air defect at the center of the fiber. Fig. 2.1 (a) displays a scanning electron micrograph (SEM) image of such a fiber end face. Around the central air hole the periodic arrangement

of air and silica is seen to form a 2D photonic crystal structure. (One can say that the 2D photonic crystal forms the cladding of the fiber and the air hole in the middle is the core of the fiber, where the light is guided). In this fiber light is guided by the photonic band gap (PBG) effect. Frequencies within a band gap of the structure will experience multiple Bragg reflection leading to destructive interference of light trying to propagate away from the air core. The function of the air core is to provide a defect in the periodic structure in which the propagation of frequencies inside the band gap is actually allowed. Consequently, one speaks of a mode inside the band gap and this type of fiber is called a photonic band gap fiber. They were first demonstrated by P. St. J. Russell's group in Bath [13, 14].

Another possibility is to let the central defect be made of silica instead of air as seen on Fig. 2.1 (b). This type of fiber was also first demonstrated by the group in Bath [15]. The 2D photonic crystal around the core has an effective refractive index between that of silica and air. Therefore, the light guidance can be explained by total internal reflection (TIR), which is also the way light is guided in step index fibers. These fibers with a central material defect are hence referred to as index guiding fibers. Wave propagation in these fibers is a major topic in this thesis.

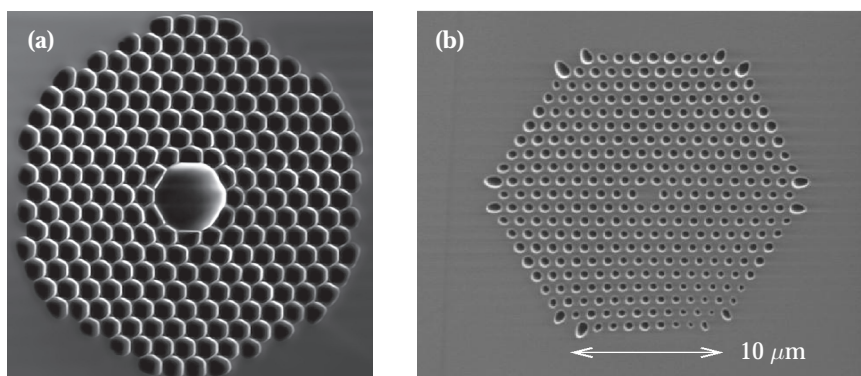


Figure 2.1: (a) SEM-image of a fiber in which light is guided by the photonic band gap effect. The light is guided in the big airhole (center of picture), which is surrounded by hollow silica tubes. The diameter of the central airhole is $9.3 \mu\text{m}$. (b) SEM-image of a PCF where the light is guided in the central core defect by total internal reflection. The dark parts of the picture indicate the airfilled regions, the brighter parts the fused silica. Pictures provided by Crystal Fibre A/S.

2.2.1 Dispersion properties of PCFs

In a homogeneous medium the dispersion relation between wave vector k and frequency ω of the propagating light is given through the refractive index of the material $\omega = c|k|/n$. In a PCF it is the combined effect of the material dispersion

and the band structure arising from the 2D photonic crystal that determines the dispersion characteristics of the fiber. For propagation in fibers it is the dispersion for the wave vector component along the z-direction k_z that is the interesting parameter. In the fiber optics literature k_z is referred to as the propagation constant β . It is then reasonable to define an effective refractive index as

$$n_{\text{eff}} = \frac{\beta c}{\omega_{\text{fund.}}}, \quad (2.1)$$

where $\omega_{\text{fund.}}$ denotes the frequencies of the lowest lying mode in the fiber.

The higher derivatives of the propagation constant are given as

$$\beta_n(\omega) = \frac{\partial^n \beta}{\partial \omega^n}, \quad (2.2)$$

and the second order dispersion $D = -\frac{2\pi c}{\lambda^2} \beta_2$ is just another way of expressing β_2 . The zero-dispersion wavelength (λ_{ZD}) is defined as the free space wavelength $\lambda = 2\pi c/\omega$ where $\beta_2 = 0$.

A cross-section of an index guiding PCF is shown in Fig. 2.2 and in Sec. 2.3 a calculation of the dispersion properties and effective area of this fiber will be sketched. The dispersion given by $\beta_2(\lambda)$ is shown in Fig. 2.3 (a) and the fiber has $\lambda_{ZD} = 721$ nm, whereas the zero dispersion wavelength for bulk silica is found around 1300 nm. The zero dispersion wavelength for this fiber has consequently been shifted into the visible regime due to the micro-structuring. This widely tunable group velocity dispersion is an extremely valuable property of the PCFs. The dispersion can be tuned by a proper choice of the size of the airholes, the distance between the holes (pitch) and the size of the central defect. A general tendency is that the zero dispersion wavelength is found at a shorter wavelength when the fraction of airfilling is increased and the central defect is decreased [5]. It is possible to manufacture fibers with zero dispersion wavelengths between 500 and 1500 nm. Another general trend is that decreasing either the pitch or the hole-size leads to a higher curvature of the dispersion profile, eventually leading to two closely lying zero dispersion wavelengths. The effects of this fiber dispersion will be treated in detail in Chap. 5.

The fibers can be made with cores down to 1 μm in diameter. Due to the small core areas huge intensities can be obtained in the cores of the fibers. Consequently, such fibers will exhibit a highly nonlinear response.

Another very useful property of the fibers is that they can be made endlessly single mode. Only one mode should have a propagation constant between the effective propagation constants for the cladding and the core i.e. $n_{\text{core}}k > \beta > n_{\text{clad}}k$, where k is the free space propagation constant. The restriction corresponds to only one solution to Maxwell's equations propagating in the core and evanescent in the cladding. The effective frequency parameter is given by [13]

$$V_{\text{eff}} = (2\pi\rho/\lambda)\sqrt{n_{\text{core}}^2 - n_{\text{clad}}^2}, \quad (2.3)$$

where ρ is the core radius. For the fiber to be single mode V_{eff} should be below 2.405. As λ decreases, the effective index of the cladding n_{clad} increases, because

more intensity of the light will be confined to the silica part of the cladding. Consequently, V_{eff} can be kept below 2.405 for a wide range of wavelengths and the fiber is said to be endlessly singlemode. In this way fibers, even with a very large core, can be made endlessly singlemode [16].

As the mode area of the fiber increases the relative intensity in the core will decrease. Hence the fibers can be used for linear propagation, where a lot of power can be delivered without going into a nonlinear propagation regime.

2.2.2 Types of fibers

Microstructured fibers have also been produced from polymers [17] and soft glass [18]. The low index material need not be air, although air of course has the advantage of providing a very low refractive index and consequently the possibility for a high index contrast.

The PCFs have been doped with optically active rare earth elements such as Er, Yb, Th and Nd, making the fibers very attractive candidates for laser action. Furthermore, fibers with double claddings have been manufactured and lasers have been demonstrated with pumping into the inner cladding and lasing in the core [19–23].

There are innumerable possibilities for geometries of the fibers. Furthermore the systems are scalable, since the propagation in the structures are determined by Maxwell's equations. Of course the material dispersion of silica due to the resonances in the material is given beforehand.

The fibers can furthermore be produced with double cores, with possibilities for interactions and coherence of the light between the cores. By breaking the symmetry of the fiber, for instance by an elliptical core the fibers can be made polarization maintaining [24].

2.2.3 Applications

In telecommunication the fibers could provide many new solutions. The PBG fibers offer the possibility of low losses and dispersion, a possible competitor to conventional fibers [25].

The development of all optical networks could benefit from the index guiding PCFs, for instance with respect to optical switching [26] and wavelength conversion based on four wave mixing [27, 28], which is treated in Chap. 5.

The PBG fibers can act as flexible systems for atom optics. They can be filled with gases, and for instance Raman scattering of hydrogen has been investigated [29]. They can also act as wave-guides for matter waves if a dipole field is superimposed. The interactions with gases or liquids in the air holes of both the index guiding fibers and the fibers guiding by the PBG effect show interesting potentials for sensing purposes [30, 31]. Correlated pairs of photons, with potential applications in quantum optics, can be created in the fibers, for instance due to the phase-matched degenerate four wave mixing that will be discussed in

Chap. 5. The fibers have also been used in quantum optics to produce squeezed light through spectral filtering [32].

The generation of supercontinua was one of the first applications of the index guiding PCFs. Optical spectra spanning more than an octave of frequencies can be generated in the fibers and the spectra have already found a number of applications. The field of frequency metrology has been truly revolutionized by the generation of supercontinua [33, 34] and frequency standards based on the fibers are already commercially available. The continua have been used in optical imaging techniques such as nonlinear coherent anti-Stokes scattering microscopy [II] and optical coherence tomography [35]. Another application is as wavelength division multiplexing light sources, but the noise in the spectra is a challenge in this respect [36]. Since the initial demonstration of the supercontinua by Ranka et al. [37] a huge research effort has been put into identifying the processes and controlling the properties responsible for the generation of the supercontinua and it has definitely been a hot topic in optics.

Supercontinuum generation will be the topic of the following three chapters. Chapter 3 is devoted to a model for light propagation in the fibers in order to subsequently investigate the supercontinuum generation. The dispersion characteristics and the effective transverse area of the fibers, serve as input parameters in the model for wave propagation. In the following section it will be sketched how these parameters can be calculated.

2.3 Solving Maxwells equations

To get the dispersion characteristics (ω versus β) of the fiber structure Maxwell's equations have to be solved: Decoupling Maxwell's equations with no free charges and currents, assuming linear response of the medium and no losses leads to a wave equation for the $\mathbf{H}_\omega(\mathbf{r})$ field

$$\nabla \times \left[\frac{1}{\varepsilon(\mathbf{r})} \nabla \times \mathbf{H}_\omega(\mathbf{r}) \right] = \left(\frac{\omega}{c} \right)^2 \mathbf{H}_\omega(\mathbf{r}) \quad (2.4)$$

where ε is the dielectric function. Here the fields have been expanded into a set of harmonic modes $\mathbf{H}_\omega(\mathbf{r}, t) = \text{Re}(\mathbf{H}_\omega(\mathbf{r})e^{-i\omega t})$ with frequency ω . This can be done without further loss of generality since Maxwell's equations have already been assumed linear [6, 8]. Because of translational symmetry along the z-axis the dielectric function only depends on (x, y) , consequently the harmonic modes can be expressed on the following form:

$$\mathbf{H}_\omega(\mathbf{r}) = \sum_m \alpha_m \mathbf{h}_m(x, y) e^{-i\beta^{(m)}(\omega)z}, \quad (2.5)$$

where m denotes the m th eigenmode with transverse part $\mathbf{h}_m(x, y)$ and propagation constant $\beta^{(m)}(\omega)$. After expanding in a plane wave basis the matrix eigenvalue problem is solved leading to the (fully vectorial) eigenmodes. The

method is described in [6, 38]. Johnson and Joannopoulos have developed a freely available code, to solve Maxwell's equations [39]. With this code and a dielectric function based on the SEM-image of Fig. 2.2 Niels Asger Mortensen and Jes Broeng from Crystal Fibre have calculated the transverse part $h_m(x, y)$ of the eigen modes and propagation constants $\beta^{(m)}(\omega)$ [40].

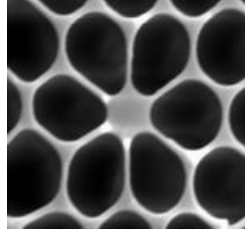


Figure 2.2: SEM-image of the endface of a PCF with a core diameter of $1.7\mu\text{m}$. Picture provided by Crystal Fibre A/S.

2.3.1 Dispersion properties

Both the material dispersion of silica and the dispersion due to the micro-structuring of the fibers contribute to the effective refractive index of the fundamental mode

$$n_{\text{eff}} = n_{\text{material}} + n_{\text{eff,bandstructure}} - n_{\text{constant}}, \quad (2.6)$$

The effective propagation constant β of the fundamental mode can subsequently be found from Eq. (2.1) by inserting n_{eff} .

The refractive index of silica n_{material} has been calculated from the Sellmeier formula

$$n_{\text{material}}^2(\lambda) = 1 + \sum_{j=1}^p \frac{B_j^2}{1 - (\frac{\lambda_j}{\lambda})^2}, \quad (2.7)$$

where λ_j is an atomic resonance in the fused silica. For the calculations the parameters given in [41] have been used: $B_1 = 0.6961663$, $B_2 = 0.4079426$, $B_3 = 0.8974794$, $\lambda_1 = 0.0684043\mu\text{m}$, $\lambda_2 = 0.1162414\mu\text{m}$, $\lambda_3 = 9.896161\mu\text{m}$.

The contribution to the effective refractive index from the micro-structuring $n_{\text{eff,bandstructure}}$, has been calculated by assuming a frequency independent refractive index of silica ($n_{\text{constant}} = 1.45$) in the dielectric function $\varepsilon(x, y)$ in Eq. (2.4). By solving the equation the propagation constant of the fundamental mode $\beta^{(1)}$ is found, giving $n_{\text{eff,bandstructure}} = c\beta^{(1)}/\omega$.

To include the contribution to n_{eff} from silica only once, the constant offset n_{constant} in Eq. (2.6) is introduced. In fact this constant term will have no impact on the simulations in the following chapters, since a frame of reference moving with the group velocity of the propagating pulse is chosen.

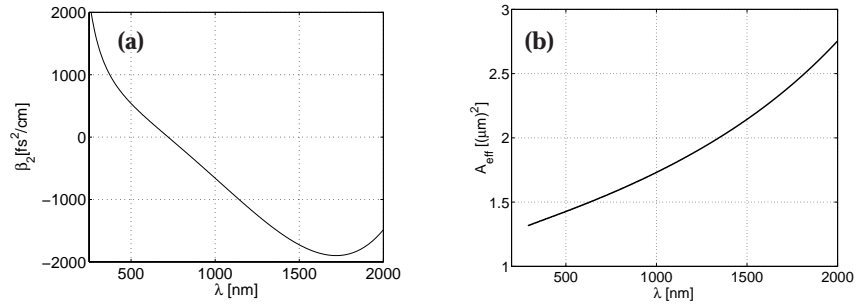


Figure 2.3: Dispersion characteristics for the fundamental frequency mode of the 1.7 μm core diameter PCF shown in Fig. 2.2. (b) Effective area of the same fiber. Calculations carried out by Niels Asger Mortensen / Jes Broeng from Crystal Fibre A/S.

Based on a SEM-picture of the fiber end face shown in Fig. 2.2 the propagation constant of the shown 1.7 μm core diameter PCF has been calculated using the method sketched above. The group velocity dispersion β_2 , calculated from the propagation constant, is shown on Fig. 2.3 (a). A mode corresponding to the other polarization state exists, but in the calculations presented in the following chapters only propagation in one polarization mode will be considered, even though for example the fiber on Fig. 2.2 is not polarization maintaining.

The frequency dependency of the refractive index of silica can also be taken into account initially through a frequency dependent dielectric function $\varepsilon(x, y, \omega)$. Equation (2.4) then has to be solved self consistently. When comparing the two methods no major differences appear.

2.3.2 Effective area

An effective area of a mode in a fiber can be defined as [40, 41]

$$A_{\text{eff},n}(\omega) = \frac{[\int dx dy |\mathbf{h}_n(x, y)|^2]^2}{\int dx dy |\mathbf{h}_n(x, y)|^4}, \quad (2.8)$$

where $|\mathbf{h}_n(x, y)|^2$ is proportional to the intensity distribution in the fiber. Figure 2.3 (b) shows the effective area of the fundamental mode for the 1.7 μm core diameter PCF. It is the high index contrast between silica and air that makes the relatively low effective areas in PCFs possible [40].

2.4 Conclusion

The transverse micro-structuring makes the dispersion of the fibers highly tunable and together with the high index contrast it leads to the small effective area,

making high intensities in the fibers possible. Due to the high intensities a cascade of nonlinear effects can take place in the fibers. The interplay between the special dispersion of the fibers and these nonlinear effects makes the phenomenon of supercontinuum generation possible. Chapter 4 and 5 will be devoted to investigations of supercontinuum generation.

Above, the linear Maxwell's equations have been solved for the transverse structure of the fibers. Although the problem is nonlinear in its nature when high intensities are involved, the method provides information about the propagation constant and the effective transverse area of the mode. These parameters will serve as input in the nonlinear model for wave propagation along the length of the fiber. The model will be presented in the following chapter and will subsequently be used to describe the generation of supercontinua in the fibers.

CHAPTER 3

Model for wave propagation in photonic crystal fibers

In this chapter it will be sketched how Maxwell's equations together with a suitable set of approximations lead to a nonlinear Schrödinger equation as a governing equation for light propagation in PCFs. Subsequently several ways of treating the dispersion and the nonlinearity will be treated. Finally the numerical implementation will be addressed.

3.1 Introduction

The theoretical modelling of light propagation in the PCFs is needed, not only to get a good understanding of the processes taking place in supercontinuum generation, but also to give input to the design and development of new fiber structures and applications.

A dedicated effort has been given to the understanding of supercontinuum generation in the PCFs, as can be seen from the substantial amount of publications already on the subject. For modelling the propagation of light in the fibers a nonlinear Schrödinger equation has been applied [42–49].

A general version of the nonlinear Schrödinger equation that takes the Raman effects, the frequency dependence of the nonlinearity and the full dispersion properties into account is presented in this chapter together with simplified versions of the equation. Numerical implementation and subsequent comparison with experimental data illustrates the power of the model, suggesting that the behavior of “theoretical”, not yet produced fibers can be predicted. The model therefore provides a strong and flexible tool for the understanding and further development of the fibers. The derivation here much follows the lines of derivations used for the propagation in conventional fibers [41, 50–52].

3.2 The nonlinear Schrödinger equation

The simplest form of the nonlinear Schrödinger equation is given by

$$\frac{d}{dz}A = -i\frac{\beta_2}{2}\frac{\partial^2}{\partial t^2}A + i\gamma|A|^2A, \quad (3.1)$$

and it will be derived in the Sec. 3.3. On the way to the equation above a more general version of the nonlinear Schrödinger equation will be found. The first term describes the second order dispersion determined by the material and the geometrical structure of the fiber as described in the previous chapter. The second term is the nonlinearity, which depends upon the polarizability of the material through $\chi^{(3)}$ and scales with the third power of the electric field. As mentioned in Chap. 2 the PCFs can be designed to have a fundamental mode with a small transverse area resulting in high intensities inside the fiber, therefore nonlinear phenomena play important roles in the description of the fibers.

The nonlinear Schrödinger equation has been applied in fiber optics since the beginning of the eighties, where it was used to describe Mollenauer’s first experimental observations of solitons in optical fibers [53]. Solitons emerge as fundamental solutions to the nonlinear Schrödinger equation because the dispersion term can balance the nonlinear term. With respect to supercontinuum generation in PCFs, soliton formation and decay play important roles, as will be described in Sec. 4.3.

A nonlinear Schrödinger equation appears in other branches of physics as well. In quantum optics the Gross-Pitaevskii equation is used to describe the

evolution of the Bose-Einstein condensate ground state wave function. Bose-Einstein condensates in optical lattices will be described in Chap. 6 and 7.

3.3 Derivation of a nonlinear Schrödinger equation

Decoupling Maxwell's equations with no free currents and charges gives the following wave equation for the electric field $\mathbf{E}(\mathbf{r}, t)$

$$\nabla \times \nabla \times \mathbf{E}(\mathbf{r}, t) = -\frac{1}{c^2} \frac{\partial^2}{\partial t^2} \mathbf{E}(\mathbf{r}, t) - \mu_0 \frac{\partial^2}{\partial t^2} \mathbf{P}(\mathbf{r}, t), \quad (3.2)$$

where $\mathbf{P}(\mathbf{r}, t)$ is the polarization, having a contribution from the linear polarization with susceptibility $\chi^{(1)}(t - t_1)$ and a contribution from the nonlinear polarization with susceptibility $\chi^{(3)}$, in the following approximated by

$$\chi^{(3)}(t - t_1, t - t_2, t - t_3) = \chi^{(3)} g(t - t_1) \delta(t - t_2) \delta(t - t_3). \quad (3.3)$$

Through the delay-function $g(t - t_1)$ the interaction of the light with the vibrational modes of silica can be included in the description (Raman scattering). $\chi^{(3)}(t - t_1, t - t_2, t - t_3)$ can be approximated by a product of three delta functions if only the electronic response of the material is wanted, since it is almost instantaneous, in which case one speaks of a Kerr nonlinearity. Because of inversion symmetry of the fibers the second order polarization disappears.

Further the induced charges at the surfaces between air and silica are neglected, corresponding to assuming $\nabla \cdot \mathbf{E}(\mathbf{r}, t) = 0$ which leads to the following approximation

$$\nabla \times \nabla \times \mathbf{E}(\mathbf{r}, t) = \nabla(\nabla \cdot \mathbf{E}(\mathbf{r}, t)) - \nabla^2 \mathbf{E}(\mathbf{r}, t) \simeq -\nabla^2 \mathbf{E}(\mathbf{r}, t). \quad (3.4)$$

Transforming to the frequency domain Using the following convention for Fourier transforms

$$\tilde{\mathbf{E}}(\mathbf{r}, \omega) = \int_{-\infty}^{\infty} dt e^{i\omega t} \mathbf{E}(\mathbf{r}, t) \quad (3.5)$$

and the above listed approximations the wave equation 3.2 can be transformed to frequency space

$$\nabla^2 \tilde{\mathbf{E}}(\mathbf{r}, \omega) + \varepsilon(x, y, \omega) \frac{\omega^2}{c^2} \tilde{\mathbf{E}}(\mathbf{r}, \omega) = -\mu_0 \omega^2 \tilde{\mathbf{P}}_3(\mathbf{r}, \omega) \quad (3.6)$$

where

$$\mathbf{P}_3(\mathbf{r}, t) = \varepsilon_0 \chi^{(3)} \mathbf{E}(\mathbf{r}, t) \int_{-\infty}^{\infty} dt_1 g(t - t_1) \mathbf{E}^2(\mathbf{r}, t_1) \quad (3.7)$$

and $\varepsilon(x, y, \omega) = 1 + \chi^{(1)}(x, y, \omega)$. As used in Chap. 2 the dielectric function does not depend on the z coordinate because of translational symmetry along the z-axis.

Separating the electric field By assuming weak coupling between the transverse and longitudinal degrees of freedom through the nonlinearity, the electric field can to a good approximation be separated into a product of a function with longitudinal dependence $\tilde{G}(z, \omega)$ and a function with transversal dependence $\tilde{h}(x, y, \omega)$ [50, 51]. Furthermore the fields are assumed to be linearly polarized along the vector \mathbf{x}

$$\tilde{\mathbf{E}}(\mathbf{r}, \omega) = \mathbf{x} \frac{\tilde{h}(x, y, \omega)}{\sqrt{S(\omega)}} \tilde{G}(z, \omega), \quad (3.8)$$

where the normalization factor $S(\omega)$ is given by

$$S(\omega) = \int dx dy |\tilde{h}(x, y, \omega)|^2. \quad (3.9)$$

Equation 3.6 is separated into the following two equations

$$\nabla_{\perp}^2 \tilde{h}(x, y, \omega) + \varepsilon(\mathbf{r}, \omega) \frac{\omega^2}{c^2} \tilde{h}(x, y, \omega) = \beta(\omega)^2 \tilde{h}(x, y, \omega), \quad (3.10)$$

$$\frac{d^2}{dz^2} \tilde{G}(z, \omega) + \beta(\omega)^2 \tilde{G}(z, \omega) = -\frac{\omega^2}{c^2} \frac{\chi^{(3)}}{A_{\text{eff}}(\omega)} \tilde{p}(z, \omega). \quad (3.11)$$

The z-dependent nonlinear polarization is now given by

$$\begin{aligned} \tilde{p}(z, \omega) &= \left(\frac{1}{2\pi}\right)^2 \int d\omega_1 \int d\omega_2 \tilde{g}(\omega_1 - \omega_2) \\ &\quad \times \tilde{G}(z, \omega - \omega_1 + \omega_2) \tilde{G}^*(z, \omega_2) \tilde{G}(z, \omega_1), \end{aligned} \quad (3.12)$$

$$p(z, t) = G(z, t) \int dt_1 g(t - t_1) G(z, t_1)^2. \quad (3.13)$$

In the transverse equation (3.10) the nonlinearity has been completely ignored. In the longitudinal equation (3.11) the effective area $A_{\text{eff}}(\omega)$ below is introduced when integrating out the transverse degrees of freedom.

$$A_{\text{eff}}(\omega) = \frac{(\int dx dy |\tilde{h}(x, y, \omega)|^2)^2}{\int dx dy |\tilde{h}(x, y, \omega)|^4}. \quad (3.14)$$

Equation Eq. (3.11) can in principle be implemented directly using for example a Finite Difference Time Domain method (FDTD) [54, 55], but it is numerically heavy.

Approximating second derivative The real electric field $G(z, t)$ can always be written as

$$G(z, t) = \text{Re}[G_+(z, t)] = \frac{1}{2}[G_+(z, t) + G_-(z, t)], \quad (3.15)$$

where $G_-(z, t) = G_+(z, t)^*$. The Fourier transform of $G(z, t)$ can be written as the transform of the respective components as defined by Eq. (3.5)

$$\tilde{G}(z, \omega) = \frac{1}{2}[\tilde{G}_+(z, \omega) + \tilde{G}_-(z, \omega)] = \frac{1}{2}[\tilde{U}_+(z, \omega)e^{i\beta z} + \tilde{U}_-(z, \omega)e^{-i\beta z}]. \quad (3.16)$$

Here the field has been written as a sum of a forward $e^{i\beta z}$ and backward $e^{-i\beta z}$ propagating wave. For them to be distinguished and treated independently the wavepacket needs to consist of an interval of wavevectors, which is the case if the field can be described within a slowly varying envelope. If the forward and backward propagating waves can be distinguished the following approximation for the second derivative with respect to z can be made

$$\begin{aligned} \left(\frac{d^2}{dz^2} + \beta(\omega)^2\right)\tilde{G}_+(z, \omega) &= \left(\frac{d}{dz} + i\beta(\omega)\right)\left(\frac{d}{dz} - i\beta(\omega)\right)\tilde{G}_+(z, \omega) \\ &\simeq 2i\beta(\omega)\left(\frac{d}{dz} - i\beta(\omega)\right)\tilde{G}_+(z, \omega). \end{aligned} \quad (3.17)$$

Inserting $G(z, t)$ in the polarization and collecting all terms effectively propagating forward leads to the following equation

$$\begin{aligned} \frac{d}{dz}\tilde{G}_+(\omega) &= i\beta(\omega)\tilde{G}_+(\omega) \\ &+ \frac{\omega^2}{c^2} \frac{\chi^{(3)}}{8A_{\text{eff}}(\omega)\beta(\omega)} \int_{-\infty}^{\infty} dt e^{i\omega t} \int_{-\infty}^{\infty} dt_1 g(t - t_1) \\ &\times \{2G_+(t)G_+(t_1)G_-(t_1) + G_-(t)G_+(t_1)G_+(t_1) \\ &+ G_+(t)G_+(t_1)G_+(t_1)\}, \end{aligned} \quad (3.18)$$

where the z -dependence of G has been omitted. Had a plane wave $G(z, t) = Re[e^{i(\beta_0 z - \omega_0 t)}]$ been considered and the time dependence on t_1 ignored, all terms above would be proportional to $e^{-i\omega_0 t}$ except the last term $G_+(t)G_+(t_1)G_+(t_1)$, which would be proportional to $e^{-i3\omega_0 t}$ corresponding to third harmonic generation.

For the approximation to be consistent the term corresponding to third harmonic generation has to be neglected, since the coupling from the forward propagating component (ω_0) to the third harmonic ($3\omega_0$) is in principle the same as between the forward (ω_0) and backward ($-\omega_0$) propagating components.

Shift of central wavelength It is numerically practical to center the spectrum around ω_0 defining a new frequency variable $\omega_1 = \omega - \omega_0$. The new field is defined as $G'_+(t) = G_+(t)e^{i\omega_0 t}$. Shifting the center frequency does not imply a further approximation. The essential approximation was made above where the forward and backward propagating waves were assumed distinguishable. It has been argued [50] that the approximation is valid for spectra as broad as $\omega_0/3$. The simulations carried out in the following chapters go beyond this limit and still provide reasonable results.

In the following equation a coordinate transformation to a frame of reference moving with velocity $1/\beta_1$ is made with $z' = z$, $t' = t - \beta_1 z$, $d/dz = d/dz' - \beta_1 d/dt'$

$$\begin{aligned} \frac{d}{dz'} \tilde{G}'_+(\omega_1) &= i(\beta(\omega) - \beta_1 \omega) \tilde{G}'_+(\omega_1) \\ &+ \frac{\omega}{c} \frac{\chi^{(3)}}{8A_{\text{eff}}(\omega)n_0} \int_{-\infty}^{\infty} dt' e^{i\omega_1 t'} \int_{-\infty}^{\infty} dt'_1 g(t' - t'_1) \\ &\times \{2G'_+(t')|G'_+(t'_1)|^2 + G'^*_+(t')G'^2_+(t'_1)e^{i2\omega_0(t'-t'_1)}\}. \end{aligned} \quad (3.19)$$

The propagation constant in the nonlinear term has here been approximated by $\beta(\omega) = n_0\omega/c$, where $n_0 = n_{\text{eff}}(\omega_0)$.

Units of electric field The input electric field can be written as

$$G'(z', t') = \bar{G}u(z', t'), \quad (3.20)$$

where $u(z, t)$ is expressed in dimensionless units. An effective power P of the light in the fiber is then given by

$$P = \frac{1}{2} \varepsilon_0 n_0 c |\bar{G}|^2, \quad (3.21)$$

Consequently, by introducing the field

$$A(z', t') = \sqrt{P}u(z', t') = \sqrt{\frac{\varepsilon_0 n_0 c}{2}} \bar{G}u(z', t') = \sqrt{\frac{\varepsilon_0 n_0 c}{2}} G'(z', t'), \quad (3.22)$$

the electric field is expressed in units of power. The propagation equation for the field A is then given by

$$\begin{aligned} \frac{d}{dz} \tilde{A}(\omega_1) &= i(\beta(\omega) - \beta_1 \omega) \tilde{A}(\omega_1) \\ &+ i\gamma(\omega) \int_{-\infty}^{\infty} dt e^{i\omega_1 t} A(t) \\ &\times \int_{-\infty}^{\infty} dt_1 g(t - t_1) |A(t_1)|^2, \end{aligned} \quad (3.23)$$

where the primes on the t, z coordinates have simply been removed, but the moving frame of reference is retained. A term $A(t)^* A(t_1)^2 e^{i2\omega_0(t-t_1)}$ has been approximated with $A(t)|A(t_1)|^2$. The convention in [41, 56] for the real part of the nonlinear refractive index $n_2 = \frac{3\chi^{(3)}}{4\varepsilon_0 c n_0^2}$ has been used. For the nonlinearity factor the convention suggested in [41] has been followed

$$\gamma(\omega) = \frac{n_2 \omega}{c A_{\text{eff}}(\omega)}. \quad (3.24)$$

Eq. (3.23) can be directly implemented. The following sections will go through various ways of treating the dispersion and the nonlinearity in the equation.

3.4 Dispersion

The propagation constant can be achieved either from calculations or experimental investigations of the fiber and is often expressed in terms of a Taylor expansion

$$\beta(\omega) = n_{\text{eff}}(\omega)\omega/c = \sum_m \frac{1}{m!} \beta_m (\omega - \omega_0)^m; \quad \beta_m = \left. \frac{\partial^m \beta}{\partial \omega^m} \right|_{\omega=\omega_0}. \quad (3.25)$$

Any dispersion profile can be fitted with a Taylor polynomial, the question is only how many terms are needed to make a good fit over the width of the spectrum.

3.4.1 Calculation of the propagation constant

The propagation constant $\beta(\omega)$ appearing in Eq. (3.11) can be found via the calculations presented in Chap. 2. The linear part of Eq. (3.11)

$$\frac{d^2}{dz^2} \tilde{G}(z, \omega) = -\beta(\omega)^2 \tilde{G}(z, \omega), \quad (3.26)$$

and Eq. (2.4) both originate from Maxwell's linear equations. By considering the magnetic field $\mathbf{H}_\omega(\mathbf{r})$ as given by Eq. (2.5) and taking the second derivative with respect to z the following equation arises

$$\frac{d^2}{dz^2} \mathbf{H}_\omega(\mathbf{r}) = -\beta(\omega)^2 \mathbf{H}_\omega(\mathbf{r}). \quad (3.27)$$

The magnetic and electric fields are related by

$$\mathbf{E}_\omega(\mathbf{r}) = -\frac{ic}{\omega \varepsilon(x, y)} \nabla \times \mathbf{H}_\omega(\mathbf{r}), \quad (3.28)$$

where with translational symmetry $\varepsilon(x, y)$ is independent of z . Consequently, $\mathbf{E}_\omega(\mathbf{r})$ also fulfills Eq. (3.26) and $\beta(\omega)$ in this and the previous chapter is the same.

3.4.2 Experimentally measured dispersion

A white-light interferometer [57] can be used to measure the second order dispersion of the PCFs. The Femtosecond Chemistry group has build such an interferometer and measured the fiber dispersion $\beta_2(\omega)$, which can be integrated to give the propagation constant. The integration constants will not have influence on the propagation simulations, since the evolution of the pulses is followed in a frame moving with the group velocity of the pulse. Calculated and measured dispersion can be compared and the importance of the deviation can be revealed by the simulations described in this chapter.

3.5 Nonlinear effects

As mentioned, Eq. (3.23) can be implemented directly as it is including both full frequency dependency of the propagation constant and the effective area as well as self-steepening and Raman effects.

3.5.1 Raman response

For the Raman response function the expression $g(t) = (1 - f_R)\delta(t) + f_R g_R(t)$ has been used, where the delta function term originates from the electronic response i.e. the Kerr interaction and the last term takes the Raman scattering into account. The function $g_R(t)$ can be chosen on the form

$$g_R(t) = \frac{\tau_1^2 + \tau_2^2}{\tau_1 \tau_2^2} e^{-t/\tau_2} \sin(t/\tau_1); t > 0, \quad (3.29)$$

$$g_R(t) = 0; t < 0, \quad (3.30)$$

as given by [50]. Raman scattering can be explained as scattering of light on the optical phonons and $1/\tau_1$ gives the optical phonon frequency. $1/\tau_2$ gives the bandwidth of the Lorentzian line. The same values as in [41] have been applied for the constants: $\tau_1 = 12.2 fs$, $\tau_2 = 32 fs$, $f_R = 0.18$.

3.5.2 Nonlinearity factor γ

The frequency dependent nonlinearity factor $\gamma(\omega)$ in Eq. (3.24) is found from the effective area $A_{\text{eff}}(\omega)$ as calculated in Chap. 2.

Since the effective area $A_{\text{eff}}(\omega)$ often does not vary too drastically with frequency as seen on Fig. 2.3 (b) a valuable approximation is to assume the effective area to be constant $A_{\text{eff},0}$. With this approximation the nonlinearity factor can be written as

$$\gamma(\omega) = \frac{n_2 \omega}{c A_{\text{eff},0}} = \gamma_0 \left(1 + \frac{\omega_1}{\omega_0}\right), \quad (3.31)$$

where $\omega_0 = \omega - \omega_1$ is the frequency of the input pulse and $\gamma_0 = \frac{n_2 \omega_0}{c A_{\text{eff},0}}$. With this nonlinearity factor the nonlinear Schrödinger equation is given by

$$\begin{aligned} \frac{d}{dz} \tilde{A}(\omega_1) &= i(\beta(\omega) - \beta_1 \omega) \tilde{A}(\omega_1) + i\gamma_0 \left(1 + \frac{\omega_1}{\omega_0}\right) \\ &\times \int_{-\infty}^{\infty} dt e^{i\omega_1 t} A(t) \int_{-\infty}^{\infty} dt_1 g(t - t_1) |A(t_1)|^2, \end{aligned} \quad (3.32)$$

and this equation will be used extensively for the simulations in the following two chapters.

In the time domain the nonlinearity factor above is given by $\gamma_0(1 + i\frac{1}{\omega_0}\frac{\partial}{\partial t})$, where the time derivative takes self-steepening and shock formation into account. Consequently, for very long pulses this time derivative can be omitted corresponding to assuming a constant nonlinearity factor

$$\gamma(\omega) = \gamma_0. \quad (3.33)$$

If the computational grid is centered at a frequency ω_c different from the central frequency of the pulse ω_0 the nonlinearity factor has to be changed accordingly

$$\gamma_0 = \frac{n_2\omega_c}{cA_{\text{eff},0}}.$$

3.5.3 Kerr nonlinearity

A Kerr nonlinearity can be assumed by ignoring the Raman response in the fibers corresponding to setting $g(t) = \delta(t)$. If the nonlinearity factor is assumed constant $\gamma = \gamma_0$ the following equation arises

$$\frac{d}{dz}\tilde{A}(\omega_1) = i(\beta(\omega) - \beta_1\omega)\tilde{A}(\omega_1) + i\gamma_0 \int_{-\infty}^{\infty} dt e^{i\omega_1 t} A(t)|A(t)|^2. \quad (3.34)$$

If all terms are transformed to the time domain and only up to second order dispersion is taken into account the following equation appears

$$\frac{d}{dz}A(t) = -i\frac{\beta_2}{2}\frac{\partial^2}{\partial t^2}A(t) + i\gamma|A|^2A(t). \quad (3.35)$$

This is exactly the simple form of the nonlinear Schrödinger equation (3.1) stated in the beginning of this chapter.

3.5.4 Overview of approaches to the nonlinearity

Most of the approximations mentioned in this section can be applied independently

- Response function $g(t)$:
 - Raman scattering $g(t) = (1 - f_R)\delta(t) + f_R g_R(t)$.
 - Kerr nonlinearity $g(t) = \delta(t)$.
- Nonlinearity factor $\gamma(\omega) = \frac{n_2\omega}{cA_{\text{eff}}(\omega)}$:
 - Effective area: Frequency dependent $A_{\text{eff}}(\omega)$ or constant $A_{\text{eff},0}$.
 - Self-steepening and shock formation: Included $\omega = \omega_0(1 + \omega_1/\omega_0)$ or not included $\omega = \omega_0$.

Which method to choose is a question of computational time, available input data for $\beta(\omega)$ and $A_{\text{eff}}(\omega)$ and of the physical regime. Generally, for short pulses (<100 fs), high intensities (10^{11} W/cm²) and short propagation lengths (a few cm) the error done by neglecting the Raman response of the material is limited (but is still there). For short pulses and high intensities the spectra generally get broad because of self-phase modulation, consequently it is important to include the frequency dependence of $\beta(\omega)$ and the effects of self-steepening and shock formation as in Eq. (3.32).

3.6 Computational methods

The equations have been implemented with the split step method with 4th order Runge Kutta steps for the nonlinearity. The dispersion is calculated in the frequency domain. For the Fourier transformations the FFTW library has been used [58]. The nonlinearity has been calculated implementing the two following approaches:

A: Direct integration of Raman response in the time domain.

In the first implementation of Eq. (3.32) the self-steepening term and the Raman response integral were both evaluated in the time domain

$$\begin{aligned} \frac{d}{dz} \tilde{A}(\omega_1) &= i(\beta(\omega) - \beta_1 \omega) \tilde{A}(\omega_1) \\ &+ \int_{-\infty}^{\infty} dt e^{i\omega_1 t} i\gamma_0 \left(1 + i \frac{1}{\omega_0} \frac{\partial}{\partial t} \right) A(t) \\ &\times \int_{-\infty}^{\infty} dt_1 g(t - t_1) |A(t_1)|^2, \end{aligned} \quad (3.36)$$

The time derivative was explicitly evaluated as

$$\frac{\partial Y}{\partial t} \rightarrow (Y[i+1] - Y[i-1])/2\Delta t \quad (3.37)$$

In the Raman response integral only the interval of response times from $t-t_1 = 0$ to 300 fs was included, since the influence of the Raman response beyond this time is very limited.

B: Calculation of the Raman response convolution integral in the frequency domain.

An alternative approach is to compute the Raman response integral by evaluating the convolution in the frequency domain. Additionally, the time-derivative was evaluated by multiplying with the frequency in the frequency domain. The

nonlinear term

$$X(\omega_1) = i\gamma_0 \left(1 + \frac{\omega_1}{\omega_0}\right) \mathcal{F} \left\{ (1 - f_R)A(t)|A(t)|^2 + f_RA(t) \int_{-\infty}^{\infty} dt_1 g_R(t - t_1)|A(t_1)|^2 \right\}, \quad (3.38)$$

could consequently be evaluated by making Fourier transformations \mathcal{F}

$$Y(\omega_1) = \mathcal{F}\{Y(t)\} = \int_{-\infty}^{\infty} dt e^{i\omega_1 t} Y(t), \quad (3.39)$$

and inverse transformations \mathcal{F}^{-1}

$$Y(t) = \mathcal{F}^{-1}\{Y(\omega_1)\} = \frac{1}{2\pi} \int_{-\infty}^{\infty} d\omega_1 e^{-i\omega_1 t} Y(\omega_1). \quad (3.40)$$

For each step dz the following transformations need to be carried out

$$Y(\omega_1) = \mathcal{F}\{|A(t)|^2\}, \quad (3.41)$$

$$g_R(\omega_1) = \mathcal{F}\{g_R(t)\}, \quad (3.42)$$

$$I(t) = \int_{-\infty}^{\infty} dt_1 g_R(t - t_1)|A(t_1)|^2 = \mathcal{F}^{-1}\{Y(\omega_1)g_R(\omega_1)\}, \quad (3.43)$$

$$M(\omega_1) = \mathcal{F}\{(1 - f_R)A(t)|A(t)|^2 + f_RA(t)I(t)\}, \quad (3.44)$$

$$X(\omega_1) = \gamma_0 \left(1 + \frac{\omega_1}{\omega_0}\right) M(\omega_1). \quad (3.45)$$

Method B is by far the fastest and most accurate since the time derivative and the Raman response integral are treated as exact as possible with the given discretization. In the following two chapters comparisons between the two implementations will be given since unfortunately there is a small difference between the two, mainly due to the evaluation of the time derivative in Eq. (3.37).

3.6.1 Scaling

The computation of the Fourier transformations scales as $O(N \log N)$, where N is the number of points in the grid. The z -step size depends on input intensity, the higher the intensity, the faster is the dynamics consequently the more z -steps are needed to propagate the same distance.

3.7 Conclusion

Starting with Maxwell's equations it has been sketched how a nonlinear Schrödinger equation for wave propagation in the PCFs can be achieved. The full frequency dependency of the propagation constant as well as the effective transverse area

serve as input for the model and these parameters can either be calculated as sketched in Chap. 2 or measured. The model includes the instantaneous nonlinear response of silica. Additionally, the effects of Raman scattering, self-steepening and shock formation can be included. In the following chapter most of the simulations shown will be based on Eq. (3.32) and the influence of the nonlinear effects will be investigated by comparison with the simpler version Eq. (3.34).

CHAPTER 4

Supercontinuum generation

When a PCF is pumped with femtosecond pulses a supercontinuum is formed and the physical mechanisms at play in this process are investigated in this chapter. Simulations based on the model presented in the previous chapter serve to explain the scenario taking place when pulses propagate in the fibers. Subsequently the simulations are compared to experiments with good agreement. This chapter is mainly based on the article [III].

4.1 Introduction

The generation of very broad spectra, called supercontinua, in PCFs has attracted much attention since Ranka et al. [37] demonstrated the first supercontinua in PCFs using low power titanium-sapphire laser pulses [59]. Supercontinua have previously been generated in gases, liquids, conventional and speciality fibers. One advantage of using PCFs for supercontinuum generation is the small effective area of the mode, leading to high intensities in the fibers. Consequently, nonlinear processes involved in the supercontinuum generation can be significant even for relatively low pulse energies on the order of pJ for femtosecond pulses. Input ranging from the continuous wave regime [60] all the way to femtoseconds has been used. An additional advantage of the PCFs is the unique dispersion of the fibers, effectively determining the dynamics of the supercontinuum generation, one of the reasons being the possibility to control the phase-matching of several nonlinear processes.

In general, supercontinuum generation is based on a cascade of nonlinear processes well known from nonlinear optics like four-wave mixing, stimulated Raman scattering and soliton dynamics. Today the generation can be controlled to a great extent by tailormade dispersion and appropriate choice of input parameters [43–45, 47–49, 61, 62].

A specific example of supercontinuum generation is given on Fig. 4.1 where a $1.7\ \mu\text{m}$ core diameter PCF is pumped with 50 fs pulses at a wavelength of 800 nm. After ~ 20 cm of propagation the emerging light is projected on a screen as shown on the pictures. Going from (a) to (c) the input intensity increases and the spectrum broadens. At the center of Fig. 4.1 (c) white light corresponding to a supercontinuum is generated. The remote field reveals the hexagonal microstructuring of the fiber.

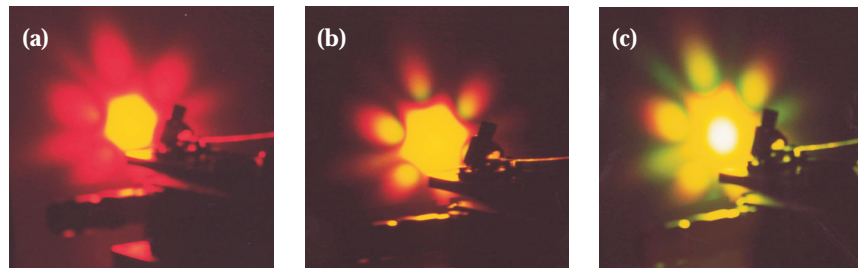


Figure 4.1: Supercontinuum generation in the $1.7\ \mu\text{m}$ core diameter PCF pumped with 50 fs pulses at a wavelength of 800 nm. Input power is increasing from (a) to (c).

In this and the following chapter focus will be on the femtosecond regime, the regime in which supercontinua were first generated [37] and for which a substantial amount of literature exists [44–49, 61, 63–67], [III, IV]. For a typical PCF with a single zero dispersion wavelength, pumped in the anomalous dis-

persion regime, the dynamics of the supercontinuum generation is dominated by the decay of higher order solitons emitting phase-matched radiation and this will be discussed in detail in the present chapter. For a fiber with a dispersion profile with two closely lying zero dispersion wavelengths the dynamics is dominated by four wave mixing instead and the scenario in this type of fiber will be discussed in Chap. 5.

Supercontinua have also been generated with pico-second and nano-second pulses [44]. The nonlinear Schrödinger equation has been used to describe the generation of supercontinua with pulses up to 60 ps long [42, 43]. 600 ps pulses generated by Q-switching is treated in [68].

For the generation of supercontinua in the nano-second regime stimulated Raman scattering as well as phase-matched four wave mixing play central roles. In fact a PCF pumped with 2-3 ns pulses has already been used by Koheras [69] in collaboration with the Helsinki University of Technology to make a commercially available white-light source.

Recently, supercontinua generated from continuous waves with powers of 1.2-1.8 W were treated [60]. For these relatively high powers modulational instabilities cause the light to break up into solitons and in combination with intrapulse stimulated Raman scattering the spectrum is broadened. The solitons can subsequently emit phase-matched non-solitonic radiation, the same process as seen for the femtosecond pulses.

In general the importance of phase-matched processes such as four wave mixing increases with decreasing bandwidth of the pulses, corresponding to increasing length of the pulses. Another general tendency is, the higher the power, the broader the spectrum. The nonlinear response increases with increasing intensity and it is consequently easier to address the various nonlinear effects.

Recently the coherence properties and the influence of noise on the spectra have been discussed. The input shot noise as well as the spontaneous Raman scattering is amplified in the fibers. Short propagation lengths together with short input pulses minimize the buildup of the noise [36, 63, 70].

4.2 Applications

Probably the most important application of supercontinua generated in PCFs has been in frequency metrology [33, 34, 71]. When a supercontinuum is generated in a PCF with femtosecond pulses, the resulting spectrum consists of a comb of frequencies with equal spacing given by the laser repetition rate. Since the spectra can be made octave spanning, a frequency and the approximate double frequency exist in the spectrum and by beating the second harmonic of the lower frequency with the higher frequency a direct link between the repetition rate and the optical frequency can be made. Consequently, a precise optical frequency standard can be established. Systems providing such optical frequency standards are commercially available from a company related to the Munich group [72].

As mentioned the supercontinua have also found an application within the interferometric technique of optical coherence tomography, where they have lead to sub-micron resolution [35].

Another imaging technique where the supercontinua have been used as a light source is in coherent anti-Stokes Raman scattering (CARS) microscopy. The technique has been used by the Femto Chemistry group [II] and the principle of this four wave mixing process is illustrated in Fig. 4.2 (a). The photon with frequency ω_S is provided by the laser and the ω_P photons are generated in the PCF. When the energy difference $\omega_P - \omega_S$ corresponds to a vibrational transition $|1\rangle - |2\rangle$ in the sample, the signal with frequency ω_{AS} will be resonantly enhanced. The method has been used to achieve the picture of a yeast cell shown in Fig. 4.2 (b), where the C-H stretch vibrational transition at 3000 cm^{-1} is probed. The cell contour as well as structure inside the cell (organelles) is seen.

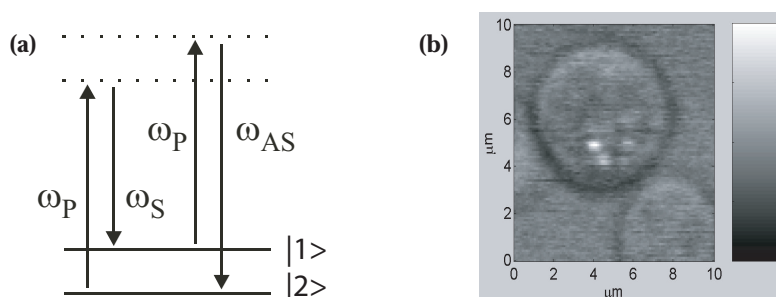


Figure 4.2: (a) Coherent anti Stokes Raman scattering. When the energy difference $\omega_P - \omega_S$ corresponds to a vibrational transition in the sample $|1\rangle - |2\rangle$ the signal with frequency ω_{AS} will be resonantly enhanced. (b) Picture of a yeast cell where the C-H stretch vibrational transition at 3000 cm^{-1} is probed. The cell contour as well as structure inside the cell (organelles) is clearly seen. The pictures are provided by Henrik Nørgaard Paulsen and Esben Ravn Andresen.

The supercontinua could serve as light sources for wavelength division multiplexing where broad, stable, flat spectra are desirable, for many channels to be carved out. The noise in the spectra are still a challenge to overcome [36] for the succes of this application.

The four wave mixing especially dominant in PCFs with two closely lying zero dispersion wavelengths could be used as basis for a blue light source as well as for wavelength converters. The dynamics in this type of fiber as well as the perspectives for compression of the spectra will be treated in the following chapter.

4.3 Physical processes in supercontinuum generation

This section gives a presentation of the various physical processes, which can play a role when a supercontinuum is formed in a PCF. The effects important

for the supercontinuum generation in the fiber shown in Fig. 2.2 will be emphasized, since the simulations presented in this chapter are done for this fiber.

4.3.1 Self phase and cross phase modulation

The nonlinear response of the silica arises due to optical pumping of the energy levels for the electrons in silica as well as saturation effects for the transitions. The effects are described through the nonlinear polarization with susceptibility $\chi^{(3)}$. The self-phase modulation (SPM) can be explained through the nonlinear part of the refractive index $n_2 I$. If the phase of the pulse is described by $\phi = \beta z - \omega_0 t = (n + n_2 I(t))\omega_0 z/c - \omega_0 t$ new frequency components are generated in the spectrum $\omega = -\partial\phi/\partial t = -\frac{n_2\omega_0 z}{c} \frac{\partial I(t)}{\partial t} + \omega_0$. The corresponding term in the nonlinear Schrödinger equation is $\gamma|A|^2 A$ (the Kerr nonlinearity), which is also responsible for the four wave mixing processes as well as cross phase modulation, where it is simply the intensity of an other frequency component, which is responsible for the modulation of the phase. For femtosecond pulses SPM plays an important role in the initial broadening of the spectra.

4.3.2 Solitons

The soliton is an exact solution to the nonlinear Schrödinger equation with Kerr nonlinearity and negative second order dispersion β_2 as given in Eq. (3.1) and it physically appears because the dispersion in the fiber is counteracted by SPM. The time evolution of an ideal third order soliton ($N = 3$) over 1 soliton period (z_0) is shown on Fig. 4.3. The soliton number and period being defined as [41]

$$N^2 = \frac{\gamma P_0 T_0^2}{|\beta_2|}, \quad (4.1)$$

$$z_0 = \frac{\pi T_0^2}{2 |\beta_2|}. \quad (4.2)$$

where $\gamma = n_2\omega/(cA_{\text{eff}})$ is again the nonlinear coefficient, $T_0 = T_{\text{FWHM}}/(2\ln(1 + \sqrt{2}))$ is the pulse duration and P_0 is the peak power. After the soliton period the pulse has reverted to its initial state as seen on Fig. 4.3, during the period the third order soliton contracts twice. If a fiber is pumped with a CW source in the anomalous dispersion regime, solitons can be generated as a consequence of modulational instability. Performing a linear stability analysis on the CW light in the fiber will reveal whether small modulations of the light will grow, corresponding to a modulational instability [41].

4.3.3 Higher order dispersion

Whereas higher order dispersion plays a minor role for pulse evolution in conventional fibers the special and often flat dispersion profiles often lead to high influence of the higher order dispersion terms.

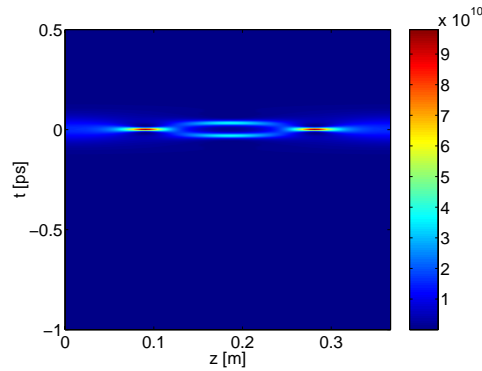


Figure 4.3: Propagation of a third order soliton.

The simulations in the left column of Fig. 4.4 are based on equation (3.34) using the full dispersion profile of the $1.7 \mu\text{m}$ core diameter fiber as shown on Fig. 2.2. The input pulses had $T_{\text{FWHM}}=100$ fs and were centered at $\lambda=836\text{nm}$ with an input intensity of $I_0 = 4.1 \times 10^{10}\text{W}/\text{cm}^2$ corresponding to a soliton number of 3.3. A constant effective area $A_{\text{eff}} = 2(\mu\text{m})^2$ and nonlinear refractive index $n_2 = 3 \times 10^{-20}\text{m}^2/\text{W}$ were used.

The frame of reference for the simulations can be chosen to move with any velocity. In Fig. 4.3 the velocity is equal to the group velocity of the soliton, which consequently stays centered at $t=0$ s. In Fig. 4.4 (a) the velocity is slightly different from the group velocity of the pulse, which makes the center of the pulse shift to $t<0$ s. Apart from this shift of the center, due to the velocity offset, the behavior of the pulses in Fig. 4.3 and Fig. 4.4 (a) is equivalent and well described as the evolution of a higher (third) order soliton, also in the latter case.

Looking at the time evolution on the logarithmic scale Fig. 4.4 (b) reveals that a new component has been formed as the soliton contracted after 4 cm. The component can be identified as the yellow line moving in the positive time direction because it has a lower group velocity than the soliton. If a "pure" third order soliton is considered on a logarithmic scale no such component is formed, hence it must be attributed to the higher order dispersion.

Fig. 4.4 (c) depicts the pulse evolution in the frequency domain. As the soliton contracts in the time domain it broadens in the frequency domain. The horizontal line at $\lambda=550$ nm appears at the same point as the component in Fig. 4.4 (b). The time wavelength plots in Fig. 4.8 described later will reveal that the two are indeed the same. From now on the component is named nonsoliton radiation.

4.3.4 Non-soliton radiation

One of several possible nonlinear phase-matched processes in the PCFs is the generation of non-soliton radiation (NSR). The NSR is emitted as a disper-

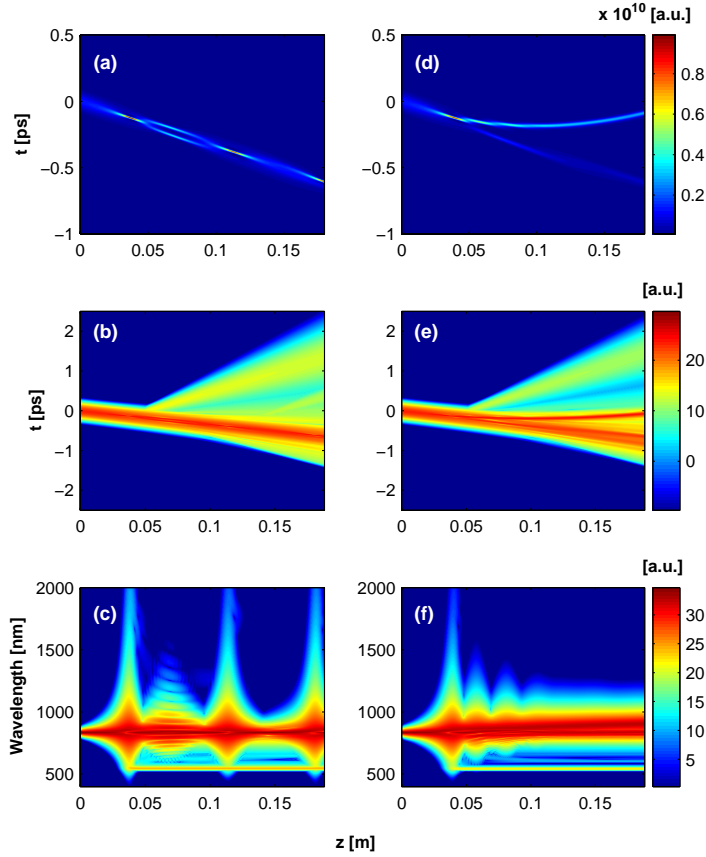


Figure 4.4: Evolution of pulse along the fiber length. (a) Simulation with only Kerr nonlinearity based on Eq. (3.34) of the pulse intensity $|A(z, t)|^2$. The behavior of the pulse resembles the behavior of the third order soliton in Fig. 4.3. (b) The same simulation as shown in (a) but on a logarithmic scale $\log(|A(z, t)|^2)$. A dispersive wave is emitted at $z=4$ cm, where the soliton contracts. (c) The spectral density $\log(|A(z, \lambda)|^2)$ for the simulation shown in (a-b). A new frequency component appears at $\lambda=550$ nm, this is the dispersive wave seen in (b). (d) Simulation of the pulse intensity $|A(z, t)|^2$ including the effects of Raman scattering and self-steepening based on Eq. (3.32). Due to Raman scattering the soliton breaks up. (e) The same simulation as shown in (d) but on a logarithmic scale, revealing the dispersive wave together with the broken-up soliton. (f) The spectral density $\log(|A(z, \lambda)|^2)$ for the simulation shown in (d-e).

sive wave around a wavelength phase-matched to the wavelength of the soliton when $\Delta\phi = \phi_S - \phi_{NSR} = 0$. ϕ_S is the phase of the soliton and ϕ_{NSR} is the phase

of the nonsoliton radiation and they are given by

$$\phi_S = \left(\beta(\omega_S) + \frac{n_2 I \omega_S}{c} \right) z - \omega_S t, \quad (4.3)$$

$$\phi_{NSR} = \beta(\omega_{NSR}) z - \omega_{NSR} t, \quad (4.4)$$

where z is the propagated distance and β is again the propagation constant. For the phase-matching to occur the phases should be evaluated at the same time $t = z/v_S$, where v_S is the group velocity of the soliton. The third term in Eq. (4.3) accounts for self-phase modulation by the pump pulse with intensity I .

The phase difference $\Delta\phi/z$ is plotted at Fig. 4.5 with $\lambda_S=836\text{nm}$. $\Delta\phi = 0$ at $\lambda = 550\text{nm}$, which is indeed the wavelength at which the nonsoliton radiation was observed. The explanation of the supercontinuum generation in terms of

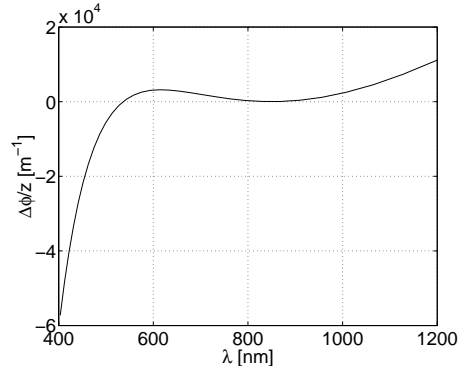


Figure 4.5: Phase difference $\Delta\phi = \phi_S - \phi_{NSR}$ for $\lambda_S = 836\text{nm}$. Phase-matching $\Delta\phi = 0$ is achieved for $\lambda_{NSR} = 550\text{ nm}$.

phase-matched NSR was originally given in [49].

4.3.5 Raman scattering and self-steepening

Figure 4.6 illustrates Raman scattering, which is a non-parametric process where energy is lost due to the vibrational excitation of the material. Raman scattering is the origin of a self-frequency shift increasing with propagation length of solitons to longer wavelengths.

The self-steepening effect given through the time derivative of the nonlinearity in the nonlinear Schrödinger equation is significant for short pulses.

Including Raman scattering and self-steepening in the nonlinear Schrödinger equation (3.32) gives the simulation results shown in the right column of Fig. 4.4. The important influence is that the soliton decays already the first time it contracts (i.e. after 4 cm). As seen on Fig. 4.4 (d-e) the soliton splits up, appearing

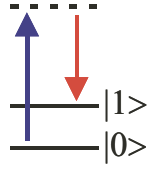


Figure 4.6: The excitation energy between the vibrational states $|1\rangle$ and $|2\rangle$ is lost to the material in the Raman scattering process.

as red traces in (e). The upper trace is a first order soliton self-frequency shifting due to intrapulse Raman scattering, consequently the trace bends. The lower trace is the remaining pulse that starts to diverge into two solitons, the initial third order solitons therefore splits into three first order solitons, with different intensities.

The nonsolitonic radiation is identified in Fig. 4.4 (c) and (f), but in the latter picture an extra NSR component has appeared at $\lambda=600$ nm. As the pulse splits up after 4 cm the intense first order soliton is redshifted and the remaining pulse is blueshifted. Consequently, as the remaining pulse is broadened spectrally it phase-matches to a new wavelength ($\lambda=600$ nm). After the pulse has been split into first order solitons only the redshifting due to Raman scattering alters the picture.

With the given third order dispersion β_3 in Fig. 4.4 it is Raman scattering and self-steepening that make the soliton decay. When the relative size of β_3 compared to β_2 is larger than in the present example, the third order dispersion alone can make the soliton decay [73]. A high relative third order dispersion is found closer to λ_{ZD} .

Most PCFs have a second zero dispersion wavelength λ_{ZD2} between the first zero dispersion wavelength and the far infrared. The second zero dispersion point is characterized by $\beta_3 < 0$. Solitons can be generated in the anomalous dispersion region with a wavelength below λ_{ZD2} . Phase-matched NSR is generated with a wavelength above λ_{ZD2} [74]. The difference between this scenario and the scenario in the present chapter is that the soliton self-frequency shifts and consequently moves towards λ_{ZD2} , but very close the λ_{ZD2} the self-frequency shifting stops because a large part of the soliton light is emitted as NSR and the spectral recoil of the NSR cancels the Raman shift of the soliton as described in [74].

4.3.6 Four wave mixing

As seen in the case of the NSR the dispersion of the fiber is of utmost importance as it governs the phase-matching of nonlinear processes and among those is four wave mixing (FWM). Degenerate FWM is illustrated in Fig. 4.7.

In degenerate four-wave mixing two photons from a pump beam with frequency ω_P are converted into a signal photon with frequency ω_S and an idler

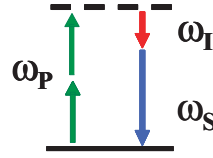


Figure 4.7: Degenerate four wave mixing, ω_P is the pump frequency, ω_S is the signal frequency and ω_I is the idler frequency.

photon with frequency ω_I . Phase-matching is achieved when energy conservation

$$\Delta\omega = \omega_S + \omega_I - 2\omega_P = 0, \quad (4.5)$$

and momentum conservation [41]

$$\Delta\beta = \beta(\omega_S) + \beta(\omega_I) - 2\beta(\omega_P) + \Delta\beta_{NL} = 0. \quad (4.6)$$

are simultaneously fulfilled. The nonlinear contribution to the propagation constant $\Delta\beta_{NL} = 2\gamma P$ originates from self-phase and cross-phase modulation.

The phase-matching condition can be expressed in terms of the even terms in the Taylor expansion of the propagation constant

$$2 \sum_{n=1}^{\infty} \frac{\beta_{2n}}{(2n)!} \Omega^{2n} + 2\gamma P = 0, \quad (4.7)$$

where Ω is the frequency difference between the pump and the signal/idler frequency. The same expression was given in [66] for the occurrence of modulation instabilities. The degenerate FWM does not play a major role for supercontinuum generation in the fiber treated in this chapter, but in the next chapter a fiber where FWM is important will be treated with focus on the fulfillment of this phase-matching condition.

If the intensities are sufficiently high FWM occur between the solitons and the NSR contributing to the generation of new frequency components in the spectrum, eventually filling an entire octave spanning spectrum. For the simulations in the present chapter the powers have been chosen so low that the process is not significant. The phase-matching conditions for this process were recently investigated [28].

4.3.7 Higher harmonics

Third harmonic generation has been demonstrated in the index guiding PCFs, where coupling between different modes and polarization states was exploited to achieve phase-matching [75, 76]. The process is not dominating in the fiber treated in this and the next chapter.

4.4 Supercontinuum evolution as a function of time and wavelength

The dynamics revealed in the previous section is confirmed by the time-wavelength distribution $S(z, t, \lambda)$ of the pulses calculated in the following manner

$$S(z, t, \omega) = \int_{-\infty}^{\infty} dt' e^{-i\omega t'} e^{-(t'-t)^2/\alpha^2} A(z, t'), \quad (4.8)$$

with $\alpha = 100$ fs and plotted as a function of wavelength $\lambda = 2\pi c/\omega$. A Wigner or Husimi distribution [77] could also have been chosen. Similar time-wavelength distributions such as the X-FROG have been used to describe the evolution of supercontinua [46, 78].

Figure 4.8 represents the same simulation as in the left column of Fig. 4.4 without Raman effects and self-steepening. The figure shows the $\log(S(z, t, \lambda))$ distribution of the pulse after (a) 0.0, (b) 3.8, (c) 7.5, (d) 11.3, (e) 15.0 and (f) 18.8 cm, where again 18.8 cm is a soliton period. After 3.8 cm (picture (b)) the self-phase modulation has broadened the spectrum to the wavelength 550 nm which is phase-matched to the wavelength of the initial pulse. The nonsolitonic radiation created moves with a different group velocity and starts to disperse as seen on picture (c). After 11.3 cm the spectrum is again maximally broadened and more NSR is emitted at 550 nm. Picture (e) shows the dispersing NSR components and in picture (f) a third NSR component has been generated.

Figure 4.9 represents the same simulation as in the right column of Fig. 4.4 including Raman scattering and self-steepening. Figure 4.9 (b) is very similar to Fig. 4.8 (b) and nonsolitonic radiation is created at 550 nm. At picture (c) the pulse is decaying into solitons and a NSR component at $\lambda=600$ nm can dimly be seen. Picture (e) and (f) make it clear that the initial pulse is broken up into separate solitons and that the two NSR components at 550 and 600nm are dispersing and moving away with their respective group velocities.

To summarize - in the anomalous dispersion regime the input pulse can be thought of as a higher order soliton. Because of Raman scattering and self-steepening the soliton breaks up into first order solitons. If the spectrum broadens to the phase-matched wavelength in the process non-solitonic radiation is emitted. Subsequently Raman scattering broadens the spectrum to higher wavelengths. (If the intensity is high enough components generated by four wave mixing can fill in the spectrum between the NSR and the solitons).

The soliton decay described above is consistent with the model given by Husakou and Herrmann [49] and with standard theory of solitons [41, 79].

4.4.1 Computational methods

All simulations presented in the paper [III] were based on the computational method A in Sec. 3.6. The simulations have been compared with simulations based on method B and showed very little difference as seen on Fig. 4.10.

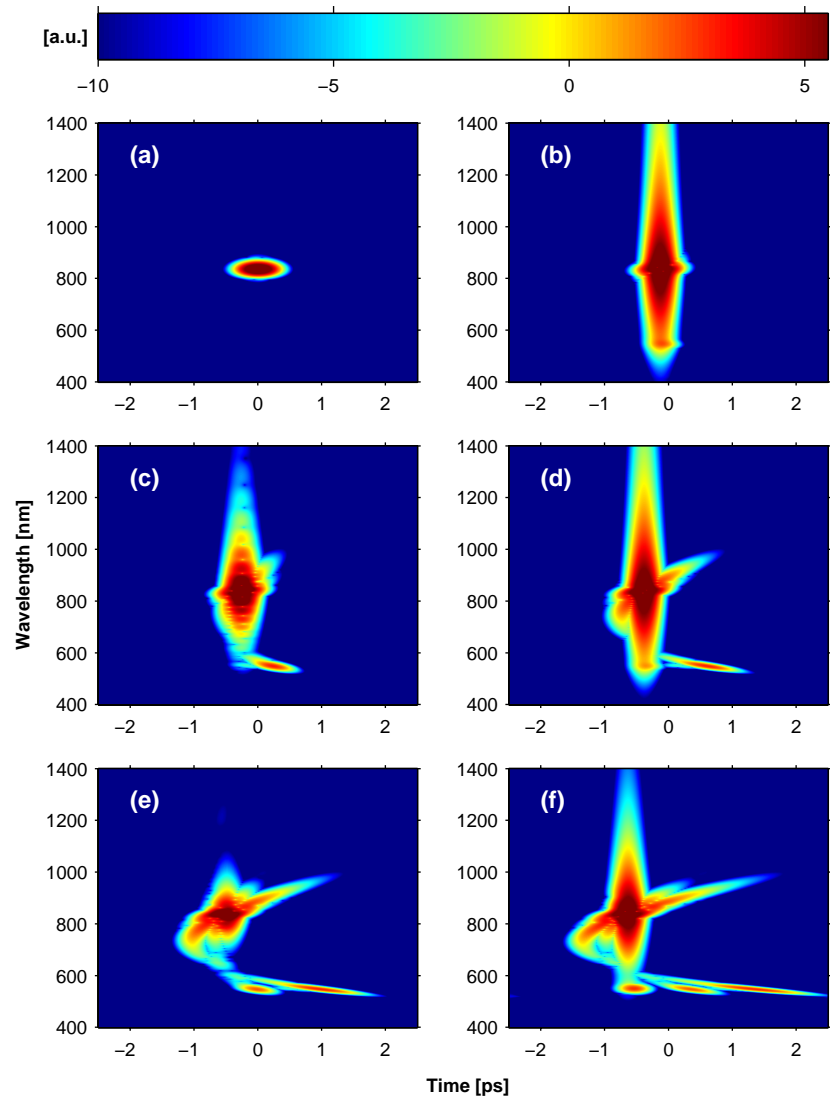


Figure 4.8: The $\log(S(z, t, \lambda))$ distribution after (a) 0.0, (b) 3.8, (c) 7.5, (d) 11.3, (e) 15.0 and (f) 18.8 cm, where 18.8 cm is a soliton period. Simulation with only Kerr nonlinearity.

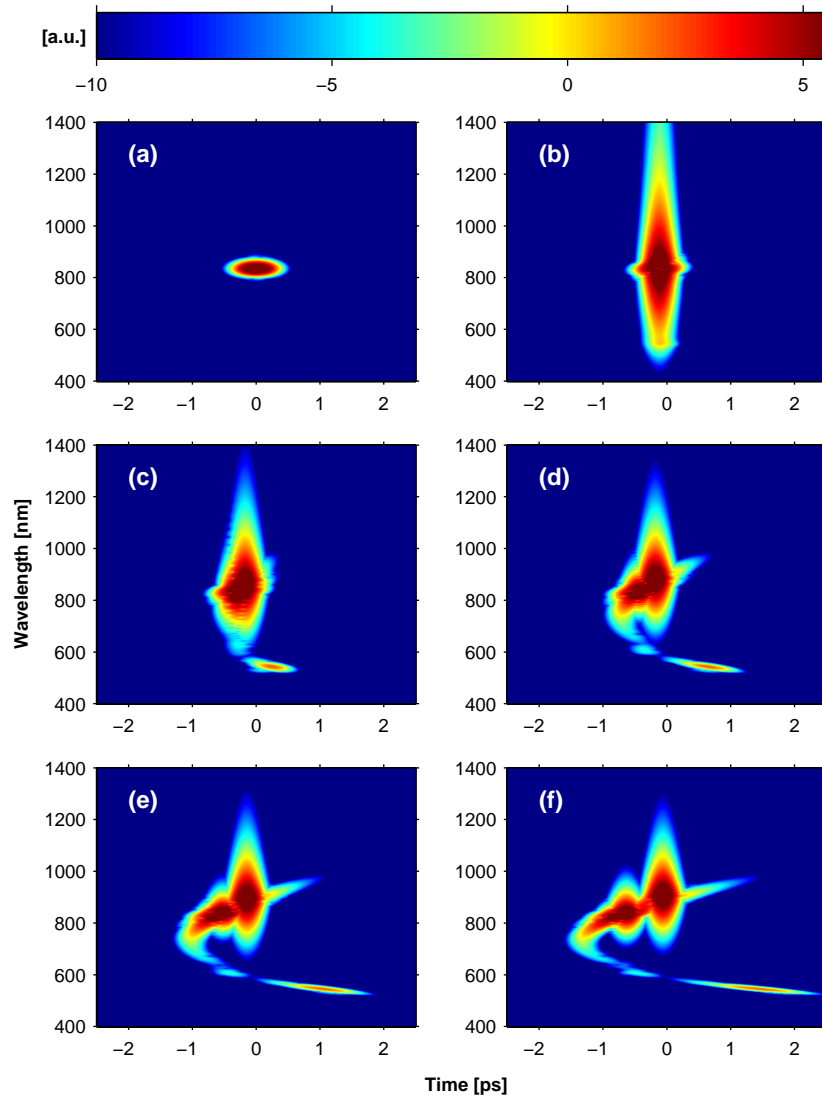


Figure 4.9: The $\log(S(z, t, \lambda))$ distribution after (a) 0.0, (b) 3.8, (c) 7.5, (d) 11.3, (e) 15.0 and (f) 18.8 cm, where 18.8 cm is a soliton period. Raman effects and self-steepening are included in the simulations.

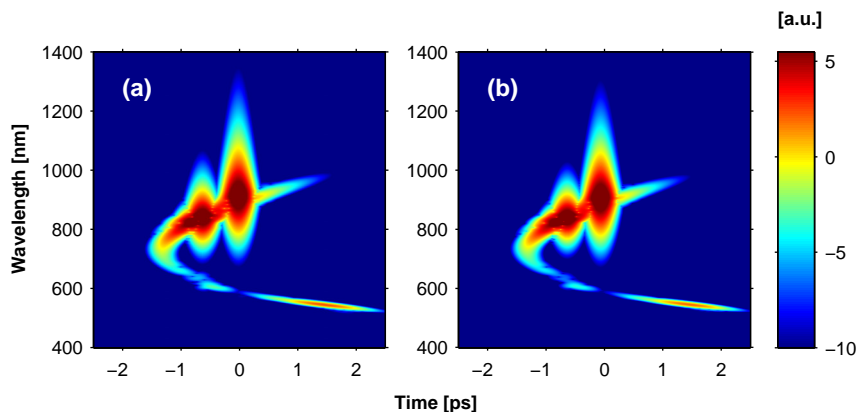


Figure 4.10: (a) This time-wavelength distribution is computed with method A described in Sec. 3.6. (b) The time-wavelength distribution computed with method B. There is only very little difference between the simulations.

4.5 Comparison with experiments

Experimental and numerical results on the onset of supercontinuum generation in a PCF pumped with femtosecond pulses are compared in this section. A range of pump wavelengths in the anomalous dispersion regime are used and intensities are low enough to make the nonsolitonic radiation clearly distinguishable from the rest of the spectrum.

The simulations are here based on Eq. (3.32) using the full dispersion profile of the $1.7 \mu\text{m}$ core diameter fiber as shown on Fig. 2.3 (a) and including the Raman scattering and self-steepening. The input pulses were again $T_{\text{FWHM}} = 100$ fs Gaussian pulses. A constant effective area $A_{\text{eff}} = 2 \mu\text{m}^2$ and nonlinear refractive index $n_2 = 3 \times 10^{-20} \text{m}^2/\text{W}$ were used.

The experimental data presented in this section were obtained by J.J. Larsen and H.N. Paulsen from the Femto Chemistry Laboratory. The pulses were ~ 100 femtoseconds long (intensity FWHM) and they were launched into a 75cm long section of the $1.7 \mu\text{m}$ core PCF. The dispersion of the fiber was found from a time of flight measurement in a ~ 100 m piece of fiber. The measurement gave a zero dispersion wavelength of 660 ± 15 nm. The experimental results consist of output spectra recorded as functions of pump wavelength (λ_P) and power.

There is quite a big difference between the measured zero dispersion wavelength and the calculated of $\lambda = 721 \text{nm}$ from Chap.2. The difference is probably due to imperfections along the length of the fiber, because the fiber zero dispersion is sensitive to the accuracy of the fiber structure. In retrospect it would therefore have been preferable to base the simulations on an experimentally measured full dispersion profile for the used piece of fiber.

4.5.1 Comparison of spectra

Figure 4.11 (a), (b) and (c) show three experimental spectra at pump powers of the order of pJ. In Fig. 4.11 (a) the input wavelength is 710nm, ~ 50 nm above the zero dispersion wavelength. Along with the slightly broadened pump pulse the spectrum shows two additional features. First, at the long wavelength side of the pump pulse, part of the energy is transferred to a distinct peak with a central wavelength of 735 nm. This peak is interpreted as a soliton. The second feature in the spectrum is the nonsolitonic radiation at 622 nm. In the next frame, Fig. 4.11 (b), λ_P is increased to 883 nm. Again, the pump pulse is slightly broadened and part of the pulse has been transferred into a soliton. Turning the attention to the blue side of the spectrum the blueshifted peak is now observed with a central wavelength of 443 nm. Finally, in Fig. 4.11 (c) a spectrum with $\lambda_P=941$ nm is shown. A broadening of the pump pulse is observed together with a shoulder reminiscent of soliton formation. Here the nonsolitonic radiation is observed at a wavelength of 396 nm.

Simulated spectra are shown on Fig. 4.11 (d), (e) and (f). The input pulses were centered at 780 nm (d), 836 nm (e) and 934 nm (f) and propagated a distance corresponding to one soliton period z_0 .

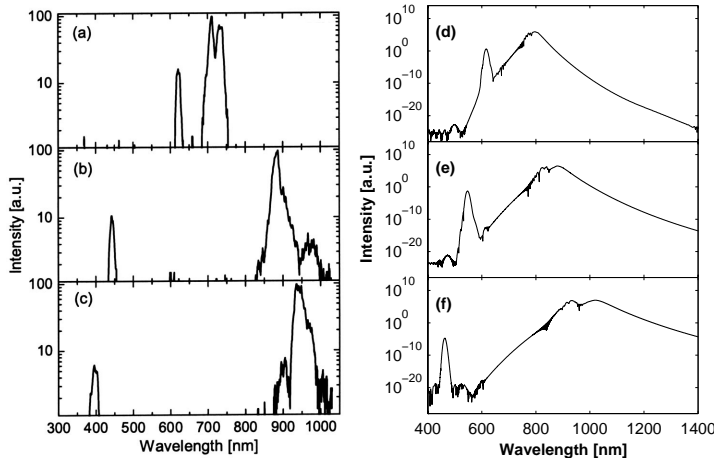


Figure 4.11: Left: recorded spectra for three pump wavelengths (a) $\lambda_p=710$ nm, (b) $\lambda_p=883$ nm and (c) $\lambda_p=941$ nm. Below 560nm the spectra are scaled for clarity. Right: examples of simulated spectra for the following pump wavelengths: (d) 780nm, (e) 836nm and (f) 934nm. The pump peak intensities are (d) 9×10^9 W/cm², (e) 2.9×10^{10} W/cm² and (f) 8×10^{10} W/cm². The peak intensities correspond to soliton numbers of 2.25 (d), 2.80 (e) and 3.22 (f). The soliton period, z_0 , is 36.7 cm (d), 18.8 cm (e) and 10.1 cm (f).

Focusing the attention on Fig. 4.11 (d) where the pumping wavelength of 780 nm is 59 nm above the theoretical zero dispersion wavelength, a nonsolitonic feature at 616 nm and a double peaked structure around the pump wavelength have emerged in the spectrum. The double peaked structure consists of two fundamental solitons undergoing self-frequency shifting. The most intense soliton is situated at 797 nm.

In Fig. 4.11(e) λ_P has been increased to 836 nm. Again, two new features are observed in the spectrum. The most intense soliton peak is found at 886 nm and the nonsolitonic radiation appears at a wavelength of 547 nm. Finally, in Fig. 4.11 (f) λ_P is 934nm and similar to the two previous spectra a peak of nonsolitonic radiation is seen, now at 463 nm. Three fundamental solitons are observed, the most intense at 1078 nm.

Comparing the simulated spectra with the experimentally measured in Fig. 4.11 a good qualitative agreement is found. In particular the nonsolitonic radiation is shifted more towards the blue when λ_P is increased in resemblance with the experiments and in agreement with the phase-matching presented in Sec. 4.3.4.

4.5.2 Phase-matched NSR

To confirm that phase-matching is the determining factor in the formation of the nonsolitonic radiation a series of simulations were made, where the wavelength of the NSR (λ_{NSR}) was found as a function of pump wavelength (λ_P). The calculations were performed at low powers to ensure that the power dependence of the phase-matching was insignificant. The results of these calculations are shown in Fig. 4.12 (a) as crosses. The full line is the expected position of the nonsolitonic radiation as determined from the phase-matching conditions, Eq. (4.3) and 4.4 without the intensity dependent term.

As is evident from the figure there is a near perfect match between the curve and the crosses which again confirms that phase-matching is playing the determining role in the formation of the nonsolitonic radiation.

Experimental data for λ_{NSR} as a function of pump wavelength λ_P are shown on Fig. 4.12 (b) at the lowest power, where the peak could be observed. The phase-matching curve on Fig. 4.12 (a) is highly sensitive to the exact form of the refractive index therefore the experimental data do not exactly reproduce the curve, but the general shape is well reproduced.

4.5.3 Threshold

According to Sec. 4.3 NSR is only formed if the input pulse is spectrally broadened by self-phase modulation to or beyond the wavelength where phase-matching occurs.

A simulation was carried out to confirm this. A 934 nm pulse identical to the one propagated in Fig. 4.11 (f) was propagated for 10.1 cm but with the intensity lowered to 2×10^{10} W/cm², corresponding to a soliton number of 1.6. At

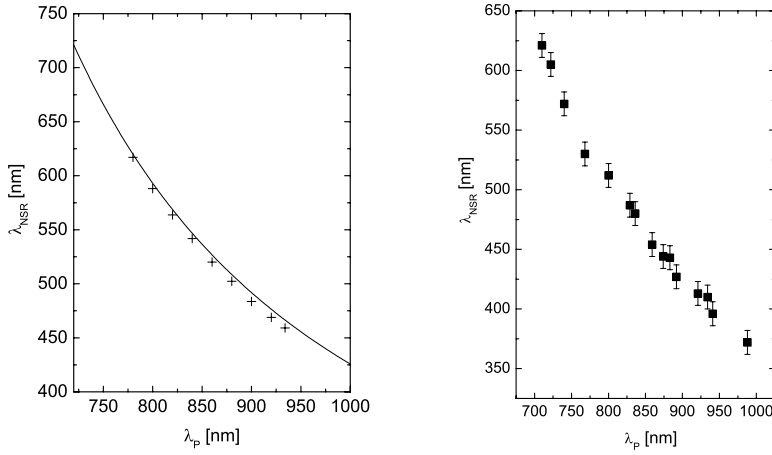


Figure 4.12: Left: phase-matching curve for generation of nonsoliton radiation. The full line is the phase-matching as given by Eq. (4.3) and (4.4). The crosses show the position of the nonsoliton radiation as found from the simulations. Right: measurements of the wavelength (λ_{NSR}) of the blueshifted nonsoliton radiation versus the pump wavelength (λ_P).

this intensity no NSR is formed. The spectral broadening for this input intensity is much less than before and the spectrum only extends down to 580 nm. Consequently it does not reach the phase-matched wavelength.

When λ_P is redshifted away from the zero dispersion wavelength, the phase-matched wavelength is correspondingly blueshifted. To span the gap between λ_P and the phase-matched wavelength an increased amount of self-phase modulation is needed and increasingly higher intensities are hence needed to provide the required spectral broadening. This explains the above observation of an increasing threshold for formation of NSR. This behavior was also found experimentally.

4.5.4 Intensity of the nonsoliton radiation

Fig. 4.13 (a), (b) and (c) show the growth of the nonsoliton radiation for three different pump wavelengths as extracted from the simulations. In all cases, a near exponential increase with intensity is found. The dotted lines in the figure indicate the threshold for formation of N-order solitons.

In Fig. 4.13 (a), where the $\lambda_P=780$ nm is close to the zero dispersion wavelength, the nonsoliton radiation is first observed close to $N=1.6$ but as λ_P is increased away from the zero dispersion wavelength, the nonsoliton radiation appears at increasingly higher soliton numbers consistent with the threshold discussion in 4.5.3.

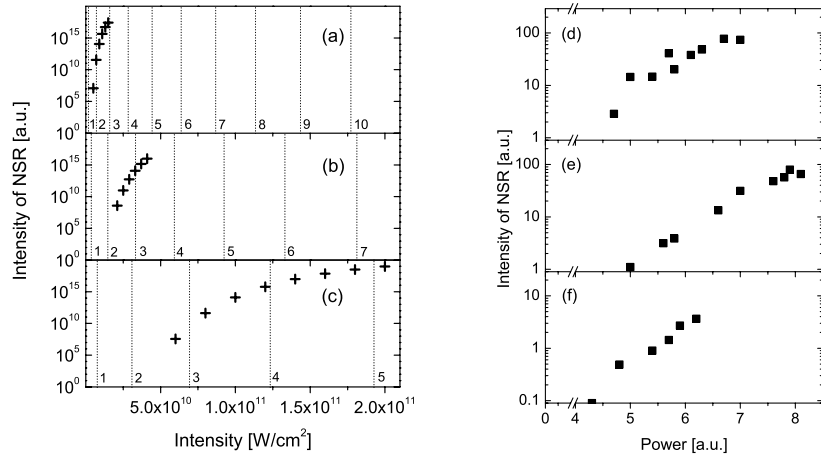


Figure 4.13: Left: the growth of the blue signal as extracted from the simulations. The intensity corresponding to a given soliton number is indicated by the vertical dotted lines. The pump wavelengths are (a) 780 nm, (b) 836 nm and (c) 934 nm. Right: nonsoliton radiation amplitude dependence on input power measured for (d) $\lambda_P=836$ nm, (e) $\lambda_P=883$ nm and (f) $\lambda_P=934$ nm.

Experimentally the growth of the nonsoliton radiation is confirmed in Fig. 4.13 (d), (e) and (f) where the integrated signal in the NSR peak is shown versus the input intensity. Above the threshold an almost exponential growth of the radiation is observed with up to $\sim 5\%$ of the power being nonsoliton radiation at the highest intensities used.

The near exponential growth above threshold is found both in experiments and simulations giving a good qualitative agreement.

4.5.5 Wavelength of the nonsoliton radiation

From the simulations the central wavelength of the nonsoliton radiation is found as a function of pump power and plotted on Fig. 4.14 (a), (b) and (c) for three different input wavelengths. For a given pump wavelength the decrease in λ_{NSR} is 3-9 nm as the intensity increases.

Similar experimental data are shown on Fig. 4.14 (d), (e) and (f). The central wavelength of the nonsoliton radiation decreases as the intensity is increased for three pump wavelengths. The measurements were terminated at the intensity where new spectral features are first observed. The experimentally observed blueshifts are 10-15 nm.

The size of the blueshift of the nonsoliton radiation in the simulations and experiments is comparable and increases in both cases with intensity. Nevertheless the size of the blueshift can not be explained entirely by the intensity

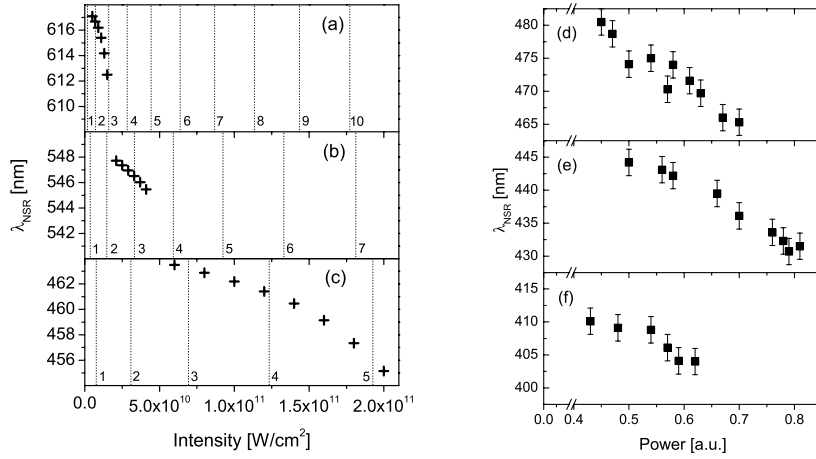


Figure 4.14: Left: the blueshift of the nonsoliton radiation as extracted from the simulations. The intensity corresponding to a given soliton number is indicated by the vertical dotted lines. The pump wavelengths are (a) 780 nm, (b) 836 nm and (c) 934 nm. Right: experimentally measured nonsoliton radiation wavelength dependence on input power (d) $\lambda_P=836$ nm, (e) $\lambda_P=883$ nm and (f) $\lambda_P=934$ nm.

dependent term in the phase-matching condition in Eq. (4.3) (a three-fold increase in intensity only shifts the phase-matched wavelength by ~ 1 nm). Rather it is the change of the pulse itself due to third-order dispersion, self-phase modulation and Raman scattering that changes the matching conditions between the evolving pump pulse and the nonsoliton radiation. It was found that the inclusion of the nonlinear effects in Eq. (3.32) as compared to a Kerr type nonlinearity ($\propto |A|^2 A$) gives a larger blueshift when the intensity is increased. In the process of soliton break-up Raman scattering will redshift the input pulse and consequently the phase-matching condition will be fulfilled for nonsoliton radiation that is more blueshifted.

Furthermore it was found that by increasing the third order dispersion the blueshift is increased to what is experimentally observed. Hence our calculations show that the discrepancy between simulated and experimentally measured blueshift is caused by the differences in the dispersion between the experimental and the simulated fiber.

Returning to Fig. 4.12 (a) the simulation points are seen to lie slightly below the phase-matching curve. The tendency becomes more pronounced with larger distance to the zero dispersion wavelength because higher intensity is needed to broaden the spectrum through self-phase modulation, consequently the NSR is blueshifted in agreement with the intensity dependent blueshift seen on Fig. 4.13.

4.6 Conclusion

The processes initiating supercontinuum formation are governed by formation of (higher-order) solitons. During the evolution of the pump pulse into one or several stable solitons, the surplus light is emitted as a dispersive wave. The simulations show that a large fraction of the dispersive wave is emitted around a distinct wavelength if the input intensity is high enough for self-phase modulation to broaden the spectrum to the phase-matched wavelength. Investigation of the implications of change in pump wavelength and intensity yielded good qualitative agreement between experiments and simulations.

CHAPTER 5

Four wave mixing in a photonic crystal fiber

Supercontinuum generation in a PCF with two zero dispersion wavelengths is investigated. The special dispersion of the fiber has a profound influence on the supercontinuum which is generated through self-phase modulation and phasematched four-wave mixing and not soliton fission as in the type of PCF investigated in Chap. 4. The supercontinuum has high spectral density and is extremely independent of the input pulse over a wide range of input pulse parameters. Simulations show that the supercontinuum can be compressed to ultrashort pulses. This chapter is based on paper [IV].

5.1 Introduction

The anomalous dispersion needed to generate broad spectra through soliton fission [49] makes the supercontinuum generation very susceptible to noise in the input pulse as noise is amplified through modulation instabilities [80]. The interplay between the various nonlinear effects gives rise to temporal and spectral structure, and compression of the spectrally broad fiber output to a few-cycle pulse is thus extremely difficult. Moreover, small changes in the input pulse parameters can lead to very different output spectra, making the selection of an optimum fiber for a given application difficult.

In this chapter it will be argued, based on simulations and experiments, that supercontinuum generation in a highly nonlinear PCF with two closely lying zero dispersion wavelengths solves the problems discussed above. In such a fiber stable, compressible spectra with high spectral density can be generated and the spectra are only weakly dependent on the input pulse parameters.

5.2 PCF with two zero dispersion wavelengths

A scanning electron micrograph image of the PCF with two zero dispersion wavelengths is shown in Fig. 5.1. The pitch of the fiber is $0.98 \mu\text{m}$ and it has a relative holesize of 0.54. The fiber core diameter is $1.5 \mu\text{m}$ with a corresponding effective area of $\sim 1.3 \mu\text{m}^2$ and a high nonlinear coefficient γ of $0.15 \text{ W}^{-1}\text{m}^{-1}$. The numerical aperture of the fiber is 0.49 at 800 nm and the fiber is single mode but not polarization maintaining.

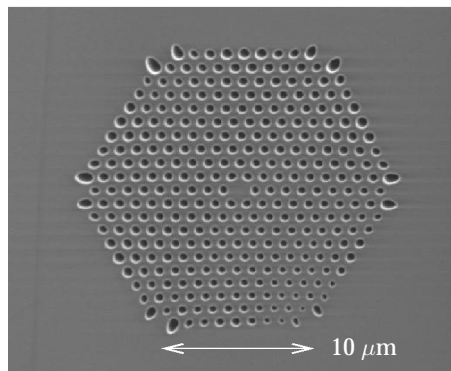


Figure 5.1: A scanning electron micrograph image of the central region of the fiber cross section.

The dispersion of the fiber has been measured using white light interferometry [57]. The result of the dispersion measurement is shown in Fig. 5.2 (a). The dispersion properties of the fiber are highly unusual with two closely lying zero dispersion wavelengths at 780 nm and 945 nm and anomalous dispersion

in the narrow range between the two zero dispersion wavelengths. The dispersion profile should be compared to the dispersion of standard highly nonlinear PCFs which have only one zero dispersion wavelength in the visible/near-infrared range and anomalous dispersion at wavelengths above the zero dispersion wavelength. A number of PCFs exhibit a second but widely separated zero dispersion wavelength at wavelengths typically above 1400 nm.

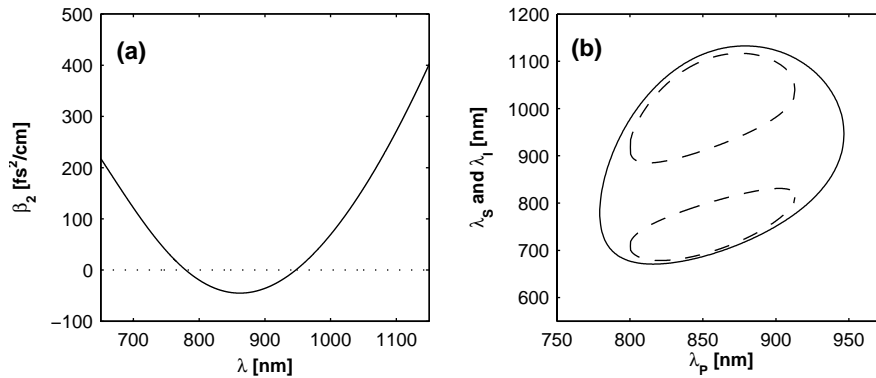


Figure 5.2: (a) Dispersion properties of the PCF with zero dispersion at 780 nm and 945 nm. (b) Phase-matching curves for four-wave mixing in the fiber. Full curve: phase-matching without power-dependent term. Dashed curve: phase-matching with an input power of 300 W.

The condition for degenerate phase-matched FWM in the PCF was presented in Sec. 4.3.6 and as any of the other nonlinear processes in the PCFs the phase-matching is highly depending on the dispersion profile of the fiber. Equation 4.7 was solved based on the measured dispersion $\beta_2(\omega)$ and the phase-matching conditions shown in Fig. 5.2 (b) were found. The result (full line) is that phase-matching can be obtained for all pump wavelengths in the range in-between the two zero dispersion wavelengths. This is in sharp contrast to the results for PCFs with only one zero dispersion wavelength where phase-matching is only possible for pump wavelengths below the zero dispersion wavelength [28, 44]. In fibers with one zero dispersion wavelength, phase-matched four-wave mixing for pump wavelengths above the zero dispersion wavelength can be obtained by inclusion of a nonlinear phaseshift [28, 44] but in the present fiber phase-matching is present at vanishing intensity. When self-phase and cross-phase modulation is included in the calculations the phase-matching curve splits into two sets of phase-matched wavelengths as shown by the dashed curve in Fig. 5.2 (b). The power induced splitting has the benefit of providing phase-matched wavelengths in immediate vicinity of the pump wavelength. For increased intensity the phase-matching curves shrink and for intensities higher than approximately 1 kW phase-matching is no longer possible.

5.3 Experiments

Experimental investigations were carried out by the members of the Femto Chemistry Laboratory. Light from a standard Ti:sapphire femtosecond laser was coupled into a 50 mm long piece of the PCF with a standard 60 \times microscope objective. An input coupling efficiency of up to 50% was obtained. The input intensity to the fiber is adjusted with a $\lambda/2$ plate and a polarizer. The light emanating from the PCF is butt-coupled to a standard fiber connected to an spectrum analyzer where spectra are recorded as the input pulse parameters are varied.

The major experimental findings are shown in Fig. 5.3 (a) and Fig. 5.4 (a) with all spectra plotted on a linear scale. In the first experiment a 40 fs pulse centered at 790 nm is launched into the fiber and the spectral evolution is followed as the input pulse energy is increased. At low pulse energies a fast broadening of the spectrum is observed, but as the pulse energy is increased above ~ 100 pJ the spectral broadening enters a saturation regime where the output spectra are remarkably similar as the pulse energy is increased. Indeed, the supercontinuum is characterized by two peaks with fixed, sharp inner edges at ~ 740 nm and ~ 950 nm and two outer edges which slowly move outward with increasing pulse energy. Above the threshold an almost complete depletion of power in the region between 740 nm and 950 nm is measured and more than 99% of the light emanating from the fiber is contained in the two spectral peaks. In Fig. 5.4 (a)

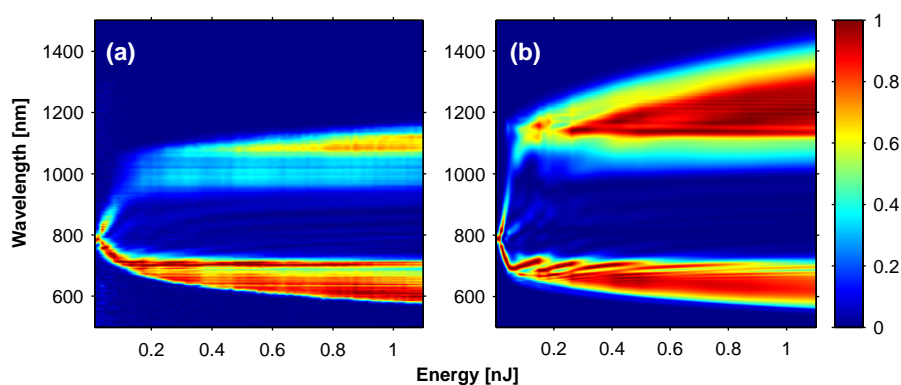


Figure 5.3: (a) Experimental measurement of output spectra versus pulse energy for a 40 fs input pulse centered at 790 nm. (b) Theoretical simulation of the spectral evolution.

the spectral output for 3 different femtosecond pulses are shown and the central wavelength and pulse chirp have been varied, while the pulse energy has been kept constant. Irrespective of the input pulse wavelength and chirp almost identical spectra with depletion of power in the region between ~ 740 nm and ~ 950 nm are obtained. For all pump wavelengths and durations, identical behaviour with increasing pulse energy was observed, i.e. above the threshold the

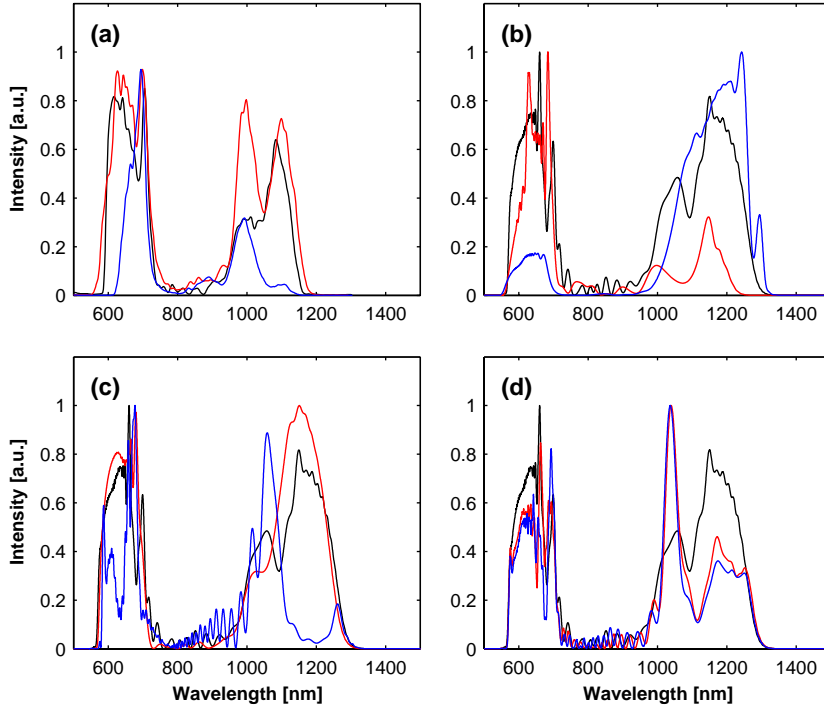


Figure 5.4: (a) Experimentally recorded output spectra 40 fs, $\lambda_0=790$ nm (black), 40 fs, $\lambda_0=810$ nm (red) and a 40 fs, $\lambda_0=790$ nm chirped to ~ 80 fs (blue). The pulse energy is 700 pJ for all pulses. (b) Simulated spectra for $\lambda_0=790$ nm (black), $\lambda_0=700$ nm (red) and $\lambda_0=1000$ nm (blue). For all pulses the energy is 700 pJ and they are 40 fs long. (c) Simulated spectra for 40 fs, 700 pJ (black), 20 fs, 350 pJ (red) and 160 fs, 2800 pJ (blue). For all pulses $\lambda_0=790$ nm. (d) Simulated spectra for an unchirped 40 fs pulse (black), upchirped to 80 fs (red) and downchirped to 80 fs (blue) pulses. For all pulses the energy is 700 pJ, $\lambda_0=790$ nm.

output consists of two peaks with fixed, sharp inner edges and slowly outward moving outer edges.

5.4 Pulse evolution in the fiber

The pulse evolution in the PCF is modelled with Eq. (3.32) and intuitive images of the pulse evolution are obtained by plotting the time-wavelength distributions $S(z, t, \lambda)$ defined in Eq. (4.8) with $\alpha = 100$ fs.

Figure 5.5 (a)-(f) show spectrograms of a 40 fs pulse centered at 790 nm as it propagates through the fiber with a pulse energy of 700 pJ. Once launched in the fiber, the pulse spectrum begins to broaden due to self-phase modula-

tion. After a few mm of propagation the spectrum breaks into two major peaks. Upon further propagation the two major peaks move outward from the original pump wavelength while a steadily increasing number of sub-peaks develop in-between the two major peaks. After approximately 2 cm of propagation the outer edges of the spectrum reach their final values and the number of sub-peaks increases no further. Upon further propagation the intensity is found to redistribute within the spectrum. In particular the region between 770 nm and 980 nm is depleted in excellent agreement with the experimental observation. During the propagation the major peaks are influenced by the dispersion of the fiber as seen from the bending of the major peaks in the spectrogram. The simulated spectra extend further into the infrared region than the experimental spectra. This discrepancy is explained by leakage losses of the present fiber at wavelengths above 1100 nm.

These supercontinuum results are in marked contrast to what was observed in the previous chapter for standard PCFs with only one zero dispersion wavelength or two widely separated zero dispersion wavelengths. The fission of solitons for the standard fibers is known to create excess noise in the supercontinuum due to modulation instability gain which amplifies noise in the input pulse [80].

In the present fiber, self-phase modulation broadens the spectrum and hereby provides seed wavelengths for degenerate and non-degenerate four-wave mixing. Initially the intensity is too high to provide phasematching but as soon the intensity is low enough four-wave mixing proceeds effectively. Because the four-wave mixing process can be phasematched for low intensities, it becomes the dominant mechanism whereas soliton dynamics is arrested and plays only a minor role in the formation of the supercontinuum.

In the absence of soliton fission the supercontinuum is expected to contain less noise than supercontinua from conventional PCFs. Experimentally the amplitude noise across the optical spectrum has been measured. Using a grating and a slit the supercontinuum was spectrally divided into 2 nm slots and then detected by a fast Si photo diode. The resulting photo diode voltage was Fourier-analysed by a frequency analyser in the range 0-80 MHz. For each 2 nm slot the signal power at 76 MHz was compared to the maximum noise feature in the spectrum. The spectra were however seen to be flat and without noise over the entire frequency range. In conclusion only an upper limit of the noise could be established. The optical spectrum in the range 600 nm to 700 nm was analysed in this manner and the noise level was found to be at least 60 dB below the signal power at all wavelengths. Consequently the supercontinuum from this fiber contains less noise than previously reported supercontinua in which significant white noise was present [36]. It should be noted that in the present experiment and in the experiments reported in [36] it was not possible to measure the noise on the laser, only an upper limit was established.

Both experimentally and theoretically the spectral depletion extends outside the region for phasematched degenerate four-wave mixing given by the two zero dispersion wavelengths Fig. 5.2. The additional depletion is caused by

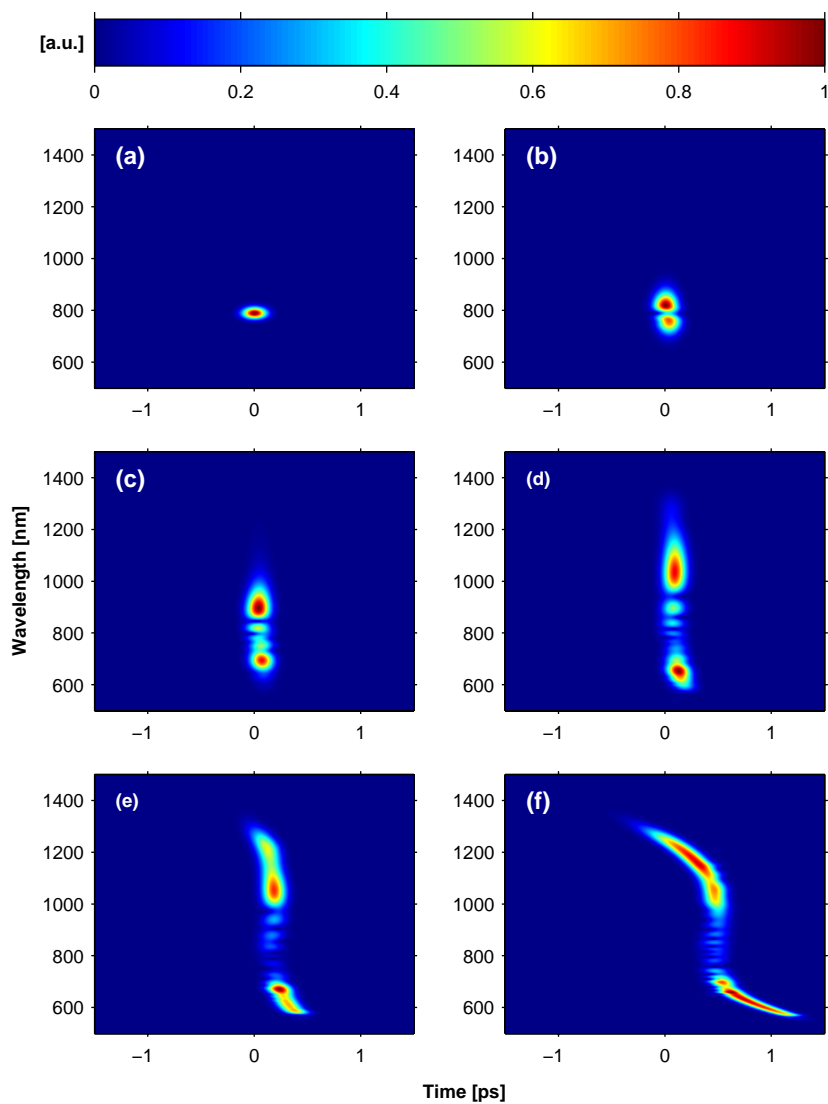


Figure 5.5: (a)-(f) Calculated spectrograms after propagation of (a) 0 cm, (b) 0.2 cm, (c) 0.5 cm, (d) 1 cm, (e) 2 cm and (f) 5 cm in the fiber for a 40 fs input pulse at 790 nm with a pulse energy of 700 pJ.

non-degenerate four-wave mixing being phasematched for a broader range of wavelengths. The reversed non-degenerate four-wave mixing process moving energy back into the depleted region is suppressed, due to group velocity walk-off.

This understanding of the supercontinuum generation process in the fiber is confirmed by simulations where the dispersion of the fiber has been shifted $\beta_2(\omega) \rightarrow \beta_2(\omega) + \beta'$, so the fiber has normal dispersion for all wavelengths. The shift of $\beta_2(\omega)$ removes the possibility of phasematched degenerate four-wave mixing, and with this channel closed only a minor depletion of the intensity between 770 nm and 980 nm is found. It is therefore concluded that phasematched four-wave mixing is the main cause of the intensity depletion between 770 nm and 980 nm. In the simulations with the shifted dispersion, formation of sub-peaks in the 770 nm to 980 nm region is still observed, but the substructure is removed if $\beta_2(\omega)$ is shifted even further into the normal dispersion regime. The shifting reduces the influence of higher-order dispersion and it is concluded that the interplay between self-phase modulation and higher-order dispersion is the cause of the sub-structure.

Simulations using a standard nonlinear Schrödinger equation (3.34) were also performed, where higher-order nonlinear effects, i.e., Raman scattering and self-steepening were omitted in Eq. (3.32) and minor differences in the output was found. This result originates in the threshold pump power for Raman scattering being higher than the threshold for four-wave mixing if phasematching is achieved [41]. The fact that four-wave mixing supersedes Raman scattering results in a higher output power of the field as no energy is lost to phonons in the fiber. Spectral and temporal effects originating in self-steepening are effectively superseded by phasematched four-wave mixing. From the simulations it is concluded that the influence of higher-order nonlinear effects are suppressed due to the phasematching of four-wave mixing.

Figure 5.3 (b) shows a simulation of the power dependence of the spectral evolution using the nonlinear Schrödinger equation (3.34) with input pulse parameters identical to what is used in Fig. 5.3 (a) that is a 40 fs pulse centered at 790 nm. The experiment and simulation are in almost complete agreement and the overall shape is extremely well reproduced. Leakage losses at wavelengths above 1100 nm again cause the simulated spectra to extend further into the infrared region than the experimental spectra. The mean photon number is conserved after 5.0 cm of propagation within the numerical accuracy of the simulations presented in this chapter. The simulated threshold for depletion of the 770 nm to 980 nm region is at ~ 50 pJ pulseenergy which is lower than the experimentally observed value of ~ 100 pJ. This discrepancy is attributed to the lack of polarization maintenance in the fiber. The differences in the substructure between experiments and simulations can also be ascribed to the lack of polarization maintenance not accounted for in the simulation, in combination with the lower resolution in power in the experiment. Polarization maintaining fibers with similar dispersion have been produced after this work was done.

In Fig. 5.4 (b)-(d) the fiber output for a variety of pulses is shown. The sim-

ulations allow the usage of a greater span of pulses than experimentally available. In Fig. 5.4 (b) the central wavelength of the 40 fs input pulse is varied from 700 nm to 1000 nm. The generated spectra consist of two major peaks located outside the depleted region, which extends from 770 nm to 980 nm regardless of the pump wavelength. Using a blueshifted pump wavelength the energy content of the blue peak is enhanced and vice versa. The double peaked spectrum is obtained with pump wavelengths spanning from below 600 nm to above 1200 nm. Figure 5.4 (c) shows the outcome when the pulse duration is changed from 20 fs to 160 fs while keeping the peak intensity fixed. Again, very similar spectra consisting of two peaks with a fixed, strongly depleted region in between the peaks are observed. For pulse durations above ~ 500 fs the formation of the double peaked spectrum stops. This change is due to insufficient self-phase modulation for long pulse durations i.e. the spectrum does not broaden enough to provide seed wavelengths for the four-wave mixing. Finally, Fig. 5.4 (d) shows simulations where the 40 fs input pulse has been up- or down-chirped to a pulse duration of 80 fs. As is evident from the figure the supercontinuum is only weakly dependent on the chirp of the input pulses.

In a fiber with a single zero dispersion wavelength phase-matched four-wave mixing can assist in generating a depleted region in the output spectrum. In that case the different phasematching condition is responsible for a depletion around the zero dispersion wavelength, and the fiber has to be pumped near the zero dispersion wavelength for the conversion to work [81, 82]. In contrast the present fiber can be pumped anywhere in between the two zero dispersion wavelengths with high conversion efficiency and it is the region between the zero dispersion wavelengths that is depleted.

Figure 5.6 shows a plot of the spectral intensity and phase after 5 cm of propagation. The amplitude and phase of the output are smooth as expected from the spectrograms. Due to the smooth phase of the single pulse spectrum, the experimentally realized bandwidth of more than 75 THz in the visible peak centered at 640 nm is therefore compressible to a sub-10 fs pulse. Due to the leakage loss the experimentally realized bandwidth is only ~ 30 THz in the near-infrared peak, which can sustain a 15 fs pulse. Pulse compression has been demonstrated in PCFs with a single zero dispersion wavelength [83], but the compressibility was limited by the soliton fission and resulting breakup of the spectrum.

A theory, not relying on the slowly varying envelope approximation, of four wave mixing in PCFs in the continuous wave regime was presented in [84]. The possibility for phase-matched FWM was predicted for PCFs with two distant zero dispersion wavelengths. This FWM was not experimentally observed when the fibers were pumped with femtosecond pulses, since the zero dispersion wavelengths were too distant to make SPM broaden the spectrum enough to seed the FWM.

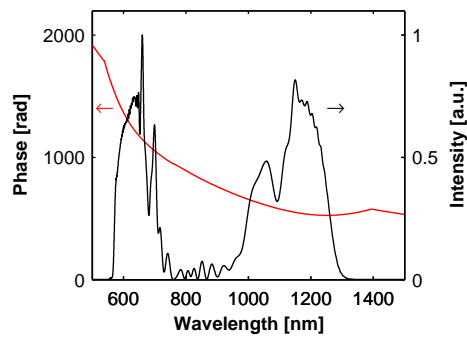


Figure 5.6: Spectrum (black) and phase (red) of the pulse after 5 cm for the 40 fs input pulse at 790 nm with a pulse energy of 700 pJ (also pictured in Fig. 5.5 (f)). The phase of the pulse is well behaved and the visible peak in the spectrum can sustain a sub-10 fs pulse with $\lambda_0=640$ nm.

5.4.1 Computational methods

All simulations presented in this chapter are computed with method B presented in Sec. 3.6, whereas method A was used for the simulations in the associated article [IV]. Spectra calculated with method A and B are compared in Fig. 5.7. Unfortunately, there is an observable difference for the short pulses used in this chapter, mainly due to the implementation of the self-steepening term in method A, where only two points are used to calculate the time derivative. Consequently, method B is the most exact.

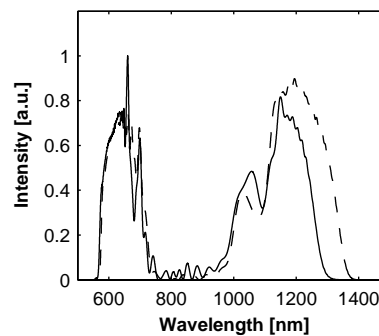


Figure 5.7: Full line: This spectrum is computed with method B described in Sec. 3.6 and is identical to the spectrum shown in Fig. 5.6. Dashed line: The spectrum computed with method A.

5.5 Applications

Computer simulations show that the spectral position of the major peaks can be tuned by tuning of the two zero dispersion wavelengths. Using a set of carefully designed PCFs short pulse generation throughout most of the visible and near-infrared region is therefore possible. Such tunable pulses are applicable in e.g. two color high repetition rate time-resolved pump-probe spectroscopy.

The possibility to generate a stable, compressible supercontinuum with high spectral density leads to a number of improvements in the applications of supercontinua. An advantage in frequency metrology is that the spectral density at ω and 2ω can be optimized by using a fiber with two properly chosen zero dispersion wavelengths. Moreover, the smaller noise present in a supercontinuum generated through phasematched four-wave mixing can increase the signal to noise ratio in experiments, e.g., in fiber based CARS microscopy [II]. Similarly the supercontinuum provides easy access to new wavelength regions for two- and three-photon microscopy [85]. In addition, the dominating FWM could be useful for the production of frequency-converters for optical networks.

5.6 Phase-matched FWM - continuous wave regime

In the Femto Chemistry Laboratory it was found that phase-matched four wave mixing is significant as well in the CW regime for a similar fiber with dispersion profile $\beta_2(\omega)$ shown in Fig. 5.8 (a). The condition for phase-matching of degenerate FWM is again given by Eq. (4.7) and the solution to the equation is shown in Fig. 5.8 (b) for powers of 0 W and 1000 W. In the CW regime the influence of the power on the phase-matching condition is very limited. There is a significant extra bend in the 0 W phase-matching curve on Fig. 5.8 (b) as compared to Fig. 5.2 (b) due to opposite signs between the determining higher order even dispersive terms [V].

The experimental demonstration of the FWM in the fiber is shown in Fig. 5.9. Part (a) of the figure shows experimental data for the FWM on the major axis and part (b) shows experimental data on the minor axis. The discrepancy between the measurements and the calculated phase-matching curve originates in the measurement of the dispersion, which was not done for the polarization directions separately. Due to the bend on the phase-matching curve it is possible to generate signal light in the whole wavelength range between 500 and 650 nm, giving perspectives for a source of green or blue light.

5.7 Conclusion

In summary, a new way of generating a stable and intense supercontinuum through self-phase modulation and phasematched four-wave mixing in a newly designed PCF with two closely lying zero dispersion wavelengths has been

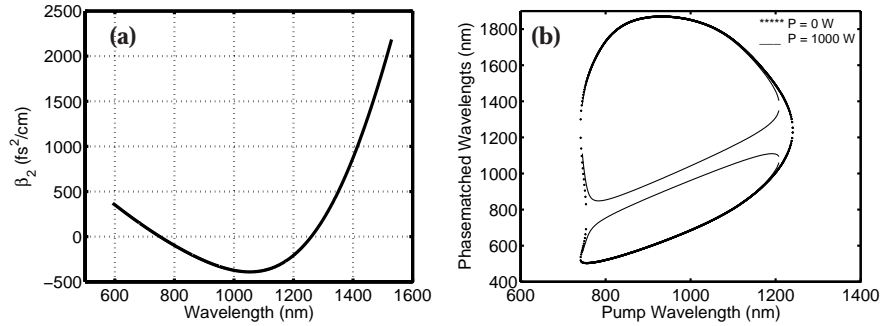


Figure 5.8: (a) β_2 for the used PCF with two zero dispersion wavelengths. (b) Condition for degenerate phase-matched FWM in the fiber with pump powers of 0W and 1000W. The figures are from the article [V] made by Thomas Vestergaard Andersen.

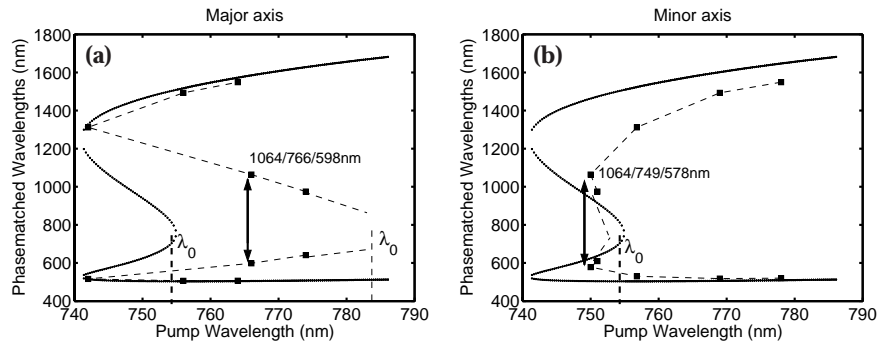


Figure 5.9: (a) Experimental data for the FWM on the major axis. (b) Experimental data for the FWM on the minor axis. The figures are from the article [V] made by Thomas Vestergaard Andersen.

demonstrated. Standard supercontinuum generation in PCFs relies on anomalous dispersion and the supercontinuum generated through soliton fission becomes very susceptible to the characteristics of the input pulse as noise is amplified through modulation instabilities. However, in the present PCF both the soliton fission mechanism and the noise amplification through modulation instabilities are suppressed. Consequently, both the amplitude and the phase of the supercontinuum are well-behaved, and extremely unsusceptible to the character of the input pulse. By optimizing the dispersion profile of the double zero dispersion wavelength fibers the generated stable supercontinuum can be tailored for the many applications envisaged, in particular compression to ultrashort pulses, metrology, pump-probe spectroscopy and non-linear microscopy.

CHAPTER 6

Introduction to Bose-Einstein condensates in optical lattices

In this chapter, an introduction to the field of BEC physics will be given with emphasis on condensates in periodic potentials. A derivation of the Gross-Pitaevskii equation will be sketched, the equivalent equation in nonlinear atom optics to the nonlinear Schrödinger equation in nonlinear optics. More thorough introductions to BEC physics are given in the books by Pethick and Smith [86], Pitaevskii and Stringari [87] and the review articles [88–90]. Recently excellent reviews on BEC physics in optical lattices have been written [91, 92].

6.1 Introduction

In the process of Bose-Einstein condensation where a single quantum state is macroscopically occupied, the boson nature of the particles is clearly revealed. Since the initial realizations of Bose-Einstein condensation in 1995 [1, 2, 93] a huge research effort has been put into the field, both regarding theory and experiments. The 2001 Nobel prize in Physics was awarded to Cornell, Wieman [94] and Ketterle [95] for their achievements of BEC. A typical realization of a BEC relies on laser cooling of the atomic gas in a magneto-optical trap and subsequent evaporative cooling in a conservative trap. A review of experimental techniques is given in [96]. The laser cooling of atoms, being a major step on the road to BEC, led to the 1997 Nobel prize in physics awarded to Chu, Cohen-Tannoudji and Phillips. After the successful applications of the lasers for the near resonant Doppler and Sisyphus cooling processes the next step was far detuned optical lattices forming conservative periodic potentials seen by the condensates.

Two amazing branches of physics are united in the system of a BEC in an optical lattice and the system is literally tunable. Through a Feshbach resonance the sign and magnitude of the nonlinear interaction can be tuned through the s -wave scattering length of the condensate. Simultaneously the optical lattice can be tuned forming perfectly periodic 1D, 2D or 3D spatial structures changing the periodicity of the BEC. The tunability of the periodicity offers a degree of freedom, unavailable in traditional condensed matter systems of electrons in a crystal lattice, where the periodicity is given by the material.

Photonic crystals and PCFs are revolutionizing technologies exactly because they provide a micro-structuring and thereby a periodicity in one, two or three dimensions. The periodicity can be manipulated and designed after almost any wish. Still, the optical lattice offers a tunability of the periodicity to the BEC during an experiment. The photonic crystal on the other hand has its final shape after it has been manufactured, and consequently it does not offer this tunability during an experiment.

The huge flexibility of the system of the BEC in the optical lattice has a price. It is a complicated experiment to conduct, indeed more complex than most experiments on the fundamental physics in photonic crystals, where most often no vacuum chambers are needed. Still, it is worth the effort. A lot of condensed matter physics can be investigated in BECs in optical lattices. Certainly, the nature of superfluidity can be investigated in the very clean system provided by the BEC, where almost the entire atomic cloud can be condensed into the superfluid phase. Strong correlations in a many body quantum mechanical system are elucidated in the Mott insulator transition, illustrating the Heisenberg uncertainty of the phase and the number of atoms. Recently, the Mott insulator state was demonstrated in Munich [97] bringing much attention to the field. Many quantum statistical phenomena can be investigated. Huge possibilities are related to investigating Fermi gases alone or together with Bose gases in op-

tical lattices [98]. The field of quantum information processing could benefit, for instance by using the Mott insulator state for a natural quantum register, as suggested in Ref. [92].

Finally, a lot of the physics learned in nonlinear optics can be directly transferred to the BEC system with the periodic potential. For example the approaches to investigations of bright solitons in cold atomic gases were greatly influenced by nonlinear optics [99], where a multiple scales analysis carried out in optics could be almost directly translated [100, 101]. Russell and coworkers [102] used their knowledge from fiber optics about the generation of nonsoliton radiation and the breakup of solitons in PCFs to investigate the breakup of gap solitons in BECs in periodic potentials. The FWM process investigated in Chap. 7 is indeed inspired by the phase-matched FWM playing a central role in the light propagation in the PCF.

The fields of nonlinear atom optics and nonlinear optics have a common origin, since the systems investigated in the two fields can basically be described by the Maxwell-Bloch equations. In the case of nonlinear optics the atomic degrees of freedom have been eliminated only preserving a linear and nonlinear susceptibility of the medium leading to an effective equation for the electromagnetic field only, the nonlinear Schrödinger equation derived in Chap. 3. In nonlinear atom optics an opposite procedure can be used. By eliminating the light field from the Maxwell-Bloch equations a nonlinear master equation for the atoms can be derived [103]. If dissipation is insignificant the master equation can be reduced to a nonlinear Schrödinger equation, but this time for the atomic field (the Gross-Pitaevskii equation) [103]. In the present chapter the Gross-Pitaevskii equation will be derived using the standard approach, by constructing an equation for N identical particles and subsequently making a mean-field approximation.

6.2 Fundamentals of BEC physics

To describe the physics of a BEC, a system of N identical, interacting bosons moving in three dimensional space and potentially subjected to external forces will be considered. The bosons can be described by a many-body wave function $\Phi(\mathbf{r}_1, \mathbf{r}_2, \dots, \mathbf{r}_N, t)$ and the time evolution can be found by solving the many-body Schrödinger equation

$$i\hbar \frac{\partial}{\partial t} \Phi(\mathbf{r}_1, \mathbf{r}_2, \dots, \mathbf{r}_N, t) = \hat{H} \Phi(\mathbf{r}_1, \mathbf{r}_2, \dots, \mathbf{r}_N, t), \quad (6.1)$$

on the premise that the initial state of the system is known. The Hamiltonian \hat{H} contains single particle Hamiltonians given by

$$\hat{h}(\mathbf{r}) = -\frac{\hbar^2}{2m} \nabla^2 + V_{ext}(\mathbf{r}), \quad (6.2)$$

where $V_{ext}(\mathbf{r})$ is the external potential and m is the mass of an atom. Under the assumption of a dilute gas, third and higher order interaction terms can be

neglected and only two-body terms $V(\mathbf{r}_j, \mathbf{r}_k)$ are needed to describe the interactions. The complete microscopic information about forces and interactions working on the bosonic particles is consequently contained in the Hamiltonian

$$\hat{H} = \sum_{j=1}^N \hat{h}(\mathbf{r}_j) + \sum_{j,k=1, j < k}^N V(\mathbf{r}_j, \mathbf{r}_k). \quad (6.3)$$

6.2.1 The two-body interaction potential

For alkali atoms the structure of the actual interaction potential is quite complicated, having a repulsive hard core and many bound states. As mentioned above the bosonic gas is assumed to be dilute. The requirement for a gas with density ρ to be dilute is that the average distance between atoms $\rho^{-1/3}$ is much larger than the range of the potential. Finding more than two particles at the same point in space is very unlikely, when the gas is dilute. Consequently, third and higher order interaction terms can be neglected as mentioned above. The two body interaction only depends on the distance between the particles, not on the actual positions of the particles, i.e. $V(\mathbf{r}, \mathbf{r}') = V(\mathbf{r} - \mathbf{r}')$. Additionally, the details of the scattering potential do not matter, since the particles do not get close enough to probe the details of the potential. If furthermore the temperature is low, the scattering takes place in the s-wave only, the scattering is fully elastic and the scattering potential can be substituted with a zero range pseudo-potential

$$V(\mathbf{r} - \mathbf{r}') = g\delta(\mathbf{r} - \mathbf{r}'), \quad (6.4)$$

where g is the so-called coupling constant,

$$g = \frac{4\pi\hbar^2}{m} a_s. \quad (6.5)$$

The pseudo-potential is consequently fully characterized by the s-wave scattering length a_s of the exact potential and a_s can be experimentally measured. Repulsive atom-atom interactions are characterized by a positive scattering length, which is the case in the proposal presented in Chap. 7. For a negative scattering length the atom-atom interaction is attractive. Above a certain number of atoms the condensate collapses because the kinetic energy is no longer sufficient to keep the atoms apart, as first experimentally demonstrated in ${}^7\text{Li}$ [93]. The sign and magnitude of the scattering length can be tuned by external fields with Feshbach resonances [104, 105], making the scattering length a tunable parameter for the system of the condensate. In atom optics the scattering length plays an equivalent role to the nonlinear susceptibility in nonlinear optics. For a PCF the nonlinear susceptibility is a material specific parameter. Additionally, the micro structuring of the fiber is responsible for the high intensity levels achievable within the fibers and the resulting nonlinear effects. Still, that does not make the nonlinear response of the fiber tunable in the sense that the nonlinearity can be tuned during an experiment with a single fiber, as opposed to the BEC where the Feshbach resonance can be tuned.

6.2.2 Second quantized Hamiltonian

In the second quantization creation and annihilation operators are introduced for the bosons. The bosonic field operator $\hat{\psi}^\dagger(\mathbf{r})$ creates a boson at the position \mathbf{r} and $\hat{\psi}(\mathbf{r})$ annihilates a boson at position \mathbf{r} . In the second quantization the full Hamiltonian in Eq. (6.3) is given by

$$\begin{aligned} \hat{H} = & \int d\mathbf{r} \hat{\psi}^\dagger(\mathbf{r}) \left[-\frac{\hbar^2}{2m} \nabla^2 + V_{ext}(\mathbf{r}) \right] \hat{\psi}(\mathbf{r}) \\ & + \frac{1}{2} \int \int d\mathbf{r} d\mathbf{r}' \hat{\psi}^\dagger(\mathbf{r}) \hat{\psi}^\dagger(\mathbf{r}') V(\mathbf{r}, \mathbf{r}') \hat{\psi}(\mathbf{r}) \hat{\psi}(\mathbf{r}'). \end{aligned} \quad (6.6)$$

The pseudo-potential Eq. (6.4) can be inserted above giving the following expression

$$\begin{aligned} \hat{H} = & \int d\mathbf{r} \hat{\psi}^\dagger(\mathbf{r}) \left[-\frac{\hbar^2}{2m} \nabla^2 + V_{ext}(\mathbf{r}) \right] \hat{\psi}(\mathbf{r}) \\ & + \frac{g}{2} \int d\mathbf{r} \hat{\psi}^\dagger(\mathbf{r}) \hat{\psi}^\dagger(\mathbf{r}) \hat{\psi}(\mathbf{r}) \hat{\psi}(\mathbf{r}). \end{aligned} \quad (6.7)$$

This second quantized Hamiltonian will be the starting point for the derivation of the Gross-Pitaevskii equation.

6.2.3 The Bogoliubov approximation and mean field theory

The many body Hamiltonian (6.7) fully describes the behavior of the particles, but in the case of a dilute Bose gas mean field theories can describe the system very well. It is characterized by a small set of parameters like the condensate wave function and the chemical potential.

In 1947 Bogoliubov [106] described a dilute homogeneous Bose gas with a mean field theory, where the condensate contribution to the bosonic field operator is separated out. The field operator can be written as

$$\hat{\psi}(\mathbf{r}) = \sum_k \psi_k(\mathbf{r}) \hat{a}_k, \quad (6.8)$$

where $\psi_k(\mathbf{r})$ is a single particle wave function and $\hat{a}_k^\dagger, \hat{a}_k$ are the corresponding bosonic creation, annihilation operators defined in Fock space:

$$\hat{a}_k^\dagger |n_0, n_1, \dots, n_k, \dots\rangle = \sqrt{n_k + 1} |n_0, n_1, \dots, n_k + 1, \dots\rangle \quad (6.9)$$

$$\hat{a}_k |n_0, n_1, \dots, n_k, \dots\rangle = \sqrt{n_k} |n_0, n_1, \dots, n_k - 1, \dots\rangle \quad (6.10)$$

and they obey the normal bosonic commutation relations

$$[\hat{a}_k, \hat{a}_q^\dagger] = \delta_{k,q}, \quad [\hat{a}_k, \hat{a}_q] = 0. \quad (6.11)$$

As mentioned, the idea is to separate the bosonic field operator into a condensed part $\psi_0(\mathbf{r})\hat{a}_0$ and a non-condensed part $\delta\hat{\psi}(\mathbf{r})$

$$\hat{\psi}(\mathbf{r}) = \psi_0(\mathbf{r})\hat{a}_0 + \delta\hat{\psi}(\mathbf{r}). \quad (6.12)$$

For Bose-Einstein condensation to occur, the number of atoms in the lowest lying single particle state must be macroscopic i.e. $n_0 \gg 1$ and n_0/N_T must remain finite for $N_T \rightarrow \infty$, where N_T is the total number of atoms. The approach of Bogoliubov [106] is based on the following two approximations:

- The operator $\delta\hat{\psi}(\mathbf{r})$ is treated as a small perturbation, a good approximation if the fraction of non-condensed atoms is small.
- Given that $\hat{a}_0|n_0, \dots\rangle = \sqrt{n_0}|n_0, \dots\rangle$ and $\hat{a}_0^\dagger|n_0, \dots\rangle = \sqrt{n_0+1}|n_0+1, \dots\rangle$, the approximation is to replace the operators \hat{a}_0 and \hat{a}_0^\dagger with c-numbers such that $\hat{a}_0 = \hat{a}_0^\dagger = \sqrt{n_0}$, which is reasonable, when the condensed state is macroscopically occupied.

The resulting expression for the boson field operator in the Bogoliubov approximation is the following

$$\hat{\psi}(\mathbf{r}) = \sqrt{N}\psi(\mathbf{r}) + \delta\hat{\psi}(\mathbf{r}), \quad (6.13)$$

where the number of atoms in the ground state n_0 has been replaced with N and the condensate wave function $\psi_0(\mathbf{r})$ with $\psi(\mathbf{r})$. In the following it will be shown that approximating the bosonic field operator with the condensate wave function leads to the Gross-Pitaevskii equation.

6.2.4 The Gross-Pitaevskii equation

To derive the Gross-Pitaevskii equation, the second quantized Hamiltonian from Eq. (6.7) is inserted into the Heisenberg equation of motion, resulting in the following expression

$$i\hbar \frac{\partial \hat{\psi}(\mathbf{r}, t)}{\partial t} = [\hat{\psi}(\mathbf{r}, t), \hat{H}] \quad (6.14)$$

$$= \left[-\frac{\hbar^2}{2m} \nabla^2 + V_{ext}(\mathbf{r}, t) + g\hat{\psi}^\dagger(\mathbf{r}, t)\hat{\psi}(\mathbf{r}, t) \right] \hat{\psi}(\mathbf{r}, t), \quad (6.15)$$

where the following bosonic commutation relations for the field operator were used to reduce the expression

$$[\hat{\psi}(\mathbf{r}), \hat{\psi}^\dagger(\mathbf{r}')] = \delta(\mathbf{r} - \mathbf{r}'), \quad [\hat{\psi}(\mathbf{r}), \hat{\psi}(\mathbf{r}')] = [\hat{\psi}^\dagger(\mathbf{r}), \hat{\psi}^\dagger(\mathbf{r}')] = 0. \quad (6.16)$$

Now the Bogoliubov approximation is used and the bosonic field operator is substituted with $\hat{\psi}(\mathbf{r}, t) = \sqrt{N}\psi(\mathbf{r}, t)$ whereby excitations are completely neglected. The result is

$$i\hbar \frac{\partial \psi(\mathbf{r}, t)}{\partial t} = \left[-\frac{\hbar^2}{2m} \nabla^2 + V_{ext}(\mathbf{r}, t) + gN|\psi(\mathbf{r}, t)|^2 \right] \psi(\mathbf{r}, t), \quad (6.17)$$

which is the so called **Gross-Pitaevskii equation** for the condensate wave function. If the external potential is time independent and the gas is in thermal equilibrium, solutions to the Gross-Pitaevskii equation which are only time-dependent through a global phase can be found. Writing such a solutions as

$$\psi(\mathbf{r}) \exp(-i\frac{\mu}{\hbar}t), \quad (6.18)$$

the time independent Gross-Pitaevskii equation appears

$$\left[-\frac{\hbar^2}{2m}\nabla^2 + V_{ext}(\mathbf{r}) + gN|\psi(\mathbf{r})|^2 \right] \psi(\mathbf{r}) = \mu\psi(\mathbf{r}). \quad (6.19)$$

In the Gross-Pitaevskii equation the term $gN|\psi(\mathbf{r})|^2$ describes the interactions of an atom in the condensate with the other $N - 1$ ($\sim N$ for big N_T) atoms in the condensate, i.e. the atom sees the mean field of the other atoms, but since they are all in the same quantum state, the other atoms can be described with the same single particle wave function $\psi(\mathbf{r})$, normalized to 1. The density of the condensate is then given by $N|\psi(\mathbf{r})|^2$. The global phase μ in the wave function (6.18) is equal to the chemical potential giving the energy required to add an other particle to the condensate. The Gross-Pitaevskii equation can be derived in a number of other ways. One way, illustrating the role of the chemical potential, is to start from the grand canonical many body Hamiltonian $\hat{K} = \hat{H} - \mu\hat{N}$, where the chemical potential μ works as a Lagrange multiplier and the last term secures the mean number of particles. By inserting $\hat{\psi} = \sqrt{N}\psi$ and making a variation of \hat{K} with respect to ψ^* the Gross-Pitaevskii equation is found.

The Gross-Pitaevskii equation is the equivalent in nonlinear atom optics to the nonlinear Schrödinger equation in nonlinear optics. Additionally, the mean-field treatment in atom optics is equivalent to the classical treatment of the electromagnetic field in optics. To go a step further in the analogy, a quantum optics treatment of the photons with creation an annihilation operators is equivalent to the second quantization in atom optics.

6.2.5 Elementary excitations

Because excitations have been neglected in the derivation, the Gross-Pitaevskii equation is only valid at $T = 0K$, and even there it is approximate since the interactions lead to quantum depletion; consequently some atoms are in excited states even at $T = 0$. But for cold alkali gases (below the critical temperature) it is generally a good approximation to neglect the number of non-condensed atoms N' in comparison with N since the quantum depletion is small.

It can be useful to move beyond the mean field approximation and calculate the elementary excitations of a condensate, both to investigate the dynamical and the thermodynamical stability of the condensate. A linear stability analysis can be performed by assuming the excitations to be small oscillations around a stationary state $\psi(\mathbf{r})$ of the Gross-Pitaevskii equation. One approach is to assume solutions to the time dependent Gross-Pitaevskii equation (6.17) of the

following form

$$\psi(\mathbf{r}, t) = e^{-i\frac{\mu}{\hbar}t} \left[\psi(\mathbf{r}) + U(\mathbf{r})e^{-i\omega t} - V^*(\mathbf{r})e^{i\omega t} \right]. \quad (6.20)$$

After keeping terms linear in $U(\mathbf{r})$ and $V(\mathbf{r})$ in Eq. (6.17) and equating terms proportional to $e^{-i\omega t}$ and $e^{i\omega t}$ the Bogoliubov-de Gennes equations appear

$$\mathcal{L} \begin{pmatrix} U_k \\ V_k \end{pmatrix} = \hbar\omega_k \begin{pmatrix} U_k \\ V_k \end{pmatrix}, \quad (6.21)$$

where the matrix operator \mathcal{L} is given by

$$\mathcal{L} = \begin{pmatrix} (\hat{h}(\mathbf{r}) - \mu + 2gN_0|\psi(\mathbf{r})|^2) & -gN\psi(\mathbf{r})^2 \\ +gN_0\psi^*(\mathbf{r})^2 & -(\hat{h}(\mathbf{r}) - \mu + 2gN|\psi(\mathbf{r})|^2) \end{pmatrix}. \quad (6.22)$$

The Bogoliubov-de Gennes equations can be derived in various other ways, for instance by introducing the Bogoliubov approximation $\hat{\psi}(\mathbf{r}) = \sqrt{N}\psi(\mathbf{r}) + \delta\hat{\psi}(\mathbf{r})$ in the grand canonical many body Hamiltonian and collecting terms of second order in $\delta\hat{\psi}(\mathbf{r})$.

Because the evolution of the modes behaves as $exp(\pm i\omega_k t)$, the criterium for dynamical stability is that all the energies in the Bogoliubov spectrum are real. If the energies of all the modes for which $\langle U_k|U_k \rangle - \langle V_k|V_k \rangle = 1$ in addition are positive the condensate is said to be thermodynamically stable. If on the other hand some of these energies are real and negative the system is said to exhibit a energetic instability / Landau instability [107]. For the class of modes for which $\langle U_k|U_k \rangle - \langle V_k|V_k \rangle = -1$ the criterium for energetic stability is that the energies are real and negative.

6.2.6 One-dimensional nonlinear Schrödinger equation

A quasi one-dimensional situation can be assumed for a BEC in a one-dimensional periodic potential if the condensate is confined in a cylindrically symmetric trap, and the external potential is generally separable. Furthermore, the atom-atom interaction energy should be smaller than the transverse excitation energy, which for a transverse harmonic confinement is given by $E_\perp = \hbar\omega_\perp$. The condensate is assumed to be in the transverse ground state, which for the harmonic confinement is a gaussian. The single particle wave function is written as $\psi = \psi_\perp(x, y)\psi(z)$, leading to the one-dimensional Gross-Pitaevskii equation

$$i\hbar \frac{\partial \psi(z, t)}{\partial t} = \left[-\frac{\hbar^2}{2m} \frac{\partial^2}{\partial z^2} + V_{ext}(z) + \gamma |\psi(z, t)|^2 \right] \psi(z, t). \quad (6.23)$$

The strength of the nonlinearity is described by the factor

$$\gamma = \frac{gN}{A_\perp}, \quad (6.24)$$

where $A_{\perp} = \frac{2\pi\hbar}{m\omega_{\perp}}$ for the gaussian ground state. The criterium of the atom-atom interaction energy being smaller than the transverse excitation energy can be expressed as $2a_s N |\psi(z)|^2 < 1$. This weak interaction limit corresponds to about 100 atoms per μm for ^{87}Rb , the alkali gas used in our proposal in the following chapter.

Salasnich et al. [108] have derived a one-dimensional nonpolynomial nonlinear Schrödinger equation for a condensate trapped in a transverse harmonic potential with trapping frequency ω_{\perp} . The derivation is based on a variational approach. For the transverse part of the ground state wave function a gaussian ansatz is made

$$\phi(x, y, t; \sigma(z, t)) = \frac{1}{\sqrt{\pi}\sigma(z, t)} \exp[-(x^2 + y^2)/2\sigma(z, t)^2]. \quad (6.25)$$

The variation of the action functional associated with the 3D Gross-Pitaevskii equation is performed with respect to the width of the transverse gaussian $\sigma(z, t)$ and the longitudinal part of the wave function $\psi(z, t)$. The resulting nonpolynomial nonlinear Schrödinger equation is given by [108]

$$i\hbar \frac{\partial \psi(z, t)}{\partial t} = \left[-\frac{\hbar^2}{2m} \frac{\partial^2}{\partial z^2} + V_{ext}(z) + \frac{gN}{A_{\perp}(z, t)} |\psi(z, t)|^2 \right] \psi(z, t) \quad (6.26)$$

$$+ \left[\frac{\pi\hbar^2}{mA_{\perp}(z, t)} + \frac{m\omega_{\perp}^2 A_{\perp}(z, t)}{4\pi} \right] \psi(z, t). \quad (6.27)$$

where $A_{\perp}(z, t)$ is a function of $\psi(z, t)$

$$A_{\perp}(z, t) = \frac{2\pi\hbar}{m\omega_{\perp}} \sqrt{1 + 2a_s N |\psi(z, t)|^2}. \quad (6.28)$$

An advantage of the approach is that the influence of the external potential $V_{ext}(z)$ on the density along the z-axis is treated.

6.3 Bose-Einstein condensates in optical lattices

In this section a brief review over some of the work done in the field will be given. The aim is to give a background for the proposal presented in Chap. 7.

After theoretical suggestions in 1998 [109, 110], strongly detuned lasers were used to form effectively conservative periodic potentials, and the field of BECs in optical lattices has grown ever since.

6.3.1 The optical lattice

A one-dimensional periodic potential can be generated by two counter-propagating laser beams with equal intensity. The origin of the force felt by the atoms is the AC-Stark shift. The oscillating electric field of the light induces an electric dipole

moment in the atom. It is then the interaction between the electric field $E(\mathbf{r}, t)$ and the induced dipole moment that causes an energy shift in the atomic energy level given by

$$\Delta E(\mathbf{r}) = -\frac{1}{2}\alpha(\omega)\langle E^2(\mathbf{r}, t) \rangle, \quad (6.29)$$

where α is the polarizability of the atomic level and $\langle \rangle$ represents a cycle average. Assuming that the frequency of the light ω is red-detuned, i.e. less than the atomic resonance frequency, the induced dipole and the electric field of the light will be in phase, corresponding to $\alpha(\omega) > 0$. The resulting force on the atom is found via minus the gradient of the energy of the atomic energy level and the force will point in the direction of increasing intensity of the light field. For a transverse Gaussian laser beam a harmonic approximation can be made for the central part of the beam, leading to a transverse harmonic potential. A longitudinal periodic potential arises due to the interference of two counter-propagating laserbeams with wavelength $\lambda_L = 2\pi/k_L$ and parallel polarizations. The transverse harmonic profile multiplied on the periodic potential is normally ignored leading to a separable potential, harmonic in the radial coordinate and periodic in the longitudinal coordinate z . The z -dependent part of the potential has a lattice spacing of $d = \lambda_L/2$ and is given by

$$V(z) = -V_0 \cos(2k_L z), \quad (6.30)$$

where V_0 is usually measured in units of the recoil energy $E_R \equiv \hbar^2 k_L^2 / 2m$, with m being the mass of the atom.

By far the most research into BEC in optical lattices has been carried out in 1D, but the formation of optical lattices in two and three dimension can be achieved by adding more laser beams. The most direct extension is to add a pair of lasers perpendicular to the first set, creating a 2D lattice. By adding a last pair in the third spatial direction a 3D lattice can be formed. In fact the Mott insulator transition was first demonstrated by Greiner et al. [97] in a 3D lattice. Stöferle et al. [111] used deep lattices along two spatial directions to create arrays of tubes. They subsequently realized the Mott insulator transition in the longitudinal dimension of the tubes.

6.3.2 Linear description

The dynamics of a condensate in an optical lattice is influenced by the following parameters: The absolute number of atoms, the depth of the periodic potential, the on site interaction energy and the characteristic energy for tunneling between lattice sites.

When the nonlinear interaction energy is small compared with the strength of the periodic potential, a simple linear band structure provide very valuable results. The proposal in Chap. 7 is in this regime with a weak periodic potential of $V_0 = E_R/2$.

The band structure of the one-dimensional linear Schrödinger equation with the periodic potential in Eq. (6.30) can be found using the method listed in almost any book on solid state physics [112]. Bloch's theorem in one dimension states that the eigen wave-functions can be written as

$$\psi_{n,k}(z) = e^{iqz} u_{n,k}(z), \quad (6.31)$$

where n is referred to as the band index and k is the quasi-momentum (strictly $\hbar k$ is the quasi-momentum). The functions $u_{n,k}$ are periodic with the lattice spacing d . The eigen wave-functions and the potential can be expressed as a Fourier series

$$\psi_{n,k}(z) = \sum_K c_{k-K} e^{i(k-K)z}, \quad (6.32)$$

$$V(z) = -\frac{V_0}{2} e^{iQz} - \frac{V_0}{2} e^{-iQz}, \quad (6.33)$$

where $Q = 2k_L$ is a lattice vector and K takes the values of lattice vectors from $-sQ$ to sQ , where s is the number of points in a period of the direct lattice. Consequently the band structure $\varepsilon_{n,k}$ can be found by solving the following set of $2s + 1$ coupled linear equations

$$\left\{ \frac{\hbar^2}{2m} (k - K)^2 \right\} c_{k-K} - \frac{V_0}{2} c_{k-K-Q} - \frac{V_0}{2} c_{k-K+Q} = \varepsilon_{n,k} c_{k-K}, \quad (6.34)$$

for the quasi-momenta k in the first Brillouin zone.

Making a Taylor expansion of the band structure around a given quasi-momentum k_0 reveals useful information about the dispersive properties of a wave packet centered at k_0 . As in nonlinear optics the first derivative gives the group velocity v_g . The second derivative gives the effective mass m_{eff} corresponding to the group velocity dispersion β_2 in optics.

$$v_g(k_0) = \frac{1}{\hbar} \left. \frac{\partial \varepsilon_n(k)}{\partial k} \right|_{k_0}, \quad m_{\text{eff}}(k_0) = \hbar^2 \left\{ \left. \frac{\partial^2 \varepsilon_n(k)}{\partial^2 k} \right|_{k_0} \right\}^{-1}. \quad (6.35)$$

To keep the analogy with optics the central part of the first band in the Brillouin zone from $k = 0$ to the points of diverging m_{eff} corresponds to a region of normal dispersion since $m_{\text{eff}} > 0$. The regions around the band edges on the other hand correspond to anomalous dispersion, since $m_{\text{eff}} < 0$.

6.3.3 Nonlinear description

Due to the atom-atom interaction in the BEC, the density of the condensate in the ground state will be modulated with the period of the optical lattice, causing high density at potential minima and low density at potential maxima. Consequently, in a shallow lattice the presence of the nonlinear interaction causes an

effective periodic potential with a smaller modulation resulting in smaller band gaps and higher bandwidths [109].

For a condensate only modulated by the periodic potential, the nonlinear band structure is given by the chemical potential μ of the time-independent Gross-Pitaevskii equation

$$\left[-\frac{\hbar^2}{2m} \frac{d^2}{dz^2} - V_0 \cos(2k_L z) + \gamma |\psi(z)|^2 \right] \psi(z) = \mu \psi(z), \quad (6.36)$$

where $\gamma = \frac{gN}{A_\perp}$. The chemical potential is equal to the nonlinear eigenvalue. Equivalently to the linear case (6.31), the nonlinear eigenstates $\psi(z) = e^{ikz} u_k(z)$ can be written on the Bloch form. As in the linear case $u_k(z)$, is periodic with the lattice and k represents wave vectors in the first Brillouin zone.

The Bloch waves $u_k(z)$ can be found numerically in various ways [113, 114]. In the method applied in [113], u_k is expanded in a Fourier series and the Hamiltonian corresponding to the Gross-Pitaevskii equation (6.36) is minimized in the space spanned by the Fourier coefficients.

For small nonlinearities the band structure much resembles the band structure of a less deep periodic potential, but when the nonlinearity is considerable, the band structure is significantly altered. When the nonlinear energy becomes greater than the energy of the band gap, loops (also called swallow tails) appear in the lower band at any band edge in the structure [115]. The indication of loops was first reported in [116].

6.3.4 General stability properties

It is the presence of the periodicity together with the nonlinearity that opens the possibility for instabilities. A stability analysis is typically based on a linear excitation around an eigen state of the Gross-Pitaevskii equation leading to the Bogoliubov-de Gennes equations as explained in Sec. 6.2.5.

The stability properties are relevant since q states over major parts of the Brillouin zone will be treated in Chap. 7. The occurrence of Landau and dynamical instabilities has been investigated by Wu and Niu [113, 114]. The central part of the Brillouin zone is energetically and dynamically stable. Moving away from the center there is a region of Landau instability beyond which there is a dynamically unstable region until the edge of the Brillouin zone. In general the smallest region of dynamical instability is found for a shallow lattice and a small nonlinearity as in our proposal in Chap. 7.

Stationary states with periods equal to multiples of the lattice period have been shown to exist [117]. Additionally, a stationary state with the double period of the lattice is shown to energetically coincide with the dynamical instability at the zone boundary mentioned above. This is very interesting since the dynamical instability is consequently not incoherent in its nature, but could simply indicate a coupling to an other discrete state. This aspect will be treated in Chap. 7.

The dynamical instability has recently been experimentally investigated by Inguscio and coworkers [118, 119]. After the condensate is generated they adiabatically turn on an optical lattice generated from two counter propagating lasers with wavelength around λ and a frequency difference $\delta\nu$. The optical lattice is consequently moving with velocity $v = (\lambda/2)\delta\nu$ and the condensate is loaded into a state of well defined quasi-momentum $q = mv/\hbar$. With this experimental method, accounted for in detail in [120], the condensate can be given any desired quasi-momentum. The dynamical instability was experimentally identified in [118] by the short lifetime of the condensate in the unstable regime.

Although many experiments are performed outside the weak interaction limit, only recently the stability analysis has been generalized to include the transverse degrees of freedom. The thresholds for instabilities are scarcely affected by the transverse degrees of freedom, on the other hand the transverse excitations play an important role inside the regime of dynamical instability, indicated by complex radial dynamics [121].

6.3.5 Shallow lattices

The behavior of the BEC depends on the type of lattice it is situated in. In this section phenomena typically encountered in a shallow optical lattice will be considered.

Soliton generation, relying on the balancing of nonlinearity and dispersion, can be achieved. The negative effective mass associated with a wave packet at the band gap in an optical lattice can be balanced by repulsive atom-atom interactions leading to a bright gap soliton as experimentally demonstrated in [122]. In the article [I] the stability of these gap solitons was investigated by solving the Bogoliubov-de Gennes equations.

The fast oscillating scale associated with the lattice can be removed from the problem using a multiple scales analysis generalized from optics [100, 101], where it has been used to describe Bragg fibers with a one-dimensional modulation of refractive index. The analysis boils down to a nonlinear Schrödinger equation for the soliton envelope function, where the kinetic energy term and the periodic potential have been replaced by a kinetic energy term with an effective mass.

It should be mentioned that bright solitons can also be generated without the presence of the periodic potential. Bright solitons have been experimentally demonstrated [123, 124] in condensates of lithium-7 atoms, where the normal dispersion corresponding to the positive mass was balanced by the attractive interactions.

A force can be applied to the condensate in the periodic potential, for example by accelerating the optical lattice potential [125]. Consider a condensate wave packet with a narrow quasi momentum distribution around k_0 . If the force is adiabatically applied the condensate will cross the Brillouin zone boundary staying in the first band. Since the group velocity becomes negative after the zone boundary is crossed, the condensate starts to oscillate in space. These

so-called Bloch oscillations are discussed in [126], where also the effect of the nonlinearity is discussed.

Landau-Zener tunneling appears if the acceleration is not performed adiabatically, causing the second band to be populated after the zone boundary is crossed. Experimental studies of the Landau-Zener tunneling effect as well as the influence of the atom-atom interaction on the effect are reported in [127]. The tunneling probability increases due to the interactions. The atoms gather at the potential wells, leading to a smaller modulation of the effective potential and hence a smaller band gap and higher tunneling probability [128]. Anderson and Kasevich made a pulsed atom laser in 1998 [129] by coupling atoms out of the condensate in a vertical periodic potential. The gravitation was acting as the accelerating force in this Landau-Zener tunneling process.

6.3.6 Deep lattices

In the case of a deep periodic potential the Bloch states exhibit strong localization at the lattice sites (the tight binding limit). Consequently, a Wannier basis, where the eigenfunctions are located at the potential minima, can often be more useful [130]. The linear Wannier states can be modified to take the effect of the atom-atom interactions into account.

When the number of atoms per lattice site becomes small, the mean field description of the Gross-Pitaevskii equation is no longer fully valid, because the particle correlations need to be properly accounted for. Instead, the Bose-Hubbard Hamiltonian was suggested in 1998 [110] for describing the system of N ultracold atoms confined by the combined potential of a harmonic trap and an optical lattice:

$$\hat{H} = -J \sum_{\langle ll' \rangle} \hat{b}_l^\dagger \hat{b}_{l'} + \frac{U}{2} \sum_l \hat{n}_l (\hat{n}_l - 1) + \sum_l \varepsilon_l \hat{n}_l. \quad (6.37)$$

Here $\langle ll' \rangle$ represents the sum over nearest neighbour pairs [131], ε_l denotes the energy at site l associated with the harmonic potential, \hat{n}_l is the atom number operator and \hat{b}_l^\dagger and \hat{b}_l are the boson creation and annihilation operators at site l . Again, the on site interaction energy is denoted U and J is the tunneling energy from site to site.

For a shallow lattice the atoms move between adjacent wells due to a small on site interaction and a high probability for tunneling, corresponding to a small ratio U/J . The condensate has a well determined phase, since each atom is smeared out over the entire lattice and the quantum gas is in the superfluid phase. As the depth of the periodic potential increases the probability for tunneling between adjacent wells becomes very small. The transition to the Mott insulator phase occurs when the ratio between the on site interaction energy U and the tunneling energy J from site to site is above a critical value. If the number of lattice wells is assumed equal to the number of atoms, then the interaction energy associated with placing two atoms at the same site is so big that it is energetically very unfavourable for the system to do it. Consequently, in the Mott

insulator state there is exactly one atom in each well, and the total wave function can be written as a product of Fock states for the lattice sites. Since there is no uncertainty in the atom number the phase of the gas is now completely uncertain. It should be mentioned that the Mott insulator phase exists for $n = 2, 3, 4, \dots$ atoms per lattice site as well and the critical value of U/J depend on n [131].

6.3.7 Superlattices

A superlattice with a period three times as long as the period of the underlying lattice has been used by W. D. Phillips and his group to load atoms into every third lattice site [132]. If atoms in optical lattices shall be used for quantum information processing, this is certainly a step forward, since it improves the ability to address single atoms.

The introduction of a superlattice, implies the appearance of new gaps in the band structure of the total system. For a shallow superlattice the introduced gaps will be narrow (mini-gaps), with associated relatively high curvature and dispersion. The high magnitude of the dispersion is exploited in the proposal [133] where the generation of gap solitons is suggested based on the superposition of two wave-packets with opposite momenta $\pm k$ generated with Bragg scattering. The momenta $\pm k$ are given by the momenta at a mini-gap.

6.4 Conclusion

BECs in optical lattices provide a valuable model system with full control over the parameters of the system. The superfluid - Mott insulator transition illustrates how the system can be used to investigate strongly correlated many body quantum mechanics. The field of nonlinear matter waves is blessed with the opportunities associated with the continuous control during an experiment of the lattice geometry in 1D, 2D or 3D. This control surpasses the flexibility provided today in nonlinear optics by photonic crystals. On the other hand the photonic crystals offer immense freedom with respect to engineering dispersive properties. Often the findings in nonlinear optics can be directly transferred to nonlinear atom optics: Inspired by the importance of the FWM process accounted for in Chap. 5, the possibilities for four wave mixing in a BEC in an optical lattice will be investigated in the following chapter.

CHAPTER 7

Phase-matched four wave mixing and quantum beam splitting of matter waves in a periodic potential

The aim of this chapter is to show that the dispersion properties imposed by an external periodic potential ensure both energy and quasi-momentum conservation such that correlated pairs of atoms can be generated by FWM from a Bose-Einstein condensate moving in an optical lattice potential. A condensate with initial quasi-momentum k_0 is transferred into a pair of correlated atomic components with quasi-momenta k_1 and k_2 , if the system is seeded with a smaller number of atoms with the appropriate quasi-momentum k_1 . This process is revealed in the numerical solution to the Gross-Pitaevskii equation and the transfer in the process is almost complete ($>95\%$). The chapter is based on paper [VI].

7.1 Introduction

As discussed in the previous chapter, BECs in optical lattices provide flexible systems for the study of matter waves in periodic potentials and nonlinear physical phenomena in general.

The FWM process considered transfers pairs of atoms coherently from an initial momentum state k_0 to new states with momenta k_1 and k_2 . The longitudinal dynamics of a BEC in a quasi-1D geometry will be considered. This geometry is relevant, e.g., for atomic wave guides and atom interferometers based on atom chips [134].

In Refs. [135, 136], it was shown that nonlinear interaction originating from the s-wave scattering between atoms leads to depletion of the condensate and emission of pairs of atoms at other momenta when a continuous matter wave beam passes through a finite region with enhanced interactions. For a larger condensate, however, the process will not be effective unless it conserves both energy and momentum, i.e., the waves must be phase-matched over the extent of the sample. The periodic potential in optical lattices points to the use of physical pictures and phenomenology from solid state physics [112], and in this chapter it will be shown how the characteristic energy band structure in a one-dimensional optical lattice can be used to ensure both energy and quasi-momentum conservation, i.e., phase-matching of the FWM process.

In fact our FWM process has an analog in the solid state system of a semiconductor microcavity. The normal modes of the light-matter coupling in the cavity are exciton polaritons having a dispersion relation ensuring energy and momentum conservation for the FWM process. Consequently, when the phase-matching condition is fulfilled and the signal mode $k = 0$ is weakly excited, two pump polaritons at k_p are converted into a pair of polaritons at wave-vectors 0 and $2k_p$ [137–139].

As explained in Chap. 5 phase-matched FWM plays a central role in the propagation of light in PCFs [IV-V]. The importance of the process in the PCFs, where the dispersion of the fiber is responsible for the phase-matching, indeed gave the inspiration to the present proposal, where phase-matching is instead achieved by exploiting the dispersion in an optical lattice.

It should be mentioned that phase-matched FWM has been realized in collisions of two condensates in two dimensions [140–143], but in the present proposal it is shown that the process can take place with atomic motion along a single direction, for example inside an atomic waveguide.

As mentioned previously in the thesis, a recent analysis [102] of the break-up of a bright matter wave soliton was analyzed in terms of dispersion and phase-matching. The system has a direct analog in nonlinear optics where solitons break up and emit nonsolitonic radiation as discussed in Chap. 4.

7.2 Phase-matched four wave mixing

For the degenerate FWM process to be phase-matched, the energy of the interacting particles has to be conserved, as illustrated in Fig. 7.1. As previously mentioned, the phase-matching is achieved by exploiting the dispersion relation imposed by a periodic potential $V(z)$. This basic idea of our proposal is illustrated in Fig. 7.2. In a periodic potential, the energy spectrum constitutes a band structure, and the figure shows the lowest energy band for the corresponding linear Schrödinger equation. When two atoms with momentum k_0 collide and leave with momenta k_1 and k_2 momentum conservation requires

$$2k_0 = k_1 + k_2 \text{ modulo } Q, \quad (7.1)$$

where Q is a reciprocal lattice vector. In the periodic potential the energy does not vary quadratically with the wave number, and as indicated by example in Fig. 7.2, it is possible to identify sets of wave numbers with conservation of the total energy

$$2\varepsilon_0 = \varepsilon_1 + \varepsilon_2. \quad (7.2)$$

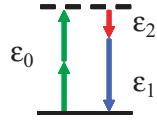


Figure 7.1: Energy conservation in degenerate FWM $2\varepsilon_0 = \varepsilon_1 + \varepsilon_2$.

7.3 Mean-field analysis

To investigate the effectiveness of this degenerate FWM process, a mean field analysis of the dynamics of the condensate was performed. The analysis was based on the one-dimensional Gross-Pitaevskii equation (6.23)

$$i\hbar \frac{\partial \psi(z, t)}{\partial t} = \left(-\frac{\hbar^2}{2m} \frac{\partial^2}{\partial z^2} + V(z) + \gamma |\psi(z, t)|^2 \right) \psi(z, t), \quad (7.3)$$

where the periodic potential $V(z)$ is given by

$$V(z) = -V_0 \cos(2k_L z), \quad (7.4)$$

and V_0 will be given in units of the recoil energy $E_R \equiv \hbar^2 k_L^2 / 2m$. As described in Sec. 6.3.1 the periodic potential can be generated with a standing wave of a laser with wavelength $\lambda_L = 2\pi/k_L$. Again the factor

$$\gamma = gN/A_\perp \quad (7.5)$$

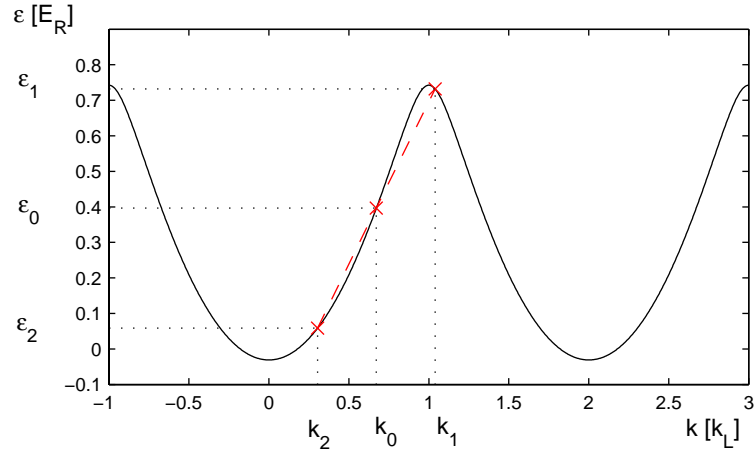


Figure 7.2: Band structure for atomic motion in the periodic potential Eq. (7.4). Quasi-momentum conservation and energy conservation is fulfilled in the crosses where two atoms with momentum k_0 collide and separate at momenta k_1 and k_2 illustrated in the figure.

describes the strength of the nonlinearity, where N is the total number of atoms in the condensate, A_{\perp} is again the area of the transverse ground state, and the coupling constant g is given by Eq. (6.5). In the calculation presented below $V_0 = E_R/2$ and $\gamma = 40.8E_R/k_L$ corresponding to $N = 100000$ ^{87}Rb atoms confined to a transverse area of $A_{\perp} = 42\mu\text{m}^2$ and a grid of 512 periods of the potential. These parameters are compatible with a Gaussian variational ansatz to the radial distribution in a harmonic potential with $\omega_{\perp} = 2\pi \times 44\text{Hz}$ [108, 121]. In this ansatz, the transverse area is given by Eq. (6.28) and for $|\psi(z, t)|^2$ has been used the average value of the density of the condensate over the entire grid. The above parameters correspond to 500 atoms per μm , whereas the weak interaction limit, defined in Sec. 6.2.6, is equivalent to 100 atoms per μm for ^{87}Rb . As the density in the condensate is higher than the limit, the ansatz above has been used to take the effect of interactions on the transverse area into account.

An eigenstate ψ_0 of the condensate with quasi-momentum k_0 is found using the method of steepest descent propagation, assuming a solution according to Bloch's theorem on a single period of the lattice potential. Subsequently, a seed at variable k_1 is applied giving the following initial wave function

$$\psi_{\text{init}}(z) = \frac{1}{\sqrt{1+\alpha^2}} \left[1 + \alpha e^{i(k_1-k_0)z} \right] \psi_0(z), \quad (7.6)$$

where $\alpha = 0.1$ has been used in our calculations with the Gross-Pitaevskii equation.

One way to generate the initial wave function $\psi_{\text{init}}(z)$ is to produce a condensate with quasi-momentum k_0 by adiabatically loading the condensate into a pe-

riodic potential moving with the velocity $v = \hbar k_0/m$, as explained in Sec. 6.3.4. Subsequently, the initial state $\psi_{\text{init}}(z)$ can be produced by a Bragg diffraction process, which coherently couples the momentum states k_0 and k_1 using a configuration of two counter-propagating lasers with wave-vectors k_0 and k_1 . Similar Bragg diffraction processes were used in the initial demonstration of FWM in two dimensions in a BEC [141].

7.4 Mean field results

The wave function $\psi_{\text{init}}(z)$ does not fulfill Bloch's theorem on a single period of the potential. Values of k_0 and k_1 corresponding to integer numbers of wavelengths are chosen on an extended grid of 512 periods. Consequently, the interference pattern seen in the density of $\psi_{\text{init}}(z)$ is periodic on this extended grid.

To test the importance of phase-matching in the FWM process the wave function ψ_{init} is propagated on this grid, with different values for the seeded momentum component k_1 . As a function of time, the evolution of the Gross-Pitaevskii wave function and build-up of amplitude at different momenta are observed. Particular interest is paid to the quasi-momentum regions around k_0 , k_1 and $k_2 = 2k_0 - k_1$. Let $\psi(k, t)$ denote the Fourier transform of the time-dependent Gross-Pitaevskii wave-function $\psi(z, t)$. The distribution in momentum space folded into a single Brillouin zone from $k = 0$ to $Q = 2k_L$ is shown in Fig. 7.3. As a function of time and the seeding momentum component k_1 , the population around the k_0 , k_1 and k_2 momentum components are calculated using the following expression

$$P_{k_i}(t, k_1) = \sum_n \int_{k_i - \Delta k/2}^{k_i + \Delta k/2} |\psi(k + nQ, t, k_1)|^2 dk, \quad i = 0, 1, 2, \quad (7.7)$$

where a sampling over a narrow momentum window with $\Delta k = k_L/32$ has been introduced. The window is indicated with dotted lines in Fig. 7.3 and it is broad enough to ensure integration over the entire area of the peak.

Fig. 7.4 (a) shows the part of the condensate, $P_{k_0}(t, k_1)$, remaining in the vicinity of the initial quasi-momentum k_0 when the condensate is seeded with different values of k_1 . The most important features in the figure occur when the condensate is seeded with $k_1 = 1.055k_L$ and $k_1 = 0.289k_L$. The original condensate fraction at k_0 is almost completely depleted, and strong growth of the population of the seeded momentum state is shown in $P_{k_1}(t, k_1)$ in part (b), accompanied by simultaneous growth in the phase-matched component $k_2 = 2k_0 - k_1$, shown as $P_{k_2}(t, k_1)$ in part (c) of the figure. Comparing the set $(k_0, k_1, k_2) = (0.672k_L, 1.055k_L, 0.289k_L)$ with the set of phase-matched wave vectors in Fig. 7.2 extremely good agreement is found and the conclusion is that the structure at $k_1 = 1.055k_L$ is indeed due to the phase-matched FWM process.

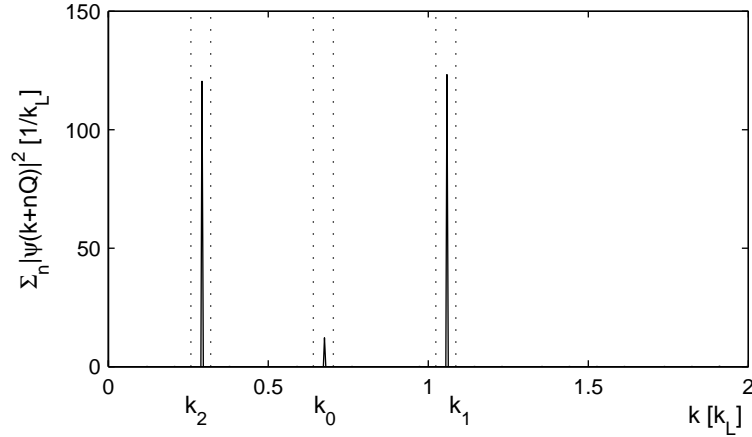


Figure 7.3: The distribution in momentum space folded into a single Brillouin zone $\sum_n |\psi(k+nQ)|^2$. In this figure the time of propagation is $t = 0.012$ s, and pairs of atoms at k_0 have efficiently been converted into pairs of atoms at k_1, k_2 . The sampling windows of $\Delta k = k_L/32$ used in Eq. (7.7) are indicated by dashed lines in the figure.

7.4.1 Double four wave mixing

The remaining structures in Fig. 7.4 are less prominent but for instance the structure in Fig. 7.4 (b) after 25 ms at $k'_1 = 0.492k_L$ can be identified as a double FWM process with the following steps: $2k_0 \rightarrow k'_1 + k'_2$ and $k_0 + k'_2 \rightarrow k'_1 + k'_3$, where $k'_3 = k'_2 + (k_0 - k'_1)$. These steps do not conserve energy but the resulting six wave mixing process ($3k_0 \rightarrow 2k'_1 + k'_3$) is resonant. The time evolution of the population of the momentum components k_0, k'_1, k'_3 is shown in Fig. 7.5. The figure indeed confirms that the k'_1 component is twice as populated as the k'_3 component. It is again the phase-matching that is responsible for the significance of this process.

7.5 Varying k_0

Calculations with the Gross-Pitaevskii equation (7.3) have been performed for various k_0 and the identified phase-matched sets of wave vectors (k_0, k_1, k_2) are plotted as crosses in Fig. 7.6. A simple band structure calculation based on a linear Schrödinger equation, as described in Sec. 6.3.2, was performed to quantitatively understand the occurring sets of wave vectors. Subsequently, the sets of wave vectors fulfilling energy and quasi-momentum conservation were extracted, as illustrated in Fig. 7.2. The phase-matched quasi-momenta k_0 occur within the interval: $k_L/2 < k_0 < k_{zm}$, where $k_L = Q/2$ and k_{zm} is a point of zero

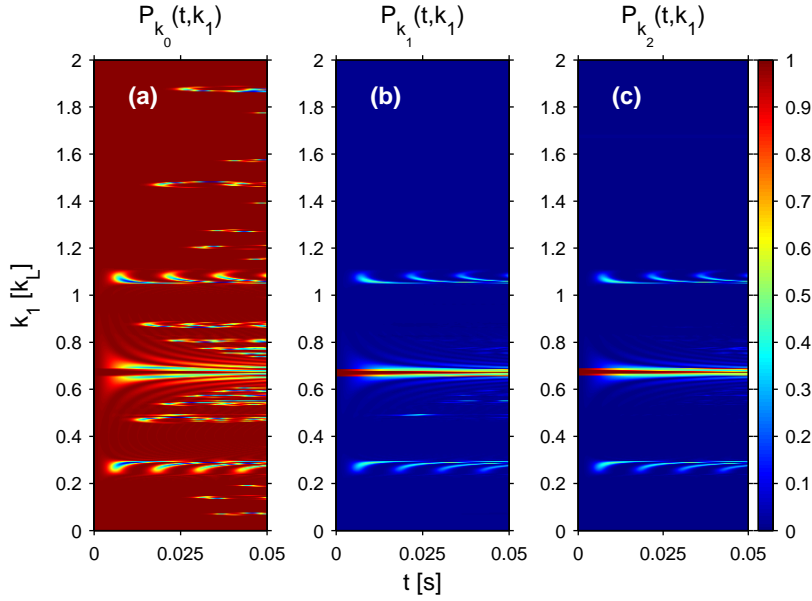


Figure 7.4: Population of different momentum components (a): $P_{k_0}(t, k_1)$, (b): $P_{k_1}(t, k_1)$ and (c): $P_{k_2}(t, k_1)$ as a function of time and as function of the seeding wave vector k_1 . The calculations are performed with a potential modulation $\beta = 1/2$, $N = 100000$ atoms, and an initial wave vector of $k_0 = 0.672k_L$. When (k_0, k_1, k_2) fulfill the phase-matching conditions in Eq. (7.1) and (7.2), which is the case for $k_1 = 0.289k_L, 1.055k_L$, the condensate originally having wave vector k_0 is efficiently transferred into a set of atomic clouds with wave vectors k_1 and k_2 .

effective mass in the band structure ($\frac{d^2\varepsilon}{dk^2}|_{k_{zm}} = 0$). Those sets of wave vectors are plotted as the full line in Fig. 7.6. This simple procedure produces results very much in agreement with those obtained by the full numerical solution. For completeness a calculation including the effect of interactions is also presented. To calculate the band structure for quasi-momentum states of atoms outside the k_0 condensate state, the excitations are assumed particle-like and the following equation is solved:

$$\left(-\frac{\hbar^2}{2m} \frac{d^2}{dz^2} + V(z) + 2\gamma|\psi_0(z)|^2\right)u(z) = \varepsilon u(z), \quad (7.8)$$

sometimes referred to as the Popov approximation to the coupled Bogoliubov-de Gennes equations for the problem, and the method consequently gives an expression for the excitation spectrum. The argument for assuming the excitations to be particle-like is that the system is close to the weak interaction limit and the character of the quasi-particles is close to the character of the particles in a weakly interacting condensate [144]. The mean-field interaction term $2\gamma|\psi_0(z)|^2$ depends on k_0 and amounts to less than a five percent correction to $V(z)$. Hence,

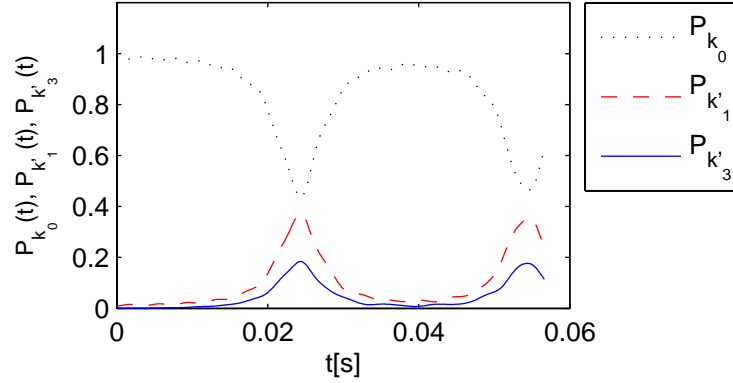


Figure 7.5: Time evolution of the population P_{k_i} of the momentum components $k_0 = 0.672k_L, k'_1 = 0.492k_L, k'_3 = 1.03k_L$. The state k'_1 is twice as populated as the state k'_3 , due to the double FWM process, effectively leading to the conversion $3k_0 \rightarrow 2k'_1 + k'_3$.

$\psi_0(z)$ is identified and Eq. (7.8) is solved for each quasi-momentum k_0 and band structures are derived from which the phase-matched pair k_1, k_2 of final momenta are extracted. Sets of (k_0, k_1, k_2) having $k_L/2 < k_0 < k_{zm}$ found with this method are shown by the dashed curve in Fig. 7.6. As expected the inclusion of the interactions only slightly changes the phase-matching condition. It should be noted that the above approach does not fully account for the effect of interactions and a comparison with the phase-matching condition based on the nonlinear band structure described in Sec. 6.3.3 could be interesting.

7.6 Rabi-oscillations

The original expectations were that the phase-matched, degenerate FWM could be achieved in a perturbative regime with only few atoms expelled from the original condensate. When the process is phase-matched, however, the calculations show an extremely high conversion efficiency (up to 95%). The populations at the set of phase-matched wave vectors $(k_0, k_1, k_2) = (0.672k_L, 1.055k_L, 0.289k_L)$ depicted in Fig. 7.4 are displayed more clearly in Fig. 7.7 (a), (b), (c) and they show clear oscillatory behavior. Such Rabi-like oscillations are normally met in transitions between discrete states, but, as illustrated in Fig. 7.2, increasing k_1 (and decreasing k_2) lowers the energy of both states, whereby energy conservation restricts the coupling to a narrow part of the momentum state continuum, in which case the dynamics passes to Rabi oscillatory dynamics [145]. Additionally, the Rabi-frequency of these oscillations is proportional to the coupling

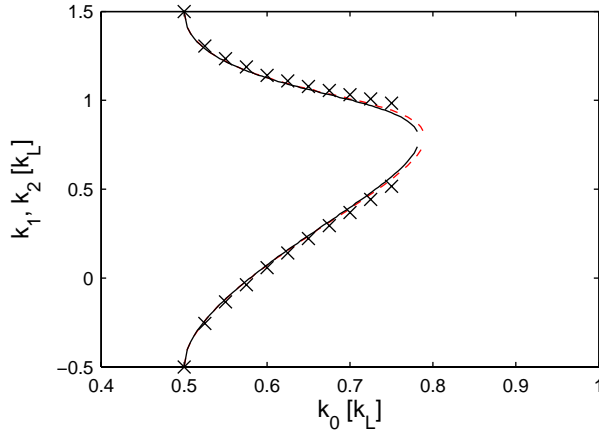


Figure 7.6: Identification of momentum states (k_0, k_1, k_2) fulfilling the phase-matching condition. Crosses: sets of phase-matched values (k_0, k_1, k_2) identified by numerical solution of the Gross-Pitaevskii equation (7.3). Full line: phase-matching condition derived from band structure based on simple linear Schrödinger equation. Dashed line: phase-matching condition when the effects of interactions have been included as in Eq. (7.8). Although the simple band structure calculations are not exact theories for the phase-matching condition there is still excellent agreement with the full mean-field calculation.

strength between the initial and final sets of states [145]. In the present situation the coupling is given by the nonlinear interaction term which is initially proportional to N and consequently the Rabi-frequency is expected to be proportional to N . A Gross-Pitaevskii simulation with half the amount of atoms as compared with Fig. 7.4 has been performed and the populations are displayed in Fig. 7.8. The set of phase-matched wave vectors $(k_0, k_1, k_2) = (0.672k_L, 1.047k_L, 0.297k_L)$ are more clearly displayed in Fig. 7.7 (d), (e), (f), and, indeed, approximately half the Rabi-oscillation frequency is observed. Note the slightly different values of (k_1, k_2) due to the effect of the interactions on the phase-matching condition. The Rabi frequency depends not only on the number of atoms and the collisional coupling strength, as mentioned above, but also on the density of states in the final state.

In Fig. 7.4 oscillatory behavior is seen above the resonant value of $k_1 = 1.055k_L$ as chirps. Above this value of k_1 energy is no longer conserved in the FWM process and the phenomenon can be explained as Rabi oscillations with a detuning and a larger generalized Rabi frequency $\Omega = \sqrt{\kappa^2 + \Delta^2}$ explaining the faster oscillations [145].

As previously mentioned, an equivalent FWM process with exciton polaritons was investigated in a solid state system of a semiconductor micro cavity. The Rabi oscillations predicted in the BEC system were not observed in the solid state system due to fast dephasing rates [137–139].

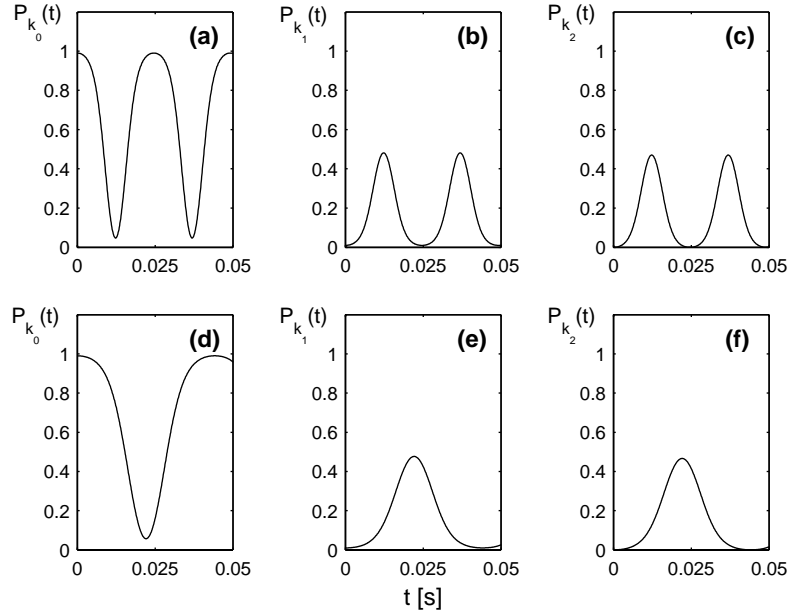


Figure 7.7: The condensate evolution based on the Gross Pitaevskii equation for sets of phase-matched wave vectors: (a): $P_{k_0=0.672k_L}(t)$, (b): $P_{k_1=1.055k_L}(t)$ and (c): $P_{k_2=0.289k_L}(t)$ for $\beta = 1/2$ and $N = 100000$. The evolution of the phase-matched components of the condensate with half the number of atoms ($N = 50000$) is shown in (d): $P_{k_0=0.672k_L}(t)$, (e): $P_{k_1=1.047k_L}(t)$ and (f): $P_{k_2=0.297k_L}(t)$. Half the oscillation frequency is observed since the oscillation frequency is proportional to the number of atoms.

7.7 Wave function in direct space

The time evolution of the wave function in direct space at resonance is plotted in Fig. 7.9 for the central $10 \mu\text{m}$ of the lattice. The corresponding populations in the momentum components $k_0 = 0.672k_L$, $k_1 = 1.055k_L$ and $k_2 = 0.289k_L$ were plotted in Fig. 7.7 (a)-(c). The bands at $t=12$ ms and $t=36$ ms in Fig. 7.9 (a) correspond to the almost complete transfer of $2k_0$ into k_1 and k_2 found in Fig. 7.7 (a)-(c). In part (b) of Fig. 7.9 the evolution in the first band around $t=12$ ms is shown. Due to the interference of the k_1 and k_2 momentum components of the condensate, the density exhibit a strongly spiked pattern. In Fig. 7.9 (c) the density at $t=0$ and 12 ms is compared.

Recently stationary period-doubled eigenstates of the Gross-Pitaevskii equation were found and investigated [117]. The state pictured in Fig. 7.9 is certainly not stationary. Anyhow, the state has a longer period than the single lattice due to the presence of both the momentum components k_1 and k_2 and it can therefore be categorized as belonging to the family of period doubled states.

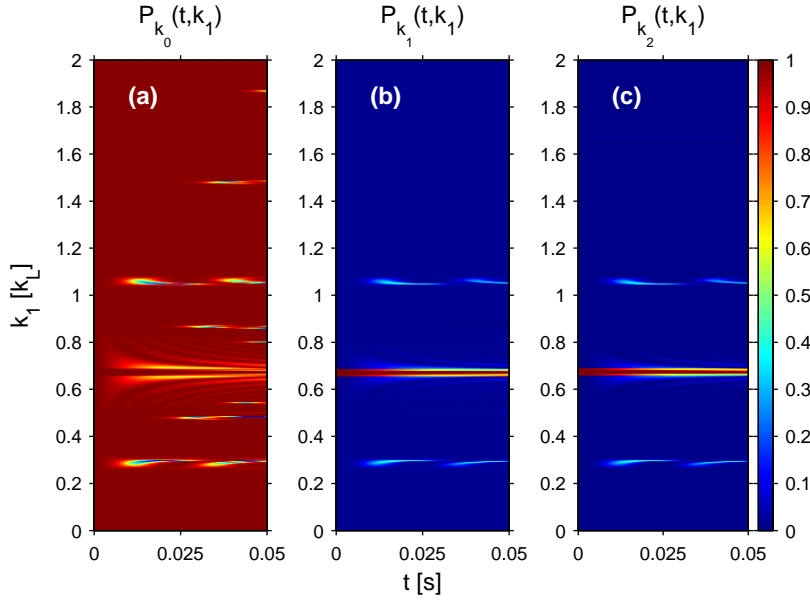


Figure 7.8: Population of different momentum components (a): $P_{k_0}(t, k_1)$, (b): $P_{k_1}(t, k_1)$ and (c): $P_{k_2}(t, k_1)$ as a function of time and as function of the seeding wave vector k_1 . The figure is equivalent to Fig. 7.4 but the simulations are performed for $N = 50000$. The set of momentum components $(k_0, k_1, k_2) = (0.672k_L, 1.047k_L, 0.297k_L)$ fulfill the phase-matching conditions in Eq. (7.1) and (7.2).

7.8 Number state analysis

In general the mean field approximation is doing well when describing thermodynamics and density distributions of a condensate with many particles $N \gg 0$. On the other hand, when it comes to investigations of correlations and statistics it is generally necessary to return to the second quantization.

The mean field analysis has shown that only the phase-matched modes are involved in the FWM process. Now an extreme case will be considered, where the correlations between the specific momentum states involved in the FWM process is investigated by performing a number state analysis. The starting point for the analysis is the second quantized Hamiltonian in momentum space for a homogeneous gas occupying the volume V [86]:

$$\hat{H} = \sum_k \varepsilon_k \hat{a}_k^\dagger \hat{a}_k + \frac{f}{2} \sum_{k, k', q} \hat{a}_{k+q}^\dagger \hat{a}_{k'-q}^\dagger \hat{a}_{k'} \hat{a}_k. \quad (7.9)$$

$f = Ng/V$ and g is again the strength of pseudo-potential given in Eq. (6.5). The operator \hat{a}_k^\dagger creates and \hat{a}_k annihilates a particle with momentum k and the

operators fulfill the bosonic commutation relations Eq. (6.11).

The role of spontaneous formation of the pairs (k_1, k_2) in comparison with the seeded process is specifically investigated by performing a number state analysis. In the analysis population is only assumed in the modes with quasi-momenta k_0, k_1 and k_2 . By choosing this restricted few mode basis both energy and momentum conservation has been assumed. In this basis the Hamiltonian above can be written as

$$\hat{H} = \frac{f}{2} \left(\sum_{i,j=0,1,2} \hat{a}_{k_i}^\dagger \hat{a}_{k_j}^\dagger \hat{a}_{k_j} \hat{a}_{k_i} + \sum_{i=0,1,2, j \neq i} \hat{a}_{k_i}^\dagger \hat{a}_{k_j}^\dagger \hat{a}_{k_i} \hat{a}_{k_j} + \hat{a}_{k_1}^\dagger \hat{a}_{k_2}^\dagger \hat{a}_{k_0} \hat{a}_{k_0} + \hat{a}_{k_2}^\dagger \hat{a}_{k_1}^\dagger \hat{a}_{k_0} \hat{a}_{k_0} + \hat{a}_{k_0}^\dagger \hat{a}_{k_0}^\dagger \hat{a}_{k_1} \hat{a}_{k_2} + \hat{a}_{k_0}^\dagger \hat{a}_{k_0}^\dagger \hat{a}_{k_2} \hat{a}_{k_1} \right). \quad (7.10)$$

The two sums describe processes conserving the number of atoms in each of the states k_0, k_1 and k_2 . The next two terms remove pairs of k_0 atoms and create k_1, k_2 pairs. The last terms correspond to the reverse processes.

As mentioned, the energy of the momentum states involved in the FWM process is assumed conserved, such that $2\varepsilon_0 = \varepsilon_1 + \varepsilon_2$, where ε_i is the eigenenergy of the linear part of the Hamiltonian for the momentum state k_i . Consequently, the modes considered in the number state analysis are chosen based on the phase-matching condition imposed by a linear band structure calculation. Since the linear energy is conserved for all the processes considered in the second quantized Hamiltonian above there was no need to include the linear energy term

$$\sum_k \varepsilon_k \hat{a}_k^\dagger \hat{a}_k. \quad (7.11)$$

The time-dependent condensate wave function can be expressed in the number state basis as

$$|\psi(t)\rangle = \sum_{n_{k_0}, n_{k_1}, n_{k_2}} c_{n_{k_0}, n_{k_1}, n_{k_2}}(t) |n_{k_0}, n_{k_1}, n_{k_2}\rangle \quad (7.12)$$

$$= \sum_n c_n(t) |N - s - 2n, s + n, n\rangle = \sum_n c_n(t) |\underline{n}\rangle, \quad (7.13)$$

where n_{k_i} is the number of atoms in the k_i state. The total number of atoms $N = n_{k_0} + n_{k_1} + n_{k_2}$ is conserved for the system. Additionally, the difference $s = n_{k_1} - n_{k_2}$ is conserved, since the atoms are always converted into pairs k_1, k_2 . Furthermore, s is equal to the number of atoms with which the state k_1 is initially seeded. The number state $|\underline{n}\rangle$ is named after the number of created pairs n , which is equal to the number of atoms n_{k_2} in the state k_2 . The k_0 state is occupied with the remaining $N - s - 2n$ atom.

The action of the Hamiltonian (7.10) on a single $|\underline{n}\rangle$ state can be written as

$$\hat{H}|\underline{n}\rangle = \alpha(n)|\underline{n}-1\rangle + \beta(n)|\underline{n}\rangle + \gamma(n)|\underline{n}+1\rangle, \quad (7.14)$$

with the coefficients

$$\alpha(n) = f\sqrt{(n+s)(n)(N-2n-s+1)(N-2n-s+2)}, \quad (7.15)$$

$$\beta(n) = \frac{f}{2}\{(N-2n-s)(N-2n-s-1) + (n+s)(n+s-1) + n(n-1) + 4(N-2n-s)(n+s) + 4(N-2n-s)n + 4(n+s)n\}, \quad (7.16)$$

$$\gamma(n) = \alpha(n+1). \quad (7.17)$$

The other number states are consistently defined as

$$|n+1\rangle = |N-2n-s-2, n+s+1, n+1\rangle, \quad (7.18)$$

$$|n-1\rangle = |N-2n-s+2, n+s-1, n-1\rangle. \quad (7.19)$$

Consequently the time dependent Schrödinger equation for the c_n coefficients is given by

$$i\hbar\dot{c}_n(t) = \alpha(n)c_{n-1}(t) + \beta(n)c_n(t) + \gamma(n)c_{n+1}(t). \quad (7.20)$$

Fig. 7.10 (a)-(c) show the evolution with time of the c_n coefficients, starting with a number state of $N-s$ atoms in the k_0 state and s atoms in the k_1 state. The mean number of atoms $\langle n_{k_i} \rangle = \langle \hat{a}_{k_i}^\dagger \hat{a}_{k_i} \rangle$ has been calculated in these three cases as illustrated in Fig. 7.10 (d)-(f). For the k_0 state the mean number of atoms is illustrated with a dotted line, for the k_1 state with a dashed line, and for the k_2 state with a full line.

In Fig. 7.10 (a), where there is no seeding corresponding to $s=0$, there is only a small fraction of population transferred from the k_0 to the k_1, k_2 states and after 50 ms the system is strongly dephased. Fig. 7.10 (d) shows the mean number of atoms and the almost vanishing $\langle n_{k_1} \rangle$ and $\langle n_{k_2} \rangle$ for $t > 25$ ms are the outcome of the dephasing process. In Fig. 7.10 (b) the condensate has been seeded with $s=10$ atoms and the system is seen to perform several oscillations between the k_0 state and the k_1, k_2 states, but after the 50 ms significant dephasing is observed and confirmed by the calculation of the mean number of atoms shown in Fig. 7.10 (e). Finally in Fig. 7.10 (c) the condensate has been seeded with $s=100$ atoms and the system is seen to perform several oscillations without significant dephasing, in agreement with the mean number of atoms pictured in Fig. 7.10 (f).

7.8.1 Detuning

Energy conservation of the linear single particle energy ε_k among the three different momentum components in the FWM process has been assumed in this number state analysis. Therefore, the effect on the exact phase-matching condition stemming from the nonlinear interaction energy has not been included. In the analysis based on the Gross-Pitaevskii equation the nonlinear interaction

was seen to slightly shifts the values for perfect phase-matching. As a consequence the Rabi-oscillations observed in the number state analysis are slightly detuned leading to a higher oscillation frequency Ω since

$$\Omega = \sqrt{\Delta^2 + \kappa^2} \quad (7.21)$$

where Δ is the detuning and κ is the oscillation frequency at resonance. In fact a higher oscillation frequency is observed in comparison with the frequency obtained from the analysis based on the Gross Pitaevskii equation, where the oscillations at exact resonance are shown in Fig. 7.7 (a)-(c) for the same density of atoms. In addition, the detuning explains that the k_0 state is not completely depleted in the number state analysis even with a high level of seeding.

7.8.2 Conclusion on number state analysis

The number state analysis confirms efficient transfer when the FWM process is seeded, and also confirms that seeding is a necessary condition for the process to start. The quantum fluctuations are not enough to significantly populate the k_1, k_2 states, consequently the dephasing of the states appear within one oscillation period, when there is no seeding. On the other hand it is concluded that the process is efficient when seeded and the quantum nature of the system does not impose too fast dephasing for the process to be dominant.

7.9 Conclusion

In conclusion the process of phase-matched FWM in a BEC in a periodic potential can be extremely efficient. When seeded, up to 95% of the atoms originally in the condensate with wave vector k_0 can be transferred into the correlated pair of states with k_1 and k_2 . The system can be used as a source of correlated atomic clouds where pairs can be easily separated due to the rather large momentum difference between k_1 and k_2 . Because of the coupling to a very narrow continuum of states the system performs Rabi-oscillations between the k_0 and the k_1, k_2 states, a behavior confirmed by the number state analysis with few modes.

As mentioned in Sec. 6.2.6, potentially better descriptions than the simple Gross-Pitaevskii equation [121] have been proposed to describe transversely confined elongated condensates. The main mechanism in the proposal relies on the non-trivial band structure, but not on its particular shape, and it is believed that the proposal should remain generally valid. Transverse confinement is, however, an important issue, and it is a natural extension of the theory to consider transverse excitations and, more generally, motion in 2D or 3D lattices, where energy conservation and phase-matching may lead to a range of interesting solutions.

The additional periodicity introduced by the superlattice mentioned in Sec. 6.3.7 opens a wide range of opportunities. It could be interesting to investigate the possibilities for energy conservation and phase-matching, in particular for

the phase-matched four-wave mixing process, that has been treated here. Furthermore, the possibility for making FWM of gap solitons could be investigated.

As discussed in Sec. 6.3.4, theories [114, 121] have proposed and experiments [118, 146] have shown that condensates moving in periodic potentials become unstable for certain ranges of quasi-momenta. These results are linked with the energy and momentum conserving processes identified in this chapter, but they also involve the detailed properties of the transverse confinement [121]. The calculations assume a lower density of atoms than in the experiments reported in [146], and in this regime only few atom pairs are expected to be spontaneously scattered, and the seeded process will be dominant.

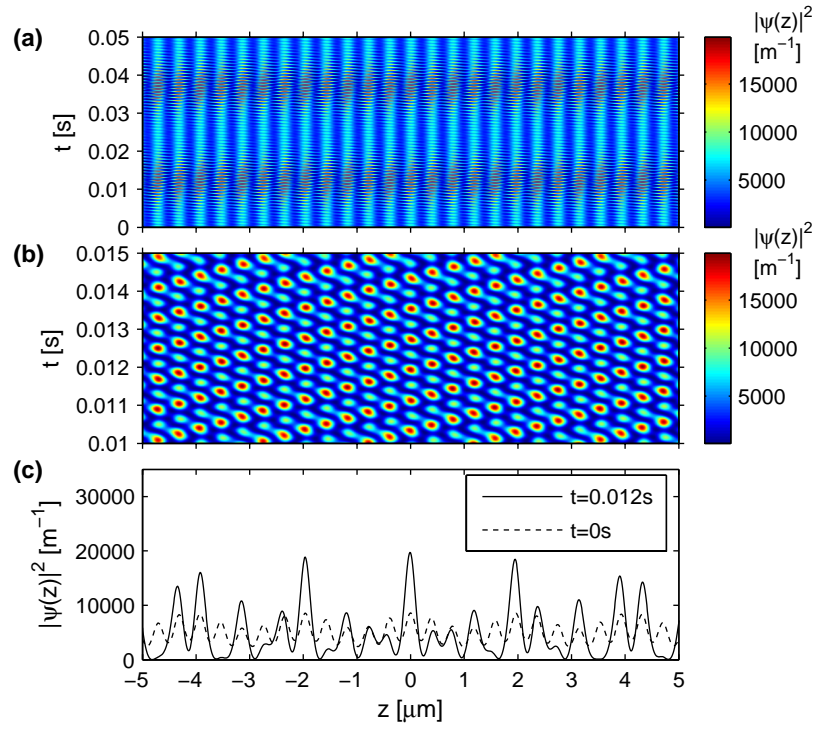


Figure 7.9: The density of the condensate wave function in direct space at resonance corresponding to $k_0 = 0.672k_L$, $k_1 = 1.055k_L$ and $k_2 = 0.289k_L$. For the simulation shown in this figure the associated populations in the momentum components are plotted in Fig. 7.7 (a)-(c). (a) The time evolution of $|\psi(z)|^2$ from $t=0$ to 50 ms. Bands are identified at $t=12$ ms and $t=36$ ms corresponding to the almost complete transfer of $2k_0$ into k_1 and k_2 found in Fig. 7.7 (a)-(c). (b) The time evolution of $|\psi(z)|^2$ from $t=10$ to 15 ms. (c) $|\psi(z)|^2$ at $t=0$ ms and 12 ms.

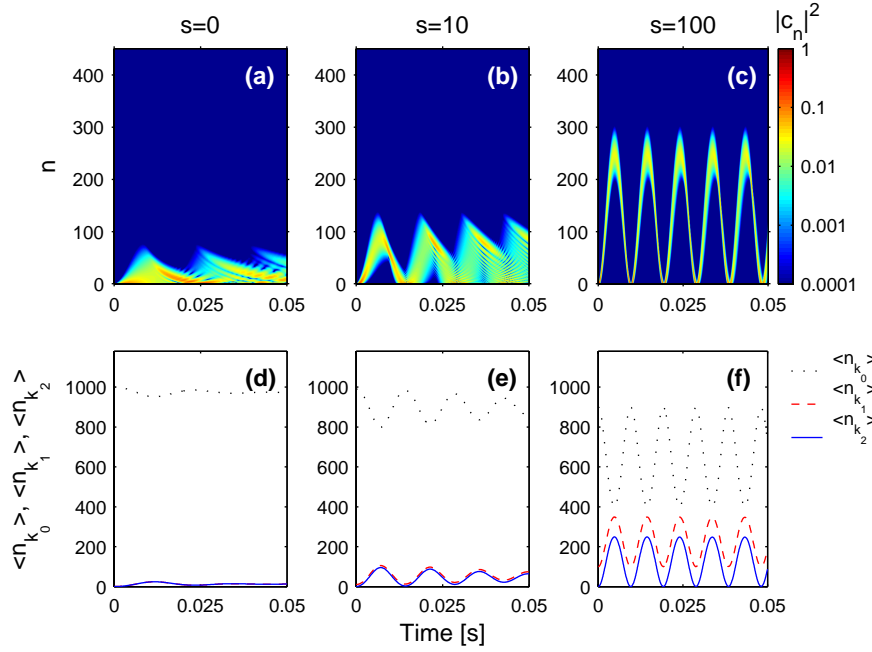


Figure 7.10: Evolution with time of the c_n coefficients is shown, starting with (a) $s=0$, (b) $s=10$ and (c) $s=100$ atoms in the k_1 state. Figure (d)-(f) illustrate the mean number of atoms in the k_0 state (dotted line), k_1 state (dashed line), and the k_2 state (full line). The mean number of atoms in figure (d) is based on the calculation for $s=0$ as shown in (a). Equivalently the mean number of atoms is shown in (e) for $s=10$ and in (f) for $s=100$. The mean number of atoms oscillates between the k_0 state and the k_1, k_2 states. The figure also reveals that it is necessary to seed the initial condensate with a fraction of atoms in the k_1 state ($s>0$) to efficiently start the conversion process and for the system to perform several oscillations. In all the calculations illustrated in this figure the total number of atoms is $N = 1000$ and the volume occupied by the atoms is $V = 8.44 \times 10^{-17} m^3$ corresponding to the same density of atoms as in the Gross-Pitaevskii simulations, where the density is given by $\rho = N/V = N/(A_{\perp}L)$ and L is the length of the extended grid with 512 periods.

CHAPTER 8

Conclusion and perspectives

In this short chapter, the main points of the thesis will be summarized and perspectives for extension of the work will be presented.

8.1 Conclusion and perspectives

In this thesis studies of wave propagation in PCFs and BECs have been carried out. In both systems phase-matched processes determined by the dispersion were shown to play important roles.

Photonic crystal fibers A model based on a nonlinear Schrödinger equation was used to investigate the dynamics of the wave propagation in PCFs.

The simulations of femtosecond pulses in a PCF with a single zero dispersion wavelength revealed that soliton decay plays an important role in the supercontinuum generation. As the pump pulse evolves towards one or more stable solitons dispersive waves are emitted, centered at distinct wavelengths, determined by phase-matching.

The dispersion of the PCFs has a profound influence on the supercontinuum. For a fiber with two closely lying zero dispersion wavelength the supercontinuum is generated through self-phase modulation and phase-matched FWM and not through the soliton decay process mentioned above. Self-phase modulation broadens the spectrum and hereby provides seed wavelengths for degenerate and non-degenerate four-wave mixing. A stable and intense supercontinuum is generated over a wide range of input pulse parameters. The supercontinuum exhibits a depleted region between the two zero dispersion wavelengths due to the FWM processes.

For both types of fiber, the simulations were compared with experimental data for supercontinuum generation and showed good agreement.

The model used in Chap. 4-5 to simulate the supercontinuum generation in PCFs can be used to predict the outcome of wave propagation in PCFs with any dispersion profile, fictive or real. Although the model is very powerful, there is still room for improvement. A full treatment of the second derivative with respect to z in the model would give a proper treatment of the backscattered light. Avoiding to make the slowly varying envelope approximation would be an advantage especially when the pump pulses are short and the resulting spectra are very broad. The issue of causality and the fulfillment of the Kramers-Kronig relations could be thoroughly addressed for the dispersion. Of course a full 3D solution of the problem would be the most accurate, but it would be computationally heavy.

The supercontinua examined in this thesis have already found applications particularly in nonlinear microscopy and frequency metrology. Indeed, the frequency metrology has been revolutionized by this new technology and the optical frequency standard of today is based on a frequency comb generated in a PCF [72]. A supercontinuum source has been produced by Koheras [69], based on FWM of nano-second pulses and further investigations of possibilities for FWM in the PCFs could be useful.

The supercontinua are products of the ultra high nonlinearities combined with the tailorable dispersion in the fibers. Still, the PCFs have other unique

properties to offer, like high birefringence, carriage of high power, multiple cores and claddings, and being endlessly singlemode. Furthermore, the fibers can act as good hosts for rare earth atoms and ions. Consequently, the prospects for applications of the fibers go far beyond the generation of supercontinua and its applications.

It could be interesting to investigate the perspectives of a resonant two or three level system inside a PBG fiber. Physically an atomic gas is placed in the air core of a photonic band gap fiber and strong nonlinear behaviour is expected as a result of the high intensity of the light. Alternatively, the two or three level system could be present as dopant rare earth atoms in the silica core of an index guiding PCF, but in this case the atomic lines will be seriously broadened. The effects of third harmonic generation, lasing without inversion, electromagnetically induced transparency and quantum computing could be addressed. To model the system the electric field of the light propagating in the fiber and the polarization of the atomic gas need to be solved in a self consistent manner.

The system is very rich both from a quantum optical and atom optical point of view, since the PBG fibers can act as a combined waveguides for light and atoms. Due to the dipole forces of light guided in a hollow core fiber, not only atoms but also molecules and particles can be trapped. The PBG fibers are very promising for sensing purposes, not only can reactant molecules be kept and transported in the fibers. Additionally, the PBGs can be made to exactly fit the frequencies of light emitted in certain processes by specific organisms. In medicine they could be used to transport a drug to a specific difficultly accessible place in the body, and if the drug was photo-sensitive, the fiber could be used to guide the light initiating the drug as well. Already evanescent wave sensing has been demonstrated with a PCF in aqueous solution [31].

In the perspective of producing all optical networks the fibers could be used to create central components such as switches and frequency converters based on phase-matched processes.

The PCFs are excellent for building new lasers. In fact lasing has already been demonstrated in rare earth doped double clad fibers, where the outer core is pumped and the lasing is taking place in the inner core [19–23].

The micro structured fibers truly have opened a wide range of opportunities since the structure can be tailor-made for specific purposes. Additionally, the field has benefited from the symbiosis between theoretical suggestions and the actual production of new fibers.

Photonic crystals with other geometries than the fibers could be engineered to fulfill certain phase-matching conditions. For instance 2D planar wave guides and full 3D crystals could be designed to provide phase-matching for four wave mixing.

Bose-Einstein condensates in optical lattices Phase-matched FWM in the system of a BEC in an optical lattice was investigated in the thesis. The dispersion properties imposed by the external periodic potential provides energy and quasi-momentum conservation. Hence, an efficient FWM process can take place,

where pairs of atoms are created. When seeded, up to 95% of the atoms originally in the condensate with wave vector k_0 can be transferred into the correlated pair of states with k_1 and k_2 , as revealed by numerical solution of the Gross-Pitaevskii equation. The system performs Rabi-oscillations between the k_0 and the k_1, k_2 states, due to the coupling to a very narrow continuum of states. The oscillatory behavior is confirmed by a number state analysis with few modes.

A natural extension of the work presented would be a stability analysis to thoroughly investigate the role of transverse excitations and the energetic and dynamic instabilities found at the edge of the Brillouin zone. Of course an experimental demonstration of the proposed phase-matched FWM process could be very interesting as well.

The introduction of superlattices could provide new possibilities for phase-matching conditions. Possibilities for phase-matched processes in particular the FWM could be investigated for condensates in 2D and 3D lattice potentials.

Condensates on chips possess many advantages with respect to creating a small and mobile setup. The chip trap potentials can be tuned to phase-match various processes for instance the FWM process reported in the previous chapter. In this way efficient beam-splitters for atom interferometers able to measure gravitational variations could be created.

The neutral atoms in the optical lattice sites as well as the atoms on chips could act as qubits and the systems could potentially be excellent for quantum computation purposes. For instance the Mott insulator phase has been suggested [110] for a quantum register.

Perhaps the most important property of BECs in optical lattices is the great flexibility the system offers as a model system for condensed matter physics and fundamental quantum statistics. Due to the tunability of the strength of the periodic potentials and the dimensionality, phase-transitions such as the Mott-insulator and Tonks gas have been investigated. The introduction of fermions and boson-fermion mixtures, not to speak of molecules, certainly opens the doors for investigations of complex quantum statistical systems.

Many ideas can be directly transferred between the two fields. The engineering of the dispersion relation for a BEC due to the optical lattice is equivalent to the dispersive engineering for a PCF due to the micro-structuring. New and interesting ideas can arise by merging the two fields. For instance it could be possible to move entire BECs inside PBG fibers. For both fields the engineering of the periodic structures can be carried out in 1, 2, and 3 dimensions and there are certainly many possibilities yet to be discovered and investigated in both of the fields.

8.2 Acknowledgments

First of all I would like to thank my supervisors Søren Keiding and Klaus Mølmer for their encouragement and support. They have both stood up for me beyond their call of duty. Klaus has always time and it has been a great experience to work with him, not least because of his enthusiasm and creativity. He is always ready with new ideas, crucial insights and a spreading optimism. Søren has acted as a protector and has miraculously solved bureaucratic deadlocks and he has always shown interest in my project, my life and my well-being.

My studies at the University have been a pleasure due to the good company of students and staff at the Departments of Physics and Chemistry. Both Klaus and Søren have a great sense of humor, which I highly value. Lars Bojer and Klaus have a symbiotic ability to give the lunch conversation yet another twist. My fellow students have contributed to an enjoyable atmosphere and entertaining coffee breaks: Thomas Kjeldsen, Mikkel Bo Nielsen, Thorbjørn Møller Pedersen, Kristian Rechendorff, Anders Rønnau, Ivan Storgaard Vogelius and Janus Halleløv Wesenberg. The company of the Femto Chemistry group has also been a great pleasure and I have enjoyed working and discussing with the group: Thomas Vestergaard Andersen, Carsten Krogh Nielsen, Henrik Nørgaard Paulsen, Jakob Juul Larsen, Henrik Stapelfeldt and Jan Thøgersen.

Thanks to Uffe Vestergaard Poulsen and Thomas Vestergaard Andersen for proof-reading the thesis and thanks to Grete Flarup for her flexible help in general. I appreciate the helpfulness of the people at Crystal Fibre. The NKT Academy is acknowledged for partial financing of my Ph.D. studies. I would as well like to thank QUANTOP for financial support and the Danish Center for Scientific Computing for computation time.

Finally, I would like to thank my friends outside the university and my family. In particular, I thank my parents and brother for their never failing support.

Karen Marie Hilligsøe

Bibliography

- [1] M. Anderson, J. Ensher, M. Matthews, C. Wieman, and E. Cornell, *Science* **269**, 198 (1995).
- [2] K. Davis, M.-O. Mewes, M. Andrews, N. van Druten, D. Durfee, D. Kurn, and W. Ketterle, *Phys. Rev. Lett.* **75**, 3969 (1995).
- [3] J. C. Knight and P. S. J. Russell, *Optics and Photonics News* **13**, **March**, 26 (2002).
- [4] P. S. J. Russell, *Science* **299**, 358 (2003).
- [5] A. Bjarklev, J. Broeng, and A. S. Bjarklev, *Photonic crystal fibres* (Kluwer Academic Publishers, Boston, 2003).
- [6] J. D. Joannopoulos, R. D. Meade, and J. N. Winn, *Photonic crystals - molding the flow of light* (Princeton University Press, 1995), 1st ed.
- [7] J. D. Joannopoulos, P. R. Villeneuve, and S. Fan, *Nature* **386**, 143 (1997).
- [8] K. Sakoda, *Optical properties of photonic crystals* (Springer, Berlin, 2001), 1st ed.
- [9] E. Yablonovitch, *Phys. Rev. Lett.* **58**, 2059 (1987).
- [10] S. John, *Phys. Rev. Lett.* **58**, 2486 (1987).
- [11] E. Yablonovitch, T. J. Gmitter, and K. M. Leung, *Phys. Rev. Lett.* **67**, 2295 (1991).
- [12] C. T. Chan, K. M. Ho, and C. M. Soukoulis, *Europhys. Lett.* **16**, 563 (1991).
- [13] J. C. Knight, T. A. Birks, P. S. J. Russell, and J. P. de Sandro, *J. Opt. Soc. Am. A.* **15**, 748 (1998).
- [14] R. F. Cregan, B. J. Mangan, J. C. Knight, T. A. Birks, P. S. J. Russell, P. J. Roberts, and D. C. Allan, *Science* **285**, 1537 (1999).
- [15] J. C. Knight, T. A. Birks, P. S. J. Russell, and D. M. Atkin, *Opt. Lett.* **21**, 1547 (1996).

- [16] T. A. Birks, J. C. Knight, and P. S. J. Russell, *Opt. Lett.* **22**, 961 (1997).
- [17] M. A. van Eijkelenborg, M. C. J. Large, A. Argyros, J. Zagari, S. Manos, N. A. Issa, I. Bassett, S. Fleming, R. C. McPhedran, C. Martijn de Sterke, et al., *Opt. Express* **9**, 319 (2001), URL <http://www.opticsexpress.org/abstract.cfm?URI=OPEX-9-7-319>.
- [18] V. V. R. K. Kumar, A. K. George, W. H. Reeves, J. C. Knight, and P. S. Russell, *Opt. Express* **10**, 1520 (2002).
- [19] K. Furusawa, A. Malinowski, J. H. V. Price, T. M. Monro, J. K. Sahu, J. Nilsson, and D. J. Richardson, *Opt. Express* **9**, 714 (2001), URL <http://www.opticsexpress.org/abstract.cfm?URI=OPEX-9-13-714>.
- [20] W. J. Wadsworth, R. M. Percival, G. Bouwmans, J. C. Knight, and P. S. J. Russell, *Opt. Express* **11**, 48 (2003), URL <http://www.opticsexpress.org/abstract.cfm?URI=OPEX-11-1-48>.
- [21] J. Limpert, T. Schreiber, S. Nolte, H. Zellmer, A. Tünnermann, R. Iliew, F. Lederer, J. Broeng, G. Vienne, A. Petersson, et al., *Opt. Express* **11**, 818 (2003), URL <http://www.opticsexpress.org/abstract.cfm?URI=OPEX-11-7-818>.
- [22] F. C. McNeillie, E. Riis, J. Broeng, J. R. Folkenberg, A. Petersson, H. Simonson, and C. Jacobsen, *Opt. Express* **12**, 3981 (2004), URL <http://www.opticsexpress.org/abstract.cfm?URI=OPEX-12-17-3981>.
- [23] J. Limpert, N. Deguil-Robin, I. Manek-Hönninger, F. Salin, F. Röser, A. Liem, T. Schreiber, S. Nolte, H. Zellmer, A. Tünnermann, et al., *Opt. Express* **13**, 1055 (2005), URL <http://www.opticsexpress.org/abstract.cfm?URI=OPEX-13-4-1055>.
- [24] A. Ortigosa-Blanch, J. C. Knight, W. J. Wadsworth, J. Arriaga, B. J. Mangan, T. A. Birks, and P. S. J. Russell, *Opt. Lett.* **25**, 1325 (2000).
- [25] E. Yablonovitch, *Phys. World* **12**, 20 (1999).
- [26] P. Petropoulos, T. M. Monro, W. Belardi, K. Furusawa, J. H. Lee, and D. J. Richardson, *Opt. Lett.* **26**, 1233 (2001).
- [27] J. E. Sharping, M. Fiorentino, A. Coker, P. Kumar, and R. S. Windeler, *Opt. Lett.* **26**, 1048 (2001).
- [28] A. V. Yulin, D. V. Skryabin, and P. S. J. Russell, *Opt. Lett.* **29**, 2411 (2004).
- [29] F. Benabid, J. C. Knight, G. Antonopoulos, and P. S. J. Russell, *Science* **298**, 399 (2002).
- [30] Y. L. Hoo, W. Jin, C. Shi, H. L. Ho, D. N. Wang, and S. C. Ruan, *Applied Optics* **42** (2003).

- [31] J. B. Jensen, L. H. Pedersen, P. E. Hoiby, L. B. Nielsen, T. P. Hansen, J. R. Folkenberg, J. Riishede, D. Noordegraaf, K. Nielsen, A. Carlsen, et al., *Opt. Lett.* **29**, 1974 (2004).
- [32] S. Lorenz, C. Silberhorn, N. Korolkova, R. S. Windeler, and G. Leuchs, **73**, 855 (2001).
- [33] S. A. Diddams, D. J. Jones, J. Ye, S. T. Cundiff, J. L. Hall, J. K. Ranka, R. S. Windeler, R. Holzwarth, T. Udem, and T. W. Hänsch, *Phys. Rev. Lett.* **84**, 5102 (2000).
- [34] R. Holzwarth, T. Udem, T. W. Hänsch, J. C. Knight, W. J. Wadsworth, and P. S. J. Russell, *Phys. Rev. Lett.* **85**, 2264 (2000).
- [35] I. Hartl, X. D. Li, C. Chudoba, R. K. Ghanta, T. H. Ko, J. G. Fujimoto, J. K. Ranka, and R. S. Windeler, *Opt. Lett.* **26**, 608 (2001).
- [36] K. L. Corwin, N. R. Newbury, J. M. Dudley, S. Coen, S. A. Diddams, B. R. Washburn, K. Weber, and R. S. Windeler, *Appl. Phys. B* **77**, 269 (2003).
- [37] J. K. Ranka, R. S. Windeler, and A. J. Stentz, *Opt. Lett.* **25**, 25 (2000).
- [38] S. G. Johnson and J. D. Joannopoulos, *Opt. Express* **8**, 173 (2001), URL <http://www.opticsexpress.org/abstract.cfm?URI=OPEX-8-3-173>.
- [39] S. G. Johnson and J. D. Joannopoulos (<http://ab-initio.mit.edu/mpb/>).
- [40] N. A. Mortensen, *Opt. Express* **10**, 341 (2002), URL <http://www.opticsexpress.org/abstract.cfm?URI=OPEX-10-7-341>.
- [41] G. P. Agrawal, *Nonlinear Fiber Optics* (Academic Press, 2001), 3rd ed.
- [42] S. Coen, A. H. C. Chau, R. Leonhardt, J. D. Harvey, J. C. Knight, W. J. Wadsworth, and P. S. J. Russell, *Opt. Lett.* **26**, 1356 (2001).
- [43] S. Coen, A. H. C. Chau, R. Leonhardt, J. D. Harvey, J. C. Knight, W. J. Wadsworth, and P. S. J. Russell, *J. Opt. Soc. Am. B*, **19**, 753 (2002).
- [44] J. M. Dudley, L. Provino, N. Grossard, H. Maillotte, R. S. Windeler, B. J. Eggleton, and S. Coen, *J. Opt. Soc. Am. B*, **19**, 765 (2002).
- [45] A. L. Gaeta, *Opt. Lett.* **27**, 924 (2002).
- [46] G. Genty, M. Lehtonen, H. Ludvigsen, J. Broeng, and M. Kaivola, *Opt. Express* **10**, 1083 (2002), URL <http://www.opticsexpress.org/abstract.cfm?URI=OPEX-10-20-1083>.
- [47] B. R. Washburn, S. E. Ralph, and R. S. Windeler, *Opt. Express* **10**, 575 (2002), URL <http://www.opticsexpress.org/abstract.cfm?URI=OPEX-10-13-575>.

- [48] J. Herrmann, U. Griebner, N. Zhavoronkov, A. Husakou, D. Nickel, J. C. Knight, W. J. Wadsworth, and P. S. J. Russell, *Phys. Rev. Lett.* **88**, 173901 (2002).
- [49] A. V. Husakou and J. Herrmann, *Phys. Rev. Lett.* **87**, 203901 (2001).
- [50] K. J. Blow and D. Wood, *IEEE J. Quantum Electron.* **25**, 2665 (1989).
- [51] P. V. Mamyshev and S. V. Chernikov, *Opt. Lett.* **19**, 1076 (1990).
- [52] J. Moloney and A. Newell, *Nonlinear optics* (Westview Press, Boulder, 2004).
- [53] L. F. Mollenauer, R. H. Stolen, and M. N. Islam, *Phys. Rev. Lett.* **45**, 1095 (1980).
- [54] R. M. Joseph, S. C. Hagness, and A. Taflove, *Opt. Lett.* **16**, 1412 (1991).
- [55] P. M. Goorjian and A. Taflove, *Opt. Lett.* **17**, 180 (1992).
- [56] R. W. Boyd, *Nonlinear Optics* (Academic Press, 1992).
- [57] S. Diddams and J.-C. Diels, *J. Opt. Soc. Am. B.* **13**, 1120 (1996).
- [58] M. Frigo and S. G. Johnson (<http://www.fft.w.org>).
- [59] *J. Opt. Soc. Am. B.* **19**, 2046 (2002).
- [60] A. K. Abeeluck and C. Headley, *Opt. Lett.* **30**, 61 (2005).
- [61] A. V. Husakou and J. Herrmann, *J. Opt. Soc. Am. B.* **19**, 2171 (2002).
- [62] A. V. Husakou and J. Herrmann, *Appl. Phys. B* **77**, 227 (2003).
- [63] J. M. Dudley and S. Coen, *IEEE J. Quantum Electron.* **8**, 651 (2002).
- [64] A. B. Fedotov, A. N. Naumov, A. M. Zheltikov, I. Bugar, J. D. Chorvat, A. P. Tarasevitch, and D. von der Linde, *J. Opt. Soc. Am. B.* **19**, 2156 (2002).
- [65] A. Ortigosa-Blanch, J. C. Knight, and P. S. J. Russell, *J. Opt. Soc. Am. B.* **19**, 2567 (2002).
- [66] W. H. Reeves, D. V. Skryabin, F. Biancalana, J. C. Knight, P. S. J. Russell, F. G. Omenetto, A. Efimov, and A. J. Taylor, *Nature* **424**, 511 (2003).
- [67] N. I. Nikolov, O. Bang, and A. Bjarklev, *J. Opt. Soc. Am. B.* **20**, 2329 (2003).
- [68] W. J. Wadsworth, N. Joly, J. C. Knight, T. A. Birks, F. Biancalana, and P. S. J. Russell, *Opt. Express* **12**, 299 (2004), URL <http://www.opticsexpress.org/abstract.cfm?URI=OPEX-12-2-299>.
- [69] (<http://www.koheras.com>).

- [70] J. M. Dudley and S. Coen, *Opt. Lett.* **27**, 1180 (2002).
- [71] S. T. Cundiff and J. Ye, *Rev. Mod. Phys.* **75**, 325 (2003).
- [72] (<http://www.menlosystems.de>).
- [73] P. K. A. Wai, Y. C. Lee, and H. H. Chen, *Opt. Lett.* **11**, 464 (1986).
- [74] D. V. Skryabin, F. Luan, J. C. Knight, and P. S. J. Russell, *Science* **301**, 1705 (2003).
- [75] F. G. Omenetto, A. J. Taylor, M. D. Moores, J. Arriaga, J. C. Knight, W. J. Wadsworth, and P. S. J. Russell, *Opt. Lett.* **26**, 1158 (2001).
- [76] F. G. Omenetto, A. Efimov, A. J. Taylor, J. C. Knight, W. J. Wadsworth, and P. S. J. Russell, *Opt. Express* **11**, 61 (2003), URL <http://www.opticsexpress.org/abstract.cfm?URI=OPEX-11-1-61>.
- [77] B. Segev, *Phys. Rev. A* **63**, 052114 (2001).
- [78] J. M. Dudley, X. Gu, L. Xu, M. Kimmel, E. Zeek, P. O'Shea, R. Trebrino, S. Coen, and R. S. Windeler, *Opt. Express* **10**, 1215 (2002).
- [79] A. Hasegawa, *Optical solitons in fibers* (Springer-Verlag Berlin, 1990), 2nd ed.
- [80] X. Gu, M. Kimmel, A. P. Shreenath, R. Trebino, J. M. Dudley, S. Coen, and R. S. Windeler, *Opt. Express* **11**, 2697 (2003), URL <http://www.opticsexpress.org/abstract.cfm?URI=OPEX-11-21-2697>.
- [81] V. P. Yanovsky and F. W. Wise, *Opt. Lett.* **19**, 1547 (1994).
- [82] B. Hall, D. Anderson, M. Lisak, G. Boyer, M. Karlsson, and A. Berntson, *J. Opt. Soc. Am. B.* **18**, 1652 (2001).
- [83] F. Druon and P. Georges, *Opt. Express* **12**, 3383 (2004), URL <http://www.opticsexpress.org/abstract.cfm?URI=OPEX-12-15-3383>.
- [84] F. Biancalana, D. V. Skryabin, and P. S. J. Russell, *Phys. Rev. E* **68**, 046603 (2003).
- [85] J. Squier and M. Müller, *Rev. Sci. Instrum.* **72**, 2855 (2001).
- [86] C. J. Pethick and H. Smith, *Bose-Einstein condensation in dilute gases* (Cambridge University Press, 2002).
- [87] L. Pitaevskii and S. Stringari, *Bose-Einstein condensation* (Oxford, Clarendon Press, 2003).
- [88] F. Dalfovo, S. Giorgini, L. P. Pitaevskii, and S. Stringari, *Reviews of Modern Physics* **71**, 463 (1999).

- [89] A. J. Leggett, *Rev. Mod. Phys.* **73**, 307 (2001).
- [90] Y. Castin, in 'Coherent atomic matter waves', Lecture Notes of Les Houches Summer School, edited by R. Kaiser, C. Westbrook, and F. David, EDP Sciences and Springer-Verlag, arXiv:cond-mat/0105058 pp. 1–136 (2001).
- [91] O. Morsch and M. Oberthaler, submitted to *Rev. Mod. Phys.* (2004).
- [92] I. Bloch, *Physics World* **April**, 25 (2004).
- [93] C. C. Bradley, C. A. Sackett, J. J. Tollett, and R. G. Hulet, *Phys. Rev. Lett.* **75**, 1687 (1995).
- [94] E. A. Cornell and C. E. Wieman, *Rev. Mod. Phys.* **74**, 875 (2002).
- [95] W. Ketterle, *Rev. Mod. Phys.* **74**, 1131 (2002).
- [96] W. Ketterle, D. S. Durfee, and D. M. Stamper-Kurn, *Making, probing and understanding Bose-Einstein condensates* (in "Bose-Einstein condensation in atomic gases, Proceedings of the International School of Physics "Enrico Fermi"", Course CXL, edited by M. Inguscio, S. Stringari, and C. Wieman (IOS Press, Amsterdam), pp. 67-176, arXiv:cond-mat/9904034, 1999).
- [97] M. Greiner, O. Mandel, T. Esslinger, T. W. Hänsch, and I. Bloch, *Nature* **415**, 39 (2002).
- [98] M. Budde and K. Mølmer, *Phys. Rev. A* **70**, 053618 (2004).
- [99] G. Lenz, P. Meystre, and E. Wrigth, *Phys. Rev. A* **50**, 1681 (1994).
- [100] C. Martijn de Sterke and J. Sipe, *Phys. Rev. A* **38**, 5149 (1988).
- [101] C. Martijn de Sterke and J. Sipe, *Phys. Rev. A* **39**, 5163 (1989).
- [102] A. V. Yulin, D. V. Skryabin, and P. S. J. Russell, *Phys. Rev. Lett.* **91**, 260402 (2003).
- [103] Y. Castin and K. Mølmer, *Phys. Rev. A* **51** (1995).
- [104] H. Friedrich, *Theoretical atomic physics* (Springer-Verlag, Berlin, 1990).
- [105] S. L. Cornish, N. R. Claussen, J. L. Roberts, E. A. Cornell, and C. E. Wieman, *Phys. Rev. Lett.* **85**, 1795 (2000).
- [106] N. Bogoliubov, *J.Phys. (Moscow)* **11**, 23 (1947).
- [107] Y. Castin, cond-mat/0105058 pp. 1–146 (2001).
- [108] L. Salasnich, A. Parola, and L. Reatto, *Phys. Rev. A* **65**, 043614 (2002).
- [109] K. Berg-Sørensen and K. Mølmer, *Phys. Rev. A* **58**, 1480 (1998).

- [110] D. Jaksch, C. Bruder, J. I. Cirac, C. W. Gardiner, and P. Zoller, *Phys. Rev. Lett.* **81**, 3108 (1998).
- [111] T. Stöferle, H. Moritz, C. Schori, M. Köhl, and T. Esslinger, *Phys. Rev. Lett.* **92**, 130403 (2004).
- [112] N. W. Ashcroft and N. D. Mermin, *Solid state physics* (Saunders College Publishing, 1976).
- [113] B. Wu and Q. Niu, *Phys. Rev. A* **64**, 061603 (2001).
- [114] B. Wu and Q. Niu, *New J. Phys.* **5**, 104 (2003).
- [115] M. Machholm, C. J. Pethick, and H. Smith, *Phys. Rev. A* **67**, 053613 (2003).
- [116] B. Wu and Q. Niu, *Phys. Rev. A* **61**, 023402 (2000).
- [117] M. Machholm, A. Nicolin, C. J. Pethick, and H. Smith, *Phys. Rev. A* **69**, 043604 (2004).
- [118] L. Fallani, L. D. Sarlo, J. E. Lye, M. Modugno, R. Saers, C. Fort, and M. Inguscio, *Phys. Rev. Lett.* **93**, 140406 (2004).
- [119] L. D. Sarlo, L. Fallani, J. E. Lye, M. Modugno, R. Saers, C. Fort, and M. Inguscio, *cond-mat/0412279* pp. 1–10 (2004).
- [120] L. Fallani, F. S. Cataliotti, J. Catani, C. Fort, M. Modugno, M. Zawada, and M. Inguscio, *Phys. Rev. Lett.* **91**, 240405 (2003).
- [121] M. Modugno, C. Tozzo, and F. Dalfovo, *Phys. Rev. A* **70**, 043625 (2004).
- [122] B. Eiermann, T. Anker, M. Albiez, M. Taglieber, P. Treutlein, K.-P. Marzlin, and M. K. Oberthaler, *Phys. Rev. Lett.* **92**, 230401 (2004).
- [123] L. Khaykovich, F. Schreck, G. Ferrari, T. Bourdel, J. Cubizolles, L. D. Carr, Y. Castin, and C. Salomon, *Science* **296**, 1290 (2002).
- [124] K. E. Strecker, G. B. Partridge, A. G. Truscott, and R. G. Hulet, *Nature* **417**, 150 (2002).
- [125] T. Anker, M. Albiez, B. Eiermann, M. Taglieber, and M. K. Oberthaler, *Opt. Express* **12**, 11 (2004), URL <http://www.opticsexpress.org/abstract.cfm?URI=OPEX-12-1-11>.
- [126] A. Trombettoni and A. Smerzi, *Phys. Rev. Lett.* **86**, 2353 (2001).
- [127] O. Morsch, J. Müller, M. Cristiani, and E. Arimondo, *cond-mat/0103466* pp. 1–5 (2001).
- [128] J. Liu, L. Fu, B.-Y. Ou, S.-G. Chen, D.-I. Choi, B. Wu, and Q. Niu, *Phys. Rev. A* **66**, 023404 (2002).

- [129] B. P. Anderson and M. A. Kasevich, *Science* **282**, 1686 (1998).
- [130] M. Chiofalo, M. Polini, and M. Tosi, *Eur. Phys. J. D* **11**, 371 (2000).
- [131] W. Zwerger, *J. Opt. B: Quantum Semiclass. Opt.* **5**, S9 (2003).
- [132] S. Peil, J. V. Porto, B. L. Tolra, J. M. Obrecht, B. E. King, M. Subbotin, S. L. Rolston, and W. D. Phillips, *Phys. Rev. A* **67**, 051603 (2003).
- [133] J. Y. L. Pearl, E. A. Ostrovskaya, and Y. S. Kivshar, *cond-mat/0408291* (2004).
- [134] P. Hommelhoff, W. Hänsel, T. Steinmetz, T. W. Hänsch, and J. Reichel, submitted to *New Journal of Physics*, *arXiv:quant-ph/0411012* (2004).
- [135] W. Zhang, C. P. Search, H. Pu, P. Meystre, and E. M. Wright, *Phys. Rev. Lett.* **90**, 140401 (2003).
- [136] I. Bouchoule and K. Mølmer, *Phys. Rev. A* **67**, 011603 (2003).
- [137] P. G. Savvidis, J. J. Baumberg, R. M. Stevenson, M. S. Skolnick, D. M. Whittaker, and J. S. Roberts, *Phys. Rev. Lett* **84**, 1547 (2000).
- [138] C. Ciuti, P. Schwendimann, B. Deveaud, and A. Quattropani, *Phys. Rev. B* **62**, R4825 (2000).
- [139] P. G. Savvidis, C. Ciuti, J. J. Baumberg, D. M. Whittaker, M. S. Skolnick, and J. S. Roberts, *Phys. Rev. B* **64**, 075311 (2001).
- [140] J. M. Vogels, K. Xu, and W. Ketterle, *Phys. Rev. Lett.* **89**, 020401 (2002).
- [141] L. Deng, E. W. Hagley, J. Wen, M. Trippenbach, Y. Band, P. S. Julienne, J. E. Simsarian, K. Helmerson, S. L. Rolston, and W. D. Phillips, *Nature* **398**, 218 (1999).
- [142] M. Trippenbach, Y. B. Band, and P. S. Julienne, *Opt. Express* **3**, 530 (1998), URL <http://www.opticsexpress.org/abstract.cfm?URI=OPEX-3-13-530>.
- [143] M. Trippenbach, Y. B. Band, and P. S. Julienne, *Phys. Rev. A* **62**, 023608 (2000).
- [144] L. You, W. Hoston, and M. Lewenstein, *Phys. Rev. A* **55**, R1581 (1997).
- [145] C. Cohen-Tannoudji, J. Dupont-Roc, and G. Grynberg, *Atom-photon interactions. Basic processes and applications* (John Wiley and Sons, Inc., New York, 1992).
- [146] S. Burger, F. S. Cataliotti, C. Fort, F. Minardi, M. Inguscio, M. L. Chiofalo, and M. P. Tosi, *Phys. Rev. Lett.* **86**, 4447 (2001).